DEVELOPMENT OF NOVEL 2 DOF THERMAL MICRO ACTUATORS AND A COMPARISON OF DIFFERENT DISPLACEMENT MEASUREMENT TECHNIQUES

by

Rene d'Entremont

Submitted in partial fulfilment of the requirements
for the degree of Master of Applied Science

Dalhousie University
Halifax, Nova Scotia
July 2011

© Copyright by Rene d'Entremont, 2011

DALHOUSIE UNIVERSITY

DEPARTMENT OF MECHANICAL ENGINEERING

The undersigned hereby certify that they have read and recommend to the Faculty of Graduate Studies for acceptance a thesis entitled "DEVELOPMENT OF NOVEL 2 DOF THERMAL MICRO ACTUATORS AND A COMPARISON OF DIFFERENT DISPLACEMENT MEASUREMENT TECHNIQUES" by Rene d'Entremont in partial fulfilment of the requirements for the degree of Master of Applied Science.

Dated: July 20, 2011

Supervisor: ________________________________

Readers: ________________________________

____

DALHOUSIE UNIVERSITY

DATE: July 20, 2011

AUTHOR: Rene d'Entremont

TITLE: DEVELOPMENT OF NOVEL 2 DOF THERMAL MICRO ACTUATORS AND A COMPARISON OF DIFFERENT DISPLACEMENT MEASUREMENT TECHNIQUES

DEPARTMENT OR SCHOOL: Department of Mechanical Engineering

DEGREE: MASc CONVOCATION: October YEAR: 2011

Permission is herewith granted to Dalhousie University to circulate and to have copied for non-commercial purposes, at its discretion, the above title upon the request of individuals or institutions. I understand that my thesis will be electronically available to the public.

The author reserves other publication rights, and neither the thesis nor extensive extracts from it may be printed or otherwise reproduced without the author's written permission.

The author attests that permission has been obtained for the use of any copyrighted material appearing in the thesis (other than the brief excerpts requiring only proper acknowledgement in scholarly writing), and that all such use is clearly acknowledged.

____

Signature of Author

Table of Contents

List of Tables viii

List of Figures ix

Abstract xii

List of Abbreviations and Symbols Used xiii

Acknowledgements xvi

Chapter 1: Introduction 1

1.1: Objective 1

1.1.1: Project Scope 1

1.1.2: Author Contribution 2

1.2: What are MEMS? 2

1.2.1: PolyMUMPs Process Overview 4

1.3: MEMS Actuators 8

1.3.1: Parallel Plate 9

1.3.2: Linear Comb Drive 10

1.3.3: Standard Thermal Actuator 11

1.3.4: Chevron Actuator 14

1.3.5: Existing Vertical Thermal Actuator (VTA) Work 15

1.3.6: Vertical Thermal Actuators Theory 21

1.4: Existing Work on Image Displacement and Focus 25

Chapter 2: 2 DOF Thermal Actuator (2DTA) 28

2.1: Description 28

2.2: Actuator Powering Configurations 30

2.3: Out-of Plane (Z) Displacement 31

2.4: Simple Planar (X) Displacement 32

2.5: Combination X and Z Displacement 33

2.6: Fabricated Device 34

Chapter 3: Finite Element Analysis 36

3.1: Model 36

3.1.1: Importing the 2DTA Model 36

3.1.2: Domains Modeled 36

3.1.3: Stress-Strain Subdomain 37

3.1.4: Thermal Domain Subdomain 37

3.1.5: Joule Heating Subdomain 38

3.1.6: Model Physical Properties 39

3.1.7: Convergence Study 41

3.2: Displacement Results in Common Stepping Positions 42

3.2.1: Maximum Z Lift Position 43

3.2.2: Maximum X-Displacement 47

3.2.3: Combination X and Z Displacement 51

3.3: Maximum Displacement Range 55

3.3.1: Out-of-Plane Displacement versus Current 55

3.3.2: Theoretical Displacement Envelope 56

3.4: Effects of Changing Heat Transfer Coefficient as Out-of-Plane Displacement Increases 58

3.5: Mechanical Natural Frequency 59

3.6: Transient Heat Transfer Analysis 62

Chapter 4: Hardware Setup 64

4.1: Electrical Setup 65

4.1.1: LabVIEW 66

4.1.2: Stepper Motor Control Hardware ... 68

4.1.3: Camera Setup ... 71

Chapter 5: Profiler Measurements ... 72

5.1: Experimental Setup ... 72

5.1.1: Profiler Theory ... 74

5.2: Area scans ... 75

5.2.1: Off Position ... 77

5.2.2: Maximum Lift Position ... 77

5.3: Profile Scans ... 79

5.3.1: Cross Section Diagram ... 80

5.3.2: Off Position Measurement ... 81

5.3.3: Maximum Lift Position ... 83

5.3.4: X and Z Displacement Combination ... 85

Chapter 6: Collecting X-Displacement Data Using Camera Images ... 87

6.1: Experimental Setup ... 87

6.2: X-Displacement Using an Optical Camera ... 87

6.2.1: NI Vision Assistant ... 88

6.2.2: Matlab ... 89

6.2.3: Optical Profiler X Measurements ... 90

6.2.4: Results ... 92

Chapter 7: Collecting Z-Displacement Data Using Camera Refocusing ... 95

7.1: Theory ... 95

7.2: Experimental Setup ... 96

7.3: Determination of Best Focus for MEMS Devices ... 96

7.3.1: Auto-Correlation Algorithm ... 97

7.3.2: Tenengrad Gradient Algorithm 98
7.3.3: Normalized Variance Algorithm 99
7.3.4: Energy Laplace Algorithm 100
7.4: Results 102
7.4.1: Accuracy 104
7.4.2: Recommendation 108
Chapter 8: Future Work & Recommendations 109
Chapter 9: Conclusion 111
Appendix A: Designed Chips 113
Appendix B: MatLab Code 116
B.2: Batch Height Measurements using the Optical Profiler 118
B.3: Normalized Autocorrelation Function 119
B.4: Normalized Variance Function 120
B.5: Tennengrad Gradient 121
B.6: Maximum Focus Determination and Curve Fitting 122
B.7: Main 123
References 124

List of Tables

TABLE 1: SUMMARY OF EXISTING IN-PLANE THERMAL ACTUATORS 15

TABLE 2: SUMMARY OF EXISTING VTAS 21

TABLE 3: FEA POLYSILICON PROPERTIES 40

TABLE 4: COMSOL CONVERGENCE STUDY RESULTS 41

TABLE 5: FEA MAXIMUM Z LIFT ELECTRICAL SETTINGS AND DISPLACEMENT 44

TABLE 6: FEA MAXIMUM X ELECTRICAL SETTINGS AND DISPLACEMENT 48

TABLE 7: FEA XZ COMBINATION ELECTRICAL SETTINGS AND DISPLACEMENT 52

List of Figures

FIGURE 1: POLYMUMPS LAYERS 5

FIGURE 2: FIRST STEP OF THE POLYMUMPS PROCESS: DEPOSITION OF POLY0 AND PHOTORESIST (MEMSCAP [7]) 6

FIGURE 3: PATTERNING OF THE PHOTORESIST IN PREPARATION TO ETCH POLY0 (MEMSCAP [7]) 6

FIGURE 4: POLY0 ETCHED AND PHOTORESIST REMOVED (MEMSCAP [7]) 7

FIGURE 5: BUILD-UP OF ALL POLYMUMPS LAYERS BEFORE OXIDE REMOVAL (MEMSCAP [7]) 7

FIGURE 6: FINALIZED PROCESS (MEMSCAP [7]) 8

FIGURE 7 : PARALLEL PLATE ACTUATOR 10

FIGURE 8: COMB DRIVE ACTUATOR 280 11

FIGURE 9: STANDARD THERMAL ACTUATOR 12

FIGURE 10: PARALLEL TA 13

FIGURE 11: TA VARIABLES 13

FIGURE 12: STANDARD 200 μM ARM CHEVRON ACTUATOR 14

FIGURE 13: VERTICAL THERMAL ACTUATOR (VTA) 15

FIGURE 14: BAR TYPE TA ADAPTED FROM CHEN [21] 16

FIGURE 15: 3 ARMED VTA 17

FIGURE 16: 4 ARMED BI-DIRECTIONAL VTA FROM CHEN [1] 18

FIGURE 17: CHEVRON VERTICAL THERMAL ACTUATORS 25

FIGURE 18: STANDARD 2 DOF THERMAL ACTUATOR 28

FIGURE 19: 2DTA ARM CROSS-SECTION IN THE MIDDLE OF FIGURE 18 (ENLARGED VIEW) 29

FIGURE 20: 2DTA IN VARIOUS POSITIONS 30

FIGURE 21: 2DTA POWERING POINTS NAMES 31

FIGURE 22: OUT-OF-PLANE 2DTA POWERING 32

FIGURE 23: 2DTA SIMPLE X POWERING 33

FIGURE 24: 2DTA XZ-DISPLACEMENT POWERING 34

FIGURE 25: SEM IMAGE OF CONSTRUCTED 2DTA 35

FIGURE 26: ACTUAL 2DTA DISPLACEMENT. FROM LEFT TO RIGHT, OFF, UNFOCUSED MAXIMUM Z-DISPLACEMENT (5 μM), AND MAXIMUM X-DISPLACMENT (1.75 μM) 35

FIGURE 27: 2DTA COMSOL MODEL WITH HIGHLIGHTED POLY0 PADS 39

FIGURE 28: CONVERGENCE STUDY. DISPLACEMENT RESULTS VERSUS NUMBER OF ELEMENTS 42

FIGURE 29: FOUR STEP LIFT AND SLIDE ACTUATION CYCLE (SIDE VIEW IN THE ZX PLANE) 43

FIGURE 30: FEA MAXIMUM Z-DISPLACEMENT (μM) 44

FIGURE 31: FEA 2DTA DISPLACEMENT PROFILE ALONG A POLY1 ARM 45

FIGURE 32: FEA MAXIMUM Z- DISPLACEMENT END VIEW (XZ PLANE) 46

FIGURE 33: FEA MAXIMUM Z-DISPLACEMENT ARM TEMPERATURE (K) 46

Figure 34: FEA Maximum Z- displacement Arm Current Flow (A/m^2) ... 47
Figure 35: FEA Maximum X-displacement (μm) ... 49
Figure 36: FEA Maximum X-Displacement End View (XZ Plane) ... 50
Figure 37: FEA Maximum X Arm Temperature (K) ... 50
Figure 38: FEA Maximum X Arm Current Density (A/m^2) ... 51
Figure 39: FEA XZ Combination Displacement (μm) ... 53
Figure 40: FEA Maximum XZ Combination Displacement (XZ Plane) ... 53
Figure 41: FEA XZ Combination Arm Temperature (K) ... 54
Figure 42: FEA XZ Combination Arm Current (A/m^2) ... 55
Figure 43: FEA Z-Displacement versus Poly1 Current ... 56
Figure 44: FEA 2DTA Displacement Envelope ... 57
Figure 45: 2DTA Arm Temperature Profile With and Without Height Dependant Heat Conduction to the Substrate ... 59
Figure 46: First Out-of-Plane Mode (44 kHz) ... 60
Figure 47: Planar Mode (131 kHz) ... 61
Figure 48: Second Out-of-Plane Mode (362 kHz) ... 61
Figure 49: Torsional Mode (434 kHz) ... 62
Figure 50: FEA Thermal Time Constant with Constant Heat Dissipation ... 63
Figure 51: Microscope Setup with Probe and ZIF Holder ... 64
Figure 52: Probe Needle Ready to Break 2 μm Poly1 Tether ... 65
Figure 53: Wiring Box with Attached Ribbon Cable ... 66
Figure 54: Stepper Motor Control LabVIEW Front Panel ... 67
Figure 55: Stepper Motor Control LabVIEW Code ... 68
Figure 56: Microscope Setup with Attached Stepper Motor ... 69
Figure 57: Allegro A4983 Stepper Motor Driver ... 70
Figure 58: Out-of-plane Focus Measurement Flowchart ... 71
Figure 59: Nanovea Optical Profiler (Nanovea Documentation [33]) ... 72
Figure 60: Nanovea Hardware (d'Entremont [34]) ... 74
Figure 61: White Light Axial Chromatism (Nanovea Documentation [33]) ... 75
Figure 62: Area Scan of the 2DTA in the Off Position ... 77
Figure 63: Maximum Lift Position Area Scan Isometric ... 79
Figure 64: Height Measurement Cross Section Explanation ... 80
Figure 65: Planar Displacement Measurement Cross Section Explanation ... 81
Figure 66: Optical Profiler Scan ... 82
Figure 67: Stuck VTA ... 83

Figure 68: Unstuck VTA 83
Figure 69: 2DTA Displacement versus Actuator Current Compared to FEA Results 84
Figure 70: Overlaid 2DTA Displacement Envelope Comparing Experimental Results to FEA 85
Figure 71: PolyMUMPs Layer Alignment Issues 86
Figure 72: Raw Optical Profiler Data 91
Figure 73: Profile Derivative 92
Figure 74: Displacement versus Voltage for Five Measurement Methods 93
Figure 75: X-Displacement Linear Fits 94
Figure 76: Example of Images when Varying the Focal Plane. The In-Focus Image is Frame 50 96
Figure 77: Normalized Autocorrelation Algorithm 98
Figure 78: Tenengrad Algorithm 99
Figure 79: Normalized Variance Algorithm 100
Figure 80: Laplace Algorithm 101
Figure 81: Overlaid Autocorrelation Results 103
Figure 82: Zoomed in Autocorrelation Algorithm with Curve Fit 104
Figure 83: CV1 Autocorrelation Algorithm results compared to measured Optical Profiler Measurements 105
Figure 84: CV1 Normalized Variance Algorithm results compared to measured Optical Profiler Measurements 106
Figure 85: CV1 Tenengrad Gradient Algorithm results compared to measured Optical Profiler Measurements 107
Figure 86: SEM Picture of a Shuttle Assembly 109

Abstract

This thesis examines the development and testing of a novel 2 DOF (Degrees of Freedom) thermal actuator using Micro Electro Mechanical Systems (MEMS) technology. A out-of-plane displacement measurement technique based on optical focus adjustments is also implemented and tested. In-plane displacement measurement techniques are also compared.

Existing MEMS actuator can either move in-plane or out-of-plane but no reported actuators were found to move in a user selectable combination of both domains. The novel actuator fabricated using the PolyMUMPs process is capable of displacements of 5 μm out-of-plane and 1.5 μm in-plane. A Finite Element Analysis (FEA) was performed as a proof of concept prior to physical construction. FEA was also used to characterize the actuator.

Measuring out-of-plane displacements of MEMS devices is difficult to accomplish using only a standard microscope and camera setup. Methods have included tilting the chip so the vertical motion has a planar component. The most common commercial measurement technique uses interferomery but special expensive equipment is necessary. A method adapted from biological autofocus is proposed in which multiple images (100+) are taken at various focal planes. An algorithm is applied which extracts the most focused image. An out-of-plane displacement measurement can be extracted between two image sets. Results were compared to optical profiler measurements and the results had an average error of 0.47 μm

A comparison of planar displacement measurement methods, which included two variations of both edge detection and pattern matching along with measurements using the optical profiler, was accomplished. Consistent planar displacement results were collected for all techniques except for the simple edge detection.

List of Abbreviations and Symbols Used

2DTA	2 degree of freedom thermal actuator
3D	Three-Dimensional
A	Area
C	Specific heat
CAD	Computer Aided Design
CCD	Charge-Coupled Device
CMC	Canadian Microsystems Corporation
CMOS	Complementary metal–oxide–semiconductor
DAQ	Data Acquisition Card
DLP	Digital Light Processing
DOF	Degrees Of Freedom
DRC	Design Rule Check
E	Young's Modulus
LCD	Linear Comb Drive actuators
F	Force output
f_{3db}	Cut-off frequency
FEA	Finite Element Analysis
g	Spacing between electrostatic fingers
GUI	Graphical User Interface
HF	Hydrofluoric acid
HSI	Hue, Saturation, and Intensity image format
i	Image pixel value
k	Thermal conductivity; Stiffness

K	Kelvin unit
L	Arm length
L-Edit	Layout-Editor
LCD	Linear Comb Drive
MEMS	Micro Electro Mechanical Systems
MetalMUMPs	A metal-based MEMS process
MUMPs	Multi-User MEMS Process
n	Number of electrostatic fingers
NI	National Instruments
P	Cross-sectional perimeter
PP	Parallel plate actuator
PGA	Pin Grid Array
PGR	Point Grey Research
PM	PolyMUMPs
PolyMUMPs	A multi-layer polysilicon based MEMS process
PWT	Pulse Width Train
q	Heat transfer rate
r	Thermal actuator gap distance
R	Arm resistance
R_s	Sheet Resistance
RGB	Red, Green, Blue image format
RIE	Reactive Ion Etching
ROI	Region of Interest
S	Image pixel value after Sobel operator
SCS	Single Crystal Silicon

SEM	Scanning Electron Microscope
SOIMUMPs	A single layer silicon-on-insulator MEMS process
SOI	Silicon on Insulator
STA	Standard Thermal Actuator, Two-arm Thermal Actuator
t	Polysilicon layer thickness
T	Temperature
TA	Thermal Actuator
V	Voltage
VI	Labview Virtual Instrument
VTA	Vertical Thermal Actuator
w	Vertical displacement COMSOL variable
ZIF	Zero Insertion Force
α	Coefficient of thermal expansion
Δ	Arm elongation due to thermal expansion
Δ_z	Vertical spacing between the actuator and the chip's substrate
ε_{air}	Dielectric constant of air
ρ	Density
Θ	Chevron arm angle
Ω	Ohm
σ	Electrical Conductivity
τ	Thermal time constant
ν	Poisson's ratio
μ	micro, image mean

Acknowledgements

I would like to begin by thanking my supervisor Dr. Ted Hubbard for the excellent guidance provided during my two years working in his lab. His eagerness and enthusiasm is well known throughout the mechanical engineering department. I would also like to thank both Dr. Marek Kujath and Dr. Yun Ma for their guidance on my supervisory committee.

A thank you to Peter Jones and Jon MacDonald for their hardware and electrical knowledge, which was essential for my research. I would also like to thank all my colleagues, especially Neil Ellerington, Craig Arthur, and Rishad Irani who have all aided me in my research.

Last of all, I would to thank all my friends and family for providing support during my studies.

Chapter 1: Introduction

1.1: Objective

The thesis is concerned with MEMS (Micro-Electro Mechanical Systems) Thermal Actuators (TA) and displacement measurement techniques using a standard microscope and camera setup.

Many MEMS devices rely on actuators to operate, such as long range conveyors and adjustable micro-mirrors. A suitable actuator should have ample displacement and force to accomplish the desired task. The aim of this research was the development of multiple degrees of freedom TAs for use as shuttle drivers using the MEMSCAP PolyMUMPs process.

Measuring out-of-plane displacements of MEMS devices has always been difficult especially if user probe input is required on-chip. Optical focus based Z-displacement (out-of-plane displacement) measurement techniques with an optical camera were compared. The repeatability of various in-plane displacement measurement techniques was also investigated.

1.1.1: Project Scope

This work includes the basic theory behind the operation of thermal actuators as well as lift and slide conveyors. A novel actuator capable of 2 DOF (Degrees of Freedom) motion was developed and characterized. A comparison to previous work was also performed. Finite Element Analysis (FEA) was carried out to determine the actuator

characteristics. Displacement measurement results in both the in-plane and out-of-plane directions was discussed along with the actuators suitability as a shuttle driver.

1.1.2: **Author Contribution**

MEMS actuators have long been developed and researched, but to the author's knowledge, none have been reported to produce significant user selectable 2 DOF displacements. Previously, similar thermal actuator geometries have been employed but only out-of-plane motion was reported [1].

Unconventional (to MEMS research) techniques used in the biological sciences for height measurement by optical focus adjustment were applied by the author to MEMS devices. Four of the more popular algorithms were tested and their accuracies compared. The suitability of such optical displacement measurement techniques for MEMS are evaluated against out-of-plane measurements collected using a commercial optical profiler.

1.2: **What are MEMS?**

MEMS are small mechanical structures built using deposition and photolithography along with various etching techniques. Common uses include sensors and actuators. With their very small sizes (~1-3 µm feature size) they can be embedded in many systems. Their light weight also makes them extremely portable or redundant if needed.

MEMS actuators are used in radio frequency communication devices as variable capacitors by finely tuning the distance between two parallel plates (Girbau [2]).

Actuators are also used extensively in the manufacture of Digital Light Projection (DLP) televisions where they control micro-mirrors. Similar micro-mirrors have also found themselves used in optical switching particularly in the fibre optic communication field.

Another major use of MEMS is the construction of various sensors including accelerometers, chemical and pressure sensors, and flow meters. Accelerometers are used in many devices including modern smartphones, automobiles, and cameras to name a few. They can also be uses in navigational equipment in the form of inertial guidance systems where the velocity and heading can be determined from a 3-axis accelerometer.

MEMS devices are also implemented in ink jet printer heads where they act as small resistors [3]. Because of their small sizes, they can rapidly heat and cool. With silicon being a semiconductor, it features significant resistance and can be heated via joule heating. The heater segments can be heated to temperature approaching 1000 K, boiling the ink and creating a high pressure bubble, ejecting the ink from a nearby nozzle.

The advantages of using MEMS devices, other than their small size, include a cheap cost and being disposable. They are constructed using a batch process where 1000s if not millions can be built at a given time, resulting in lower unit cost. A three axis accelerometer can be purchased for $20 CDN in 2011 [4].

Even though MEMS device are already widely used, the development of future device depends on the understanding on how common physics scales with size. Smaller devices have large area/volume ratios compared to their macro counterpart. As a result, surface force such as friction and electrostatic forces are becoming more important than body forces such as gravity and inertia. One problem plaguing designers is stiction. It

consist of the combination of van der waals forces, the capillary effect, electrostatic forces, and hydrogen bridging forces which bonds two parallel plate together making it near impossible to free these devices [5][6].

MEMS devices are generally grouped in either Bulk or Surface micromachining. The first generally consist of etching the substrate and top layer to create features. Advantages include simplicity and the ability to create thicker structures. Surface micromachining usually begins with a blank silicon wafer where layers can be deposited then etched to create the feature. Some processes such as PolyMUMPs include three structural layers on top of the wafer.

1.2.1: **PolyMUMPs Process Overview**

A very common MEMS technology is the Multi User MEMS Process (MUMPS) developed by MEMSCAP, which uses a well defined surface micromachining commercial process. It is designed for flexibility over a wide range of uses. One of the MUMPS variation is called PolyMUMPs and uses three separate layers of polysilicon topped by a thin layer of gold all bonded to the main silicon wafer. Figure 1 show the multiple layers along with the silicon oxides separating each layer. The dimple represents a 0.75 µm hole etched in the oxide not an additional oxide layer.

The flexibility comes from the ability to etch the oxide before the polysilicon layer is applied, bonding it to the previous layer. As a result, many different types of devices are being built including actuators, sensors, and mirrors.

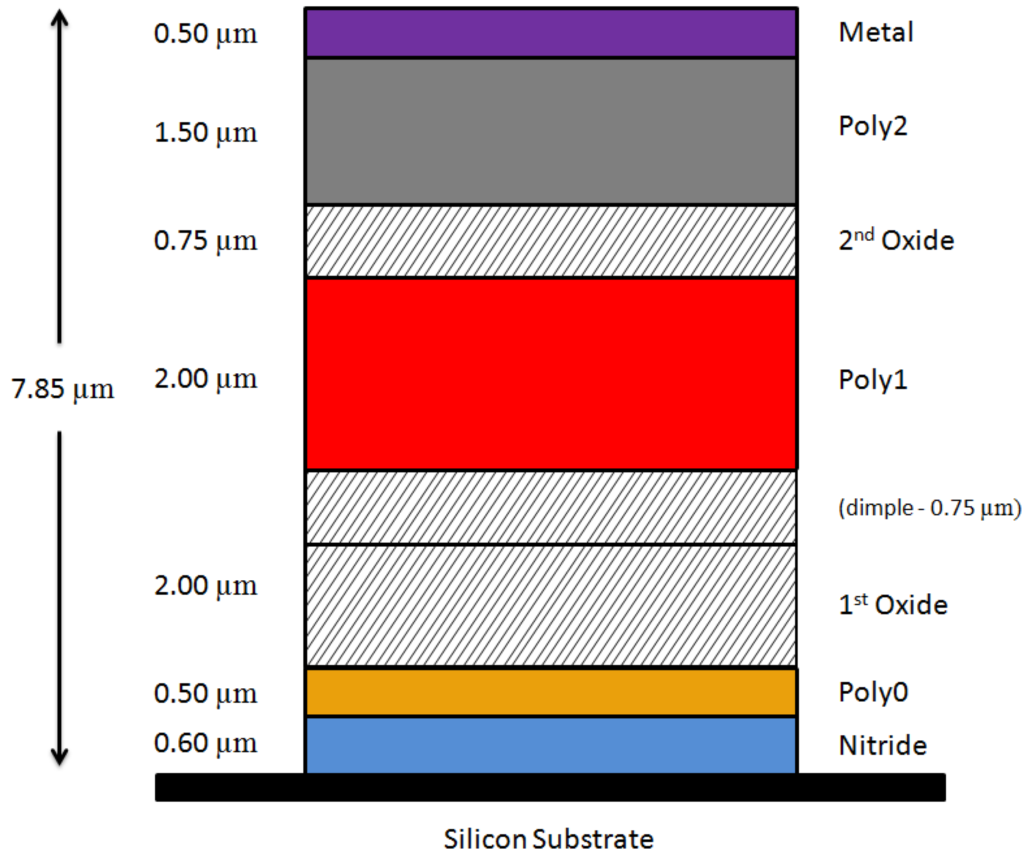

Figure 1: PolyMUMPs Layers

The construction of a PolyMUMPs chip is a combination of layer depositions and various wet or ion etchings. The process begins with a thick silicon wafer. Layers are then deposited and etched to the desired shapes using photolithography. To add a layer, they begin by covering the entire wafer by the polysilicon layer followed by photoresist as shown in Figure 2. The etching mask pattern is created by exposing the photoresist to light.

Figure 2: First Step of the PolyMUMPs Process: Deposition of Poly0 and Photoresist (Memscap [7])

The exposure of the photoresist to the appropriate pattern followed by the development of the photoresist prepares the appropriate etching mask for the underlying layer. Figure 3 shows the chip still containing the entire Poly0 layer with the patterned photoresist.

Figure 3: Patterning of the Photoresist in Preparation to Etch Poly0 (Memscap [7])

Reactive Ion Etching (RIE) is used to etch the polysilicon leaving only the polysilicon under the photoresist. They then remove the remaining photoresist (Figure 4) making the chip ready for the application of the following layer, in this case Oxide1.

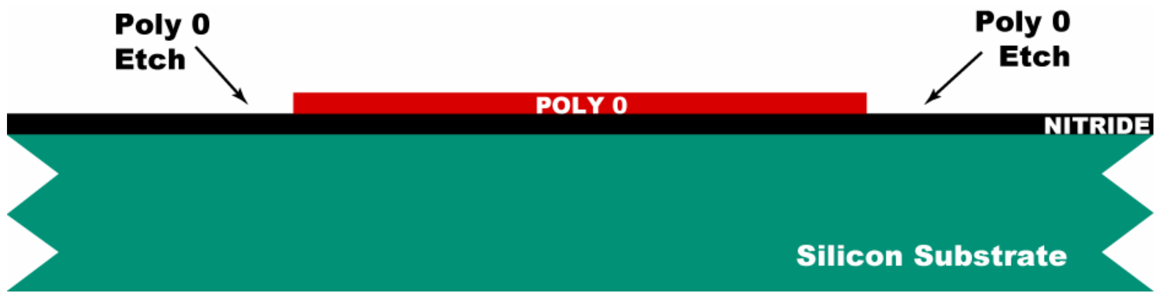

Figure 4: Poly0 Etched and Photoresist Removed (Memscap [7])

The process outlined above is then repeated 5 additional times to build up the remaining layers. Figure 5 demonstrates the cross section of all PolyMUMPs layers before the wet etching of both oxide layers. The blanketing effect can also be seen, which happens when a layer gets deposited partially on top of another one, e.g. 1st oxide over the Poly0 layer. It creates a step height in the structure.

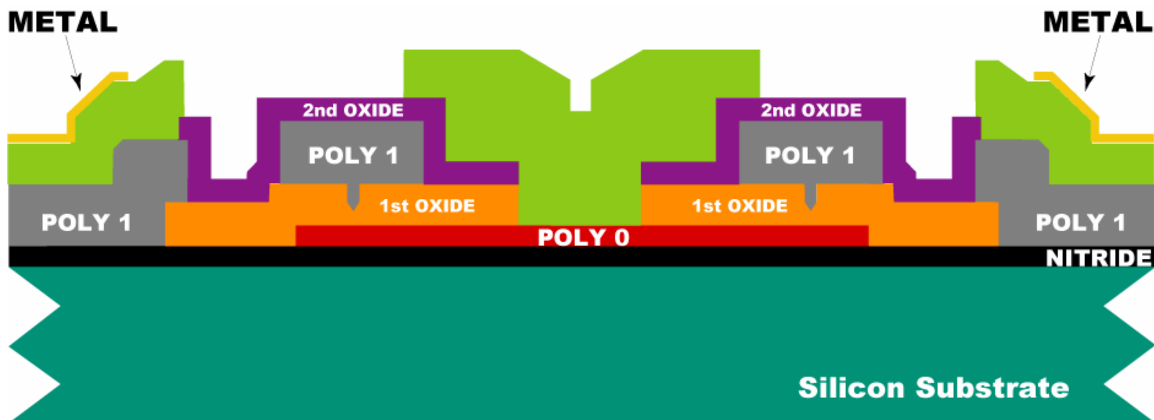

Figure 5: Build-up of All PolyMUMPs Layers before Oxide Removal (Memscap [7])

Finally the Oxide layers are removed by wet etching using room a temperature bath containing 49% hydrofluoric acid (HF). The released structure can be seen in Figure 6, notice the two center portions of Poly2 are lowered compared to Figure 5 now the oxide is gone.

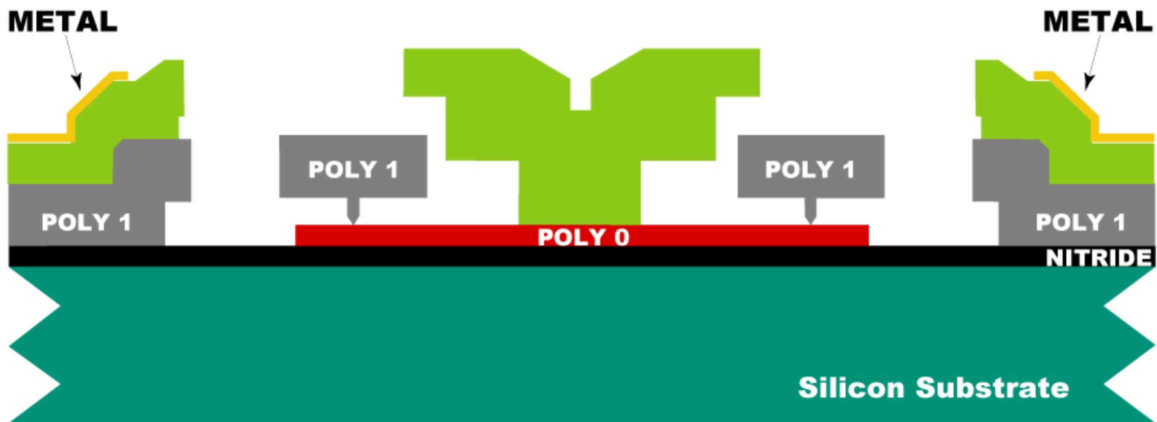

Figure 6: Finalized Process (Memscap [7])

1.3: MEMS Actuators

Since its inception in the late 80's, many different types of PolyMUMPS actuators have been designed and tested. Most of these actuators can be lumped into two broad categories, electrostatic and thermal actuators.

Electrostatic actuators use the electrostatic force between two differently charged plates. In PolyMUMPs, the thickest structure can only be 3.5 um high by combining both the Poly1 and Poly2 layers. As a result, many small arms must be used to accumulate enough area to produce a usable force. These actuators can produce very large forces but requires a large chip area.

Thermal actuator use either differential thermal expansion of different arms such as the standard TA, or symmetry to force the displacement in one direction such as the chevron actuator. Both designs have a major advantage over electrostatic actuators, smaller size, but they are very inefficient. In order to be actuated to their full potential they must be heated to around 1000 ^{o}C.

1.3.1: **Parallel Plate**

If two parallel plates are vertically separated, electrostatic force produce large forces perpendicular to the plates, pulling them together. In order to implement this in a planar device, parallel plate (PP) comb drives actuators split the plate into interdigitated fingers. The electrostatic forces are still perpendicular to the comb fingers direction but the forces are now lateral and not vertical. The disadvantage of the PP actuator is its small displacement. The governing equation for the actuator force is seen below in (1), [8][9].

$$F = \frac{n\varepsilon_{air}A}{2}V^2\left(\frac{1}{{g_1}^2} - \frac{1}{{g_2}^2}\right) \tag{1}$$

Where F is the actuator force (N), n being the number of fingers, ε_{air} represents the dielectric constant of air (F/m), A is the finger area (m^2), V being the voltage (V), g_1 and g_2 being the distance between fingers on each side. g_2 being the larger of the two.

Electrostatic force is a function of gap distance squared; therefore the starting location of the plates must be within a few microns of each other, with an offset to one side. The offset produce a preferential actuation direction towards the smaller gap. The voltage levels needed for actuation usually ranges in 60-100 V range but with no current flow thus little power is dissipated (Sameoto [9]).

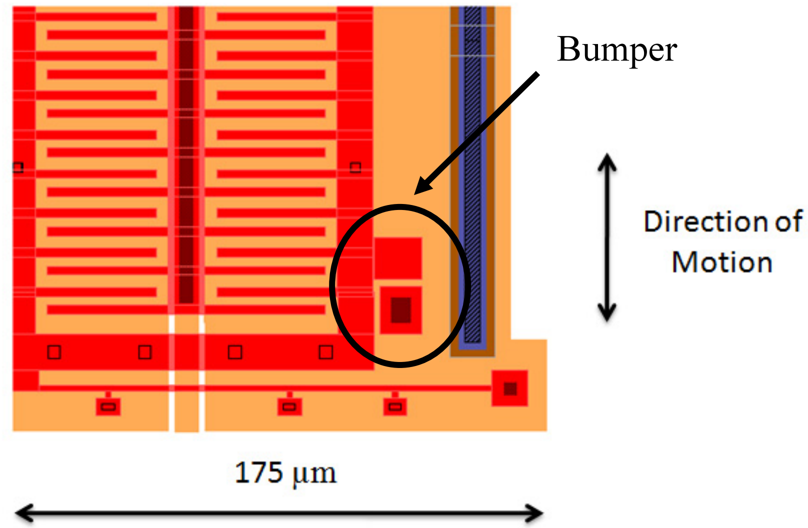

Figure 7 : Parallel Plate Actuator

PP actuators also suffer from pull-in which is caused when the plates become too close together. The spring force holding them apart varies linearly with distance while the electrostatic force is of second order. When a small gap change increases the electrostatic force to a greater value than the spring force, the plates snap together. To prevent such occurrence, bumpers are placed as can be seen in Figure 7. Since the electrostatic force is very sensitive to gap distance, the starting gap can only be a few microns limiting the displacement of the entire actuator to 1-3 μm (Sameoto [9]).

1.3.2: **Linear Comb Drive**

Linear Comb Drives (LCD) operate on the same principle as the PP actuator mentioned above except the displacement is along the comb fingers as opposed to perpendicular to them (Figure 8). This allows much greater actuation displacement as they are not as susceptible to pull-in as the PP actuators. The force of a LCD actuator can be calculated by equation (2), [8][9].

$$F = \frac{n\varepsilon_{air}t}{g}V^2 \qquad \textbf{(2)}$$

Where F is the actuator force (N), n being the number of fingers, ε_{air} represents the dielectric constant of air (F/m), t is the finger height (m), V being the voltage (V), and g being the gap distance (m) between fingers on each side.

The consequence of larger displacements is smaller actuation forces because fewer surfaces are producing this displacement. They must also use compliant springs to ensure the combs do not move towards each other while still allowing the combs to move in their intended directions.

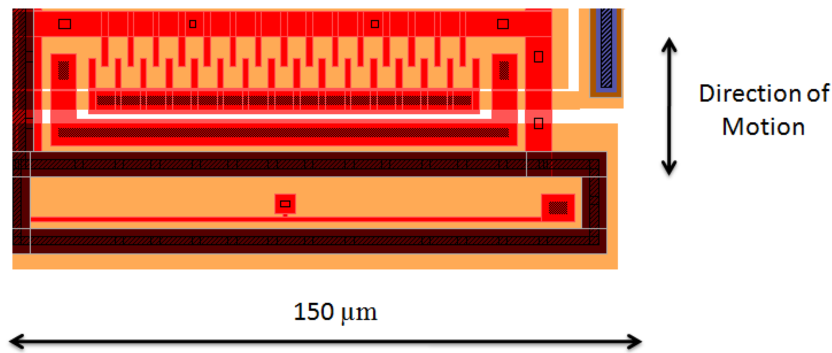

Figure 8: Comb Drive Actuator

Reported displacements for LCDs have been reported from 30-60 µm at actuation voltages of 25-40 V by Zhou [10].

1.3.3: **Standard Thermal Actuator**

MEMS Standard Thermal Actuators (STA) operate on the differential thermal expansion of two polysilicon arms. Figure 9 demonstrates the geometry of an STA built using the Poly1 layer in the PolyMUMPS design. A voltage is applied to the two Poly0 pads on the left causing current to flow through the actuator. The thin arm, called the hot

arm, has a higher resistance and will therefore reach higher temperatures due to Joule Heating. The thicker cold arm has a lower power density and will only partially heat (Hickey [11]).

Since a thick arm also resists bending, a flexure is incorporated at the base of the cold arm. It is a very important feature of the STA as its length limits the deflection of the entire TA. Also, it cannot be thinner than the hot arm as it will reach higher temperature and be the limiting feature.

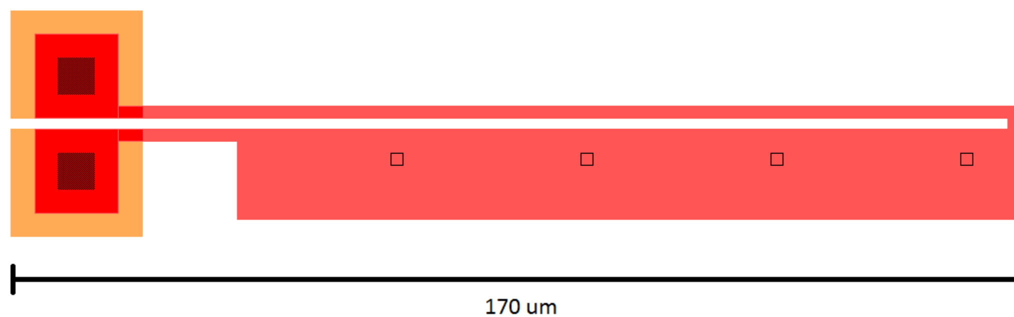

Figure 9: Standard Thermal Actuator

STAs cannot be positioned in parallel for higher force because the displacement is not perfectly linear. The displacement is the result of bending at the cold arm flexure meaning the displacement is really an arc. Coupling has been attempted by attaching compliant springs to the TA tip as seen in Figure 10. Energy generated within the hot must be used to deform the coupling spring instead of the cold are flexure resulting in lower displacement.

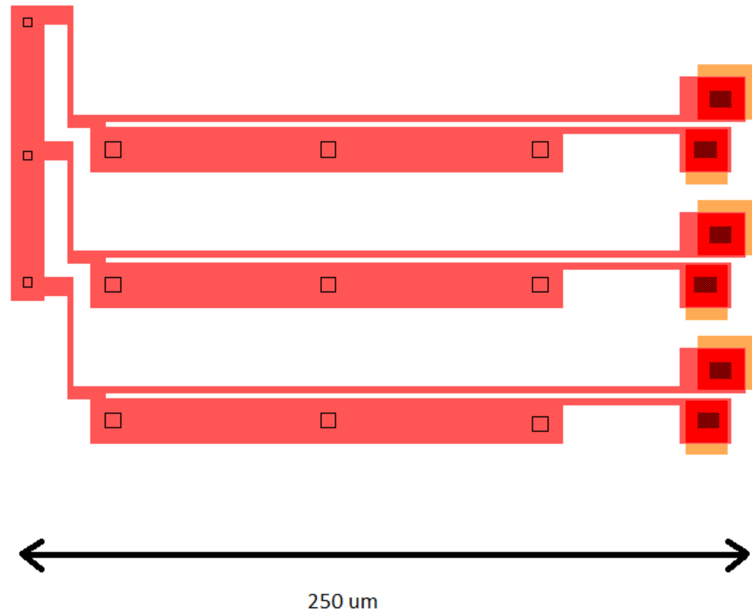

Figure 10: Parallel TA

Current STA designs can attain in-plane displacements of 5-10 μm (Lai [12]) (Venditti [13]), while VTAs typically reach around 9 μm (Lee [14]). The displacement is heavily dependent on the distance ‘r’ between the hot and cold arm (Figure 11). The geometric amplification is roughly equal to the actuator length divided by the gap distance ‘r’ (Hickey [15]). A common TA would be 200 μm long with a gap of 4 μm resulting in an amplification of 50 the hot arm expansion.

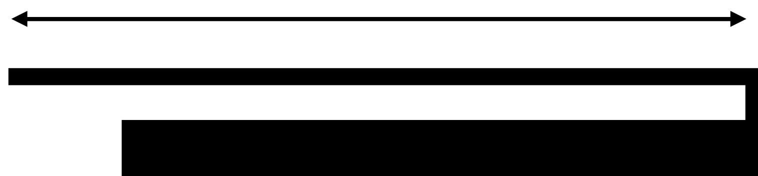

Figure 11: TA Variables

1.3.4: **Chevron Actuator**

A second type of TA is called the Bent Beam or chevron actuator (Figure 12). It does not contain both a hot and cold arm as does the STA but instead every arm is heated. It produces displacement by angling the arms at a very shallow angle from the horizontal, usually from 6-12 degrees (Hickey [15]). The geometric amplification is proportional to $1/\theta$. For a 6° angle the amplification is roughly 10 times resulting in displacement, ranging in the few microns.

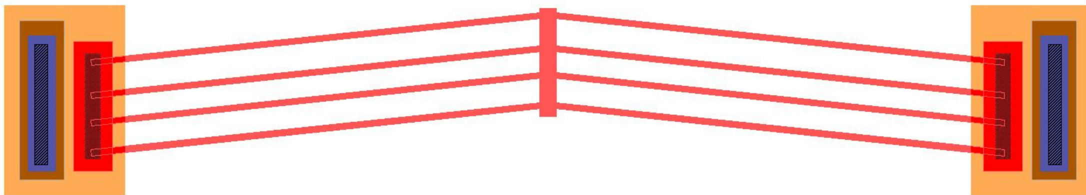

Figure 12: Standard 200 µm arm Chevron Actuator

PolyMUMPs Chevron actuators are also commonly built using the poly1 layer, meaning they are 2 µm thick as well as 2 µm from the substrate. Common arm thicknesses are either 2 or 3 µm. As opposed to STAs they can be constructed in parallel because their displacements are linear. It is common to group 4 or more chevron together as seen in Figure 12, displacements are unaffected but force can be greatly increases by having multiple chevrons. Lai [12] reported a force of 120 µN for a 300µm wide, 8 parallel chevron actuators.

Table 1: Summary of Existing In-Plane Thermal Actuators

Paper	Voltage (V)	Process	Type	Disp. (µm)	Area (mm^2)
Hickey [11]	6	PM	STA	10	0.0038
Lai [12]	8	PM	Chevron	3	0.012
Venditti [13]	6	PM	STA	±6	0.00264
Chuoi [16]	125	CMOS	LCD	10	0.6
Zhou [10]	35	PM	LCD	60	1

1.3.5: **Existing Vertical Thermal Actuator (VTA) Work**

For some MEMS related tasks, in plane motion is not enough, vertical motion is needed. Common VTAs are very similar to the STA in that they both contain a hot and cold arm. The gap distance separating both arms is the vertical height difference in layers for the VTA (Atre [17] and Girbau [2]). The VTA has two cold arms which provide lateral stability instead of one as in the STA (Figure 13).

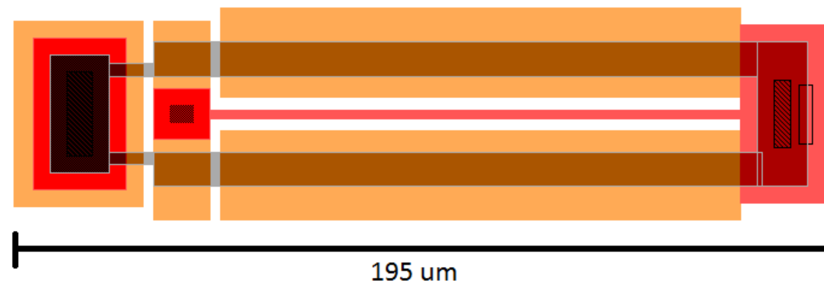

Figure 13: Vertical Thermal Actuator (VTA)

PolyMUMPs is a common process and, many research teams have designed VTAs capable of out of plane motion (Tsou [18] and Yan [19]). Tsai [20] developed an out-of-plane rotational actuator capable of rotations of ±2.87° using the silicon-on-insulator (SOI) process.

Some very large MEMS VTAs have reported displacement on the order of 600 μm using custom bi-morphs (Wu [21]). Four Al/Pt/SiO_2 flexures are attached to a large center pad. The entire device has a footprint of 2.5 mm which is an order of magnitude larger than most other MEMS device mentioned here. Although it features large displacements, it is very slow, having a time constant of 25 ms.

Bar type VTAs, as seen in Figure 14 taken from Chen [22], have also been built in which the center of the bar is slightly elevated.

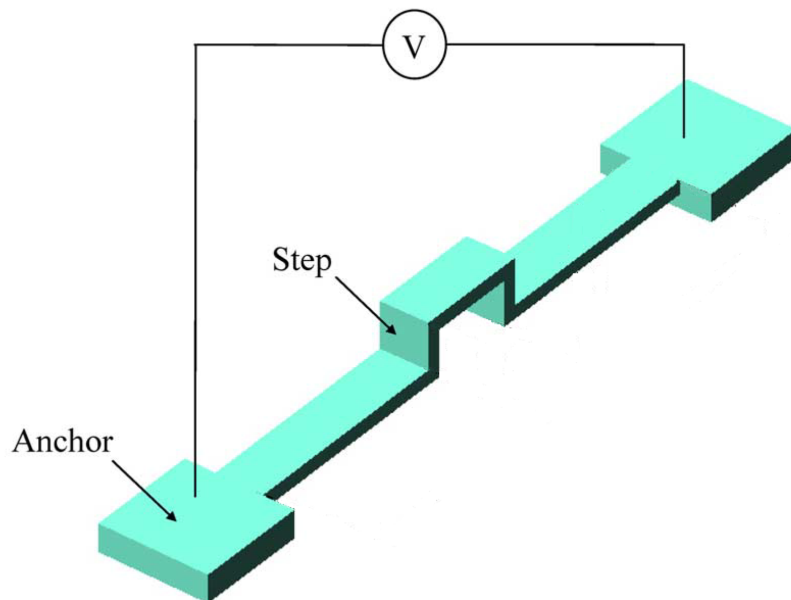

Figure 14: Bar Type TA adapted from Chen [22]

It operates on the same principle as the chevron TA by having a fully heated device with a preferential buckle direction. A PolyMUMPs version was built by Atre [17] which had 10 μm of displacement. As opposed to standard VTAs, the displacement versus voltage curve is in the shape of a square root function opposed to exponential. Chen [22] created a bar TA from a single layer of single crystal silicon (SCS). Displacements of 20 μm where measured with a total actuator length of 600 μm. The

entire TA was buckling for these levels of displacement. FEA had only predicted approximately 2 μm. Because bar TA are fixed at both ends, they exhibit higher natural frequencies at approximately 90 kHz measured by laser Doppler vibrometer.

Three armed actuators have also been developed. One developed by Girbau (Figure 15) was described as a hybrid between the traditional in-plane buckle-beam actuator and the vertical hot–cold actuator [2].

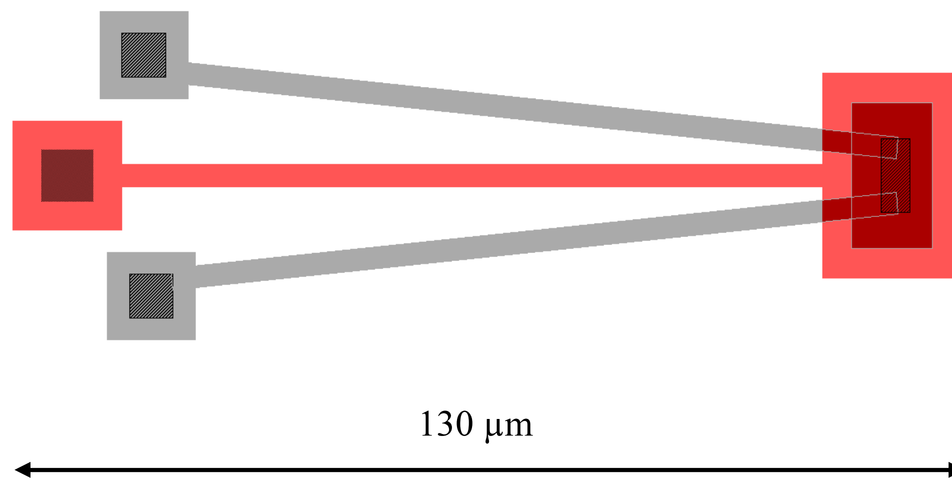

Figure 15: 3 Armed VTA

Power is applied to the chevron with the center arm remaining cold. As in a standard VTA, the cold arm has a different height from the substrate, therefore when the chevron tries to actuate in-plane it is forces up. By angling the two outer arms, larger normalized displacements can be achieved. At 8V, 10 μm of displacements has been achieved with a 126 μm arm.

Li [23] created a 3 arm parallel VTA using the SOIMUMPS process. It had a total length of 1800 μm and an effective height form the substrate of 200 μm. As opposed to common VTAs which have one hot arm and two cold arms; this actuator had two lower

hot arms and only one cold arm. As a result, no energy is wasted by slightly heating the cold arms. They concentrated on dynamic response but reported static measured displacements of 5 μm. Dynamic measurements were conducted using a laser scanning vibrometer. The 0-90% rise time was measured at 17.3 ms.

Bi-directional actuators are built using a variety of different processes from common well defined process such as PolyMUMPs and MetalMUMPs while others use custom in-house processes. One such actuator is depicted below in Figure 16 which was taken from Chen [1].

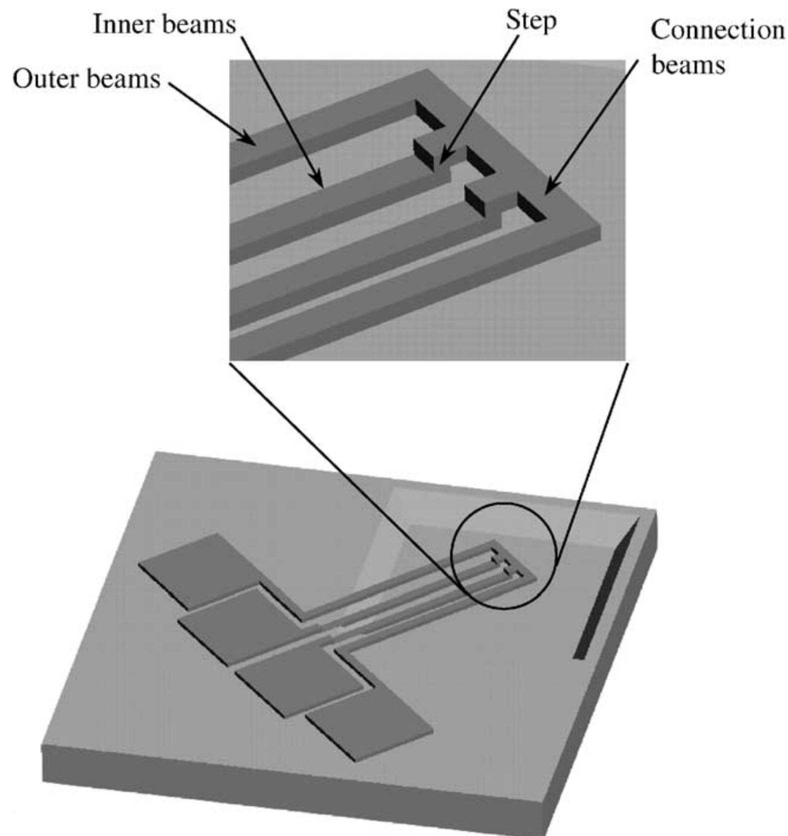

Figure 16: 4 Armed Bi-directional VTA from Chen [1]

A VTA containing four arms has been developed by Chen [1]. The current can flow through either the upper or lower two arms creating both the positive or negative

vertical displacements. The outer arms are raised higher than the center two arms. Current can flow either in the two lower arms causing a upwards displacement or in the upper two arms causing a downwards motion. Chen [1] reported displacement of ± 7 μm with an overall actuator length of 240 μm and a layer thickness of 2 μm. The actuator was fabricated using a custom process with one layer of SCS. A similar actuator was also developed in the PolyMUMPs process by Yan [19], which had four laterally spaced arms; they overlaid the lower Poly1 and higher Poly2 arms. Similar out-of-plane displacements of 5-6 μm were reported with no mention of downward capabilities.

A third type of bi-directional actuator developed by Michael [24] consists of 1200 by 100 μm microbridge attached to the substrate by tri-layer pre-stressed spring. The bi-stable actuator toggles between it's up and down position with thin silicon legs at each end. The actuators two toggle points are 16 μm either above or below its initial location. The size displacements are impressive but the actuator is both extremely large and slow, taking approximately 30ms to toggle.

Out-of-plane displacements have also been achieved using the SOI process. This process has two layers, a lower 15 μm thick layer SCS and a 2 μm thick layer of polysilicon. As opposed to the thermal actuators previously mentioned, this rotational actuator is electrostatic. Both silicon layers form one comb finger and are isolated from each other by an oxide layer. The comb drive can them be operated vertically as opposed to in-plane by applying the voltage potential across the upper electrode of one comb and bottom electrode of the other. The center pad is fixed by a spring therefore when one comb attempts to move vertically, a rotation is created (Tsou [18]). Static rotation angles

of -1° to 0.6° have been reported at 100 V. When operating the actuator at its first resonant frequency (10.46 kHz), a scanning angle of 70° has been reached.

A second out-of plane rotational actuator using MEMSCap's MetalMUMPS process has also been developed (Tsai [20]). It operates on similar principles as Tsou [18]. It is also an electrostatic actuator with the center pad being fixed by a torsion bar on the substrate. As the combs are attracted, the center platform rotates about the torsion bar. Displacements of ±2.87° have been measured by optical refocusing with an attached optical scale. The first natural frequency was measured at approximately 4.75 kHz by method of edge blurring.

Table 2 below summarizes existing VTA designs. The processes covered PolyMUMPs (PM), SOIMUMPS (SOI), MetalMUMPS (MM), Single Crystal Silicon (SCS), and Bi-morph actuators.

Table 2: Summary of existing VTAs

Paper	Voltage (V)	Process	Type	Disp. (µm)	Length (µm)	Width (µm)	Disp. /Area (µm/ µm^2)	Natural Freq. (kHz)
Atre [17]	8	PM	Thermal	10	126	40	0.00198	-
Chen [1]	5	SCS	Thermal	± 7	240	70	0.00083	-
Chen [22]	54mW	SCS	Thermal	20	600	27	0.00123	-
Girbau [2]	4	PM	Thermal	2.25 FEA	195	165	0.00007	-
Li [23]	-	SCS	Thermal	5	1800	-	-	17.3 ms
Michael [24]	9	Bi-morph	Thermal	±16	1200	~300	0.00009	-
Tsai [20]	105	MM	Electro-static	± 2.87°	2600	250	-	5.05
Tsou [18]	100	SOI	Electro-static	70° dyna-mic	850	400	-	10.46
Wu [21]	5.5	Bi-morph	Thermal	600	~1000	~1000	0.0006	0.5
Yan [19]	9	PM	Thermal	6.25	217	60	0.00048	-

1.3.6: **Vertical Thermal Actuators Theory**

The (VTA) operates very similarly to the STA with the major difference being the cold arms constructed from the P2 layer. Instead of having a planar distance between both the cold and hot arm of the STA, the VTA has an out-of-plane separation. Figure 13 demonstrates a common VTA, notice there are two cold arms to keep the TA from also having an in plane displacement. The P2 layer with the P0 addition is only 0.50 µm higher. Again, the cold arms have flexures close to their anchor points.

As indicated above, the driving force behind TAs is thermal expansion; therefore large temperature differences are created to achieve maximum displacement. Common operating temperature of the hot arm can often be in the 600-1000 K range with 1273 K being reported as the failure limit (Hickey [11]). The coefficient of thermal expansion (CTE) is commonly reported from 2.6-3.5*10^{-6} /K. It is temperature dependant but its variation will not be considered for this thesis. The net expansion of the hot arm follows $\Delta_{net} \sim \alpha_t * L_h * T_{h_{avg}}$, resulting in expansion on the order of 0.1 µm.

The power dissipated within the arm follows ohms law, $Power = IR$, with heat being dissipated mostly along the arms and to the substrate through the air in the form of conduction. Hickey [15] also derived the heat flow equations characterizing the temperature profile along the TA arm as shown in equation (3). Where T_i, P_i, A_i, L_i, V_i, and R_i represents the temperature (K), cross-sectional perimeter (m), cross sectional area (m^2), length (m), electric potential (V), and resistance (Ω) of the ith arm respectively. k_{poly} is the thermal conductivity $\left(50\frac{W}{mK}\right)$ of the polysilicon layer. C_{poly} represents the specific heat of polysilicon $\left(860\frac{J}{kg*K}\right)$ and ρ is the density of polysilicon $\left(2300\frac{K}{m^3}\right)$. Δz represents the distance (m) from the polysilicon layer to the substrate.

$$\frac{\partial T_i(x)}{\partial t} = \frac{k_{poly}}{C_{poly}\rho}\frac{\partial^2 T_i}{\partial x^2} - \frac{k_{air}P_i/2}{C_{poly}\rho A_i L_i \Delta z}(T_i - T_\infty) + \frac{V_i^2/R_i}{C_{poly}\rho A_i L_i} \tag{3}$$

The three terms on the right hand side of equation (3) represents respectively the heat conduction along the arms, the heat conduction to the substrate through the air layer, and joule heating. The division by 2 in the center term is a shape factor for a square bar above and isothermal surface. Hickey [11] concluded heat conduction thought the arms

and conduction to the substrate represented the majority of heat loss in the actuator. Hickey used a constant Δz of 2 μm but for VTAs this distance changes with displacement. Higher the displacements result in lower heat dissipation. VTAs are very sensitive actuators at higher voltages. Atre [17] performed many simulations with variable gaps along with temperature dependant air properties to investigate this effect.

MEMS device have high surface to volume ratios compared to macro scale devices. It allows them to dissipate heat very quickly and still respond at operating frequencies in the 30-45 kHz range (Hickey [15] and Chen [1]). At the higher frequencies, there is a significant static offset to the displacement is it cannot effectively shed the heat. Time constants for a typical STA was measured at about 160 μs. Being able to operate at these high frequencies makes then suitable for many uses such as variable capacitors, optical switch, and micro positioners (Chen [1]). The low operating voltage of PolyMUMPS thermal actuators (0-10 V) also makes it possible to be driven with TTL or CMOS outputs. Many actuator variations will produce a few microns of displacement at 5V and a few mA.

The common failure modes for thermal actuators are either burn out, when the temperature reaches above the 1273 K mark, or hot arm buckling. The hot arms in either thermal actuator designs are long thin members very susceptible to buckling. The gap distance also affects when buckling will occur. A smaller ‘r’ meaning a larger geometric amplification also results in larger stresses within the hot arm causing buckling at lower temperatures. Hickey [25] studied the effect of varying the gap distance and proposed guidelines for optimum actuator displacement of force. These forces were also measured by various methods. Lai [12] used acupuncture needles and measured their deflection at a

given voltage and compared it to their unconstrained deflection. Maximum forces for a single 200 μm STA was measure at 6 μN and the parallel array of 5 TAs only had 17 μN of force. It displays the inefficiencies of coupling TAs in parallel, as energy is wasted deforming the springs instead of producing displacement.

One common problem with TAs or any long suspended structures in MEMS is stiction. It is most prevalent when high humidity is present but can happen at any time. Since the surface to volume is higher in MEMS device compared to macro objects, surface effect have a large effect. Stiction is dominated the Capillary effect, van der Waal forces, hydrogen bridging forces, and the electrostatic effect (Yan[6], Ellerington [5]). In some circumstance, the actuator can be stuck to the substrate and no solutions exist to free them. Light stiction can be freed to touching the specimen with an acupuncture needle. To prevent stiction, it is common to create 0.5 μm dimples on the underside of large flat structures. The actuator in Figure 9 features four dimples on its cold arm.

It is also possible to use chevrons in order to produce vertical lift by adding what looks like a VTA to the tip of the chevron (Figure 17). These are used when more force is needed since the lifter Poly1 arm remains cold and therefore will not buckle as easily. They are very similar to the actuator developed by Atre [17].

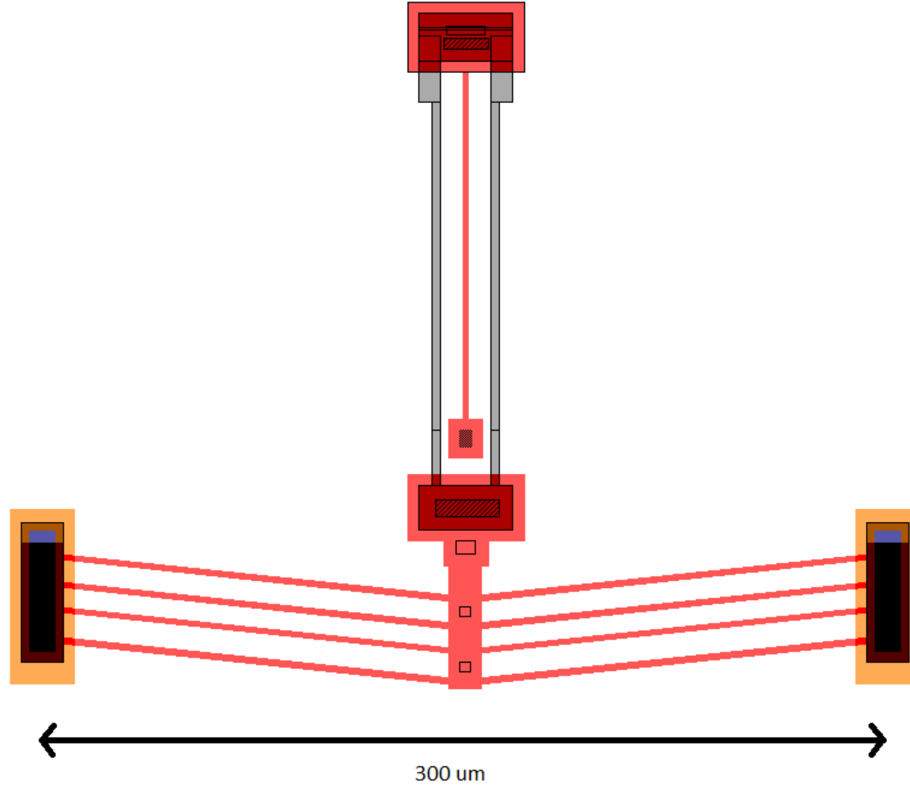

Figure 17: Chevron Vertical Thermal Actuators

1.4: Existing Work on Image Displacement and Focus

There exist simple ways of measuring X-displacement using an optical camera and a sequence of images, but measuring out-of-plane displacement has proven much more difficult. The most common method used involves using an interferometer with accuracies of 20 nm. It is possible to achieve rough height measurements by refocusing the microscope until the best focused image is reached (Tsai [20]). Lee [14] tilted the MEMS chip by an angle θ of up to 45 degrees and measured the tilted x displacement. The Z-displacement is then the measured displacement multiplied by $\sin(\theta)$. In the biological sciences, it is somewhat more common to have autofocusing microscopes

which employ optimal focus determination algorithms to produce a clear image for the viewer. Modern digital cameras also employ such feature. Sun [26]and Santos [27] studied various algorithms to determine which was best suited for their respective fields but no height measurements were extracted. Kaneko [28] used similar methods to construct a 3D image of stacked coin by extracting the in-focus portion of each image along with the height data for those pixels.

The question arises: can existing biological focusing techniques be applied in the MEMS field? And if so, which techniques work best?

Most groups studying autofocus performed comparisons of the different algorithm for their specific purposes. The biological field uses autofocusing microscope for easier viewing of their specimens. Both Sun [26] and Santos [27]employ various algorithms and evaluate them on different aspects such as: accuracy, range, false maximums, peak width, and susceptibility to image noise. Sun compared a total of 18 different algorithms ranging from derivative, statistical, histogram, and intuitive based algorithms. Image pre-processing was also performed to assess the algorithms robustness to sub sampling, random noise and low-pass filtering. Sun concluded the 'Normalized Variance' algorithm was best suited for the raw or noisy images. The other two algorithms mentioned were the 'Tenenbaum Gradient' and 'Autocorrelation' which were useful in specific cases.

Santos [27] determined the best algorithm for the analytical fluorescent image cytometry studies of counterstained nuclei. In total 11 algorithms were compared. Many of the same algorithms Sun [26] used are also present here. He concluded Vollath's 4th (also called Autocorrelation) performed best overall with the 'Normalized Variance' being second best.

Kaneko [28] developed a dynamic focusing lens was used to create real-time 3D images by autofocus technique. The lens used piezoelectric transducers to either push or pull on glass diaphragms filled with Silicon oil. This shifted the focal plane in a calculable fashion within a reported range of ± 4 mm. A novel real-time algorithm called 'one pixel' method was used which can process a frame in 1 ms enabling the camera to take multiple frames before the monitor is refreshed. The setup was tested on four stacked coins but the reported work does not discuss the use with much smaller MEMS devices. The coins also have distinguishable feature all along their surface whereas MEMS actuator only contain focus information along the edge. This lack of features on the flat surfaces makes it hard to produce 3D images from the in-focus portions. Noguchi [29] attempted to extract shape from focus using a 'Sharpness index' but no results could be made with only a standard camera. They also used active illumination by exposing the chip to a specific light pattern. The concluded the image itself could not be used because the flat sections do not contain enough information to determine whether they are in-focus or not.

Chapter 2: 2 DOF Thermal Actuator (2DTA)

2.1: Description

As opposed to the two different TA geometries mentioned earlier, The 2 DOF Thermal Actuator (2DTA) does not contain separate thin hot arms and thick cold arms. It contains four thin (2 um) parallel arms as seen in Figure 18.

Figure 18: Standard 2 DOF Thermal Actuator

The differential expansion needed for displacement occurs from routing the current through different arms. It produce out-of-plane displacements similar to the standard VTA using arms of different vertical spacing as shown in Figure 19.

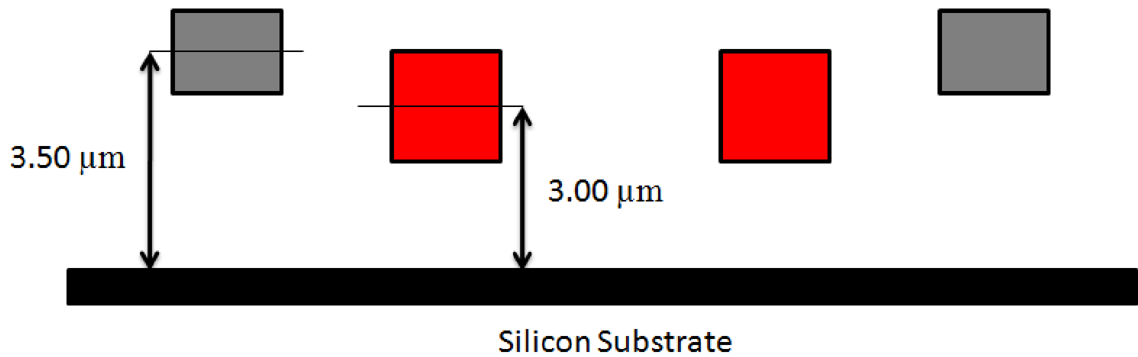

Figure 19: 2DTA Arm Cross-Section in the middle of Figure 18 (enlarged view)

As opposed to most TAs, in which only one voltage potential and the ground must be specified, the 2DTA needs three specified voltages adding more complexity. Each yellow Poly0 pad seen on the left side of Figure 18 is wired separately giving much greater control over displacement direction than standard TAs. The 2DTA has two 150um long Poly2 (gray) arms and two ~175um long Poly1 arms (red). One thing which must be kept in mind is the different resistivity of both the Poly1 and Poly2 layers. The documented resistivity of Poly1 and Poly2 is 10 Ohm /sq and 20 Ohm/sq respectively [7]. This causes the arms to heat at different rates as generated Power $=IR^2$, where I represents the arm current (A) and R is the arm resistance (Ω). The Poly2 is also slightly thinner which does partially account for the higher resistivity.

The initial purpose of the 2DTA was the development of a 2 DOF thermal actuator suitable for shuttle actuation; the shuttle would be supported by an array of 2DTA. It would therefore be able to actuate to specified X and Z positions. Required positions include a pure in-plane X-displacement, a pure out-of-plane Z-displacement and a combination XZ-displacement with enough Z-lift to clear the stationary resting pads for the shuttle between consecutive actuations. Figure 20 below depicts these three configurations.

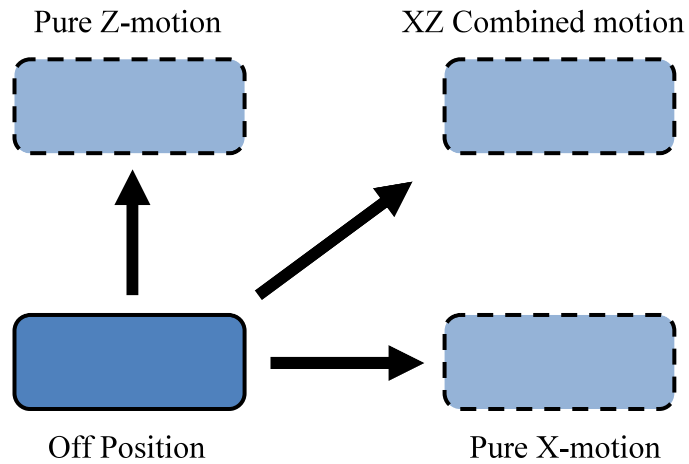

Figure 20: 2DTA in Various Positions

2.2: Actuator Powering Configurations

With four different arms which can be powered, a naming convention must be specified. The descriptive names chosen are shown in Figure 21. Future sections will reference these names.

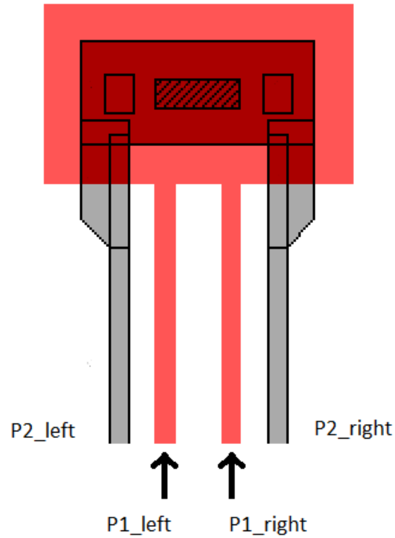

Figure 21: 2DTA Powering Points Names

2.3: **Out-of Plane (Z) Displacement**

The following three figures demonstrate how current is routed in the three most common actuation methods. Figure 22 depicts the pure Z-displacement powering technique. As in a standard VTA, the Poly1 arms must be heated while the Poly2 arms stay cold. With the 2DTA you can simply apply a voltage across both Poly1 arms. Common actuation voltages range from 3-9 V. The Poly2 arms can either be disconnected altogether or a voltage equal to half the applied Poly1 voltage. If the TA is actuated remotely and the Poly2 arms cannot be disconnected, you must ensure no current flows through these arms as it would greatly diminish actuation displacement.

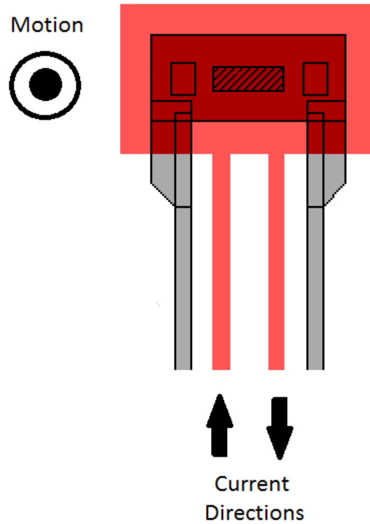

Figure 22: Out-of-Plane 2DTA Powering

2.4: **Simple Planar (X) Displacement**

Figure 23 demonstrates the easiest way to produce an in-plane displacement. Both one Poly1 and one Poly2 arm on the same side must be heated. Usually the Poly1 arm is the ground with the higher potential applied to the Poly2 arm. The downfall of this method is it also produces a small out-of-plane displacement which is caused by the different thermal expansion of the Poly1 and Poly2 arms. The Poly2 arm has a higher resistance and heats to a higher temperature than the Poly1 arm. But Poly1 arm has a larger cross sectional area and can therefore produce larger forces at a given temperature. The Poly1 arm is also slightly longer meaning it required a smaller temperature increase to achieve the same expansion as the Poly2 arm.

The required voltages to ensure no current flow through the other two arms get slightly more complicated. The required voltage ratio for the other two powering points is represented by: $\frac{R_{Poly1}}{(R_{Poly1}+R_{Poly2})}$, where R represents the resistance (Ω) of either polysilicon

arm. The calculated nominal resistances using the parameters specified in the Poly MUMPS handbook [7] are $R_{Poly1} = 975\ \Omega, R_{Poly2} = 1750\ \Omega$. The resulting ratio is approximately 1/3 of the applied Poly2 voltage. The resistance is highly temperature dependant, therefore slight deviations from the calculation are needed to get no current flow in the other two arms during actual operation.

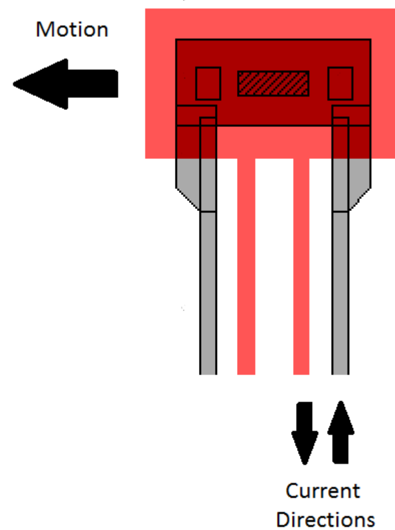

Figure 23: 2DTA Simple X Powering

2.5: Combination X and Z Displacement

The third and most complex way of powering the 2DTA involves heating three of the four arms. With this method, a combination of planar and out-of-plane displacements is possible. In most situations, the grounded Poly1 arm will have the highest temperature and therefore should be closely monitored to ensure the current does not exceed 3.00 mA which would cause permanent structural damage. By varying the voltage about the zero current voltage derived in case 2 on the second P1 arm, you can either increase or decrease the Z-displacement. To achieve a pure X-displacement, P1_left must be lower

than the zero current voltage. This decreases the current through P1_right and increases the current through P2_right causing a downward moment. By increasing the P1_left voltage the opposite occurs. The current through P1_right increases and P2_right decreases causing an enhanced Z-displacement.

The P2_left voltage required for zero current flow now depends on the two applied voltages (P1_left and P2_right), $\frac{R_{Poly1}V_{Poly2}+R_{Poly2}V_{Poly1}}{R_{Poy1}+2R_{Poly2}}$.

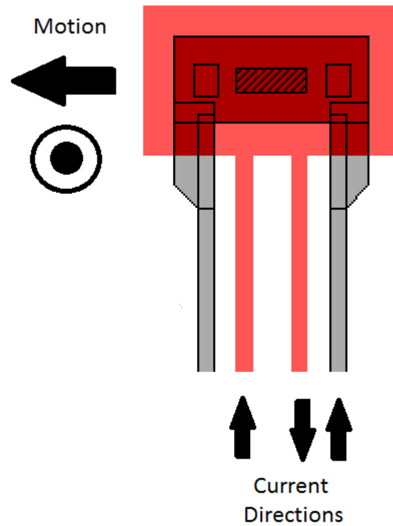

Figure 24: 2DTA XZ-Displacement Powering

2.6: **Fabricated Device**

The 2DTA shown in Figure 18 has been constructed and tested. A Scanning Electron Microscope (SEM) was used to capture clear images. Figure 25 shows the standard 2DTA, it feature 2 µm wide Poly1 and Poly2 arms. The center Poly1 arms are 195 µm long while the outer Poly2 arms are 175 µm long.

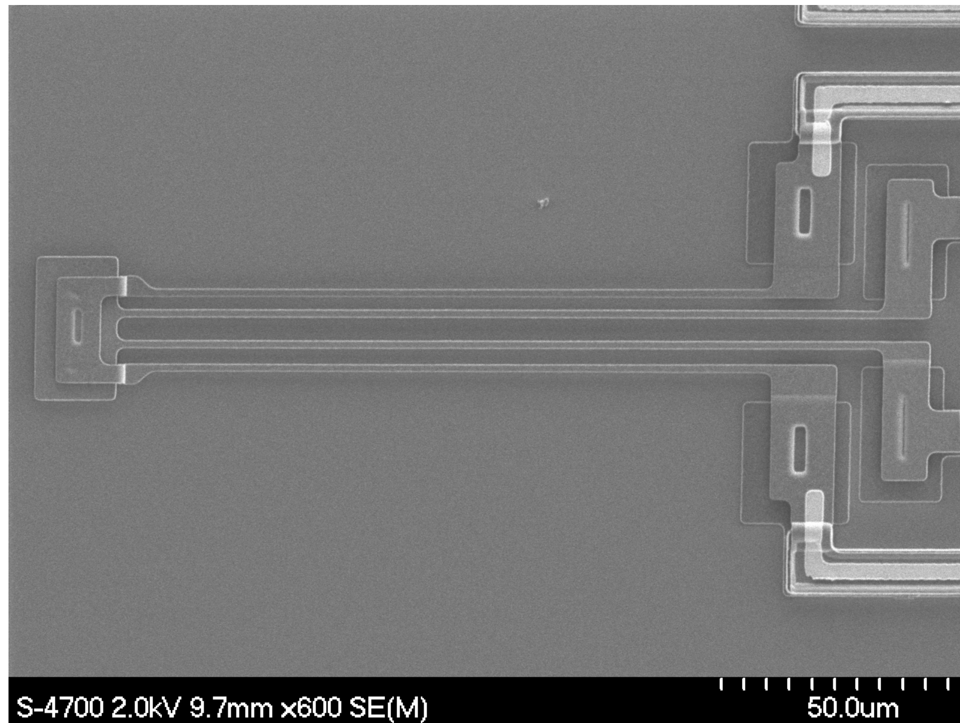

Figure 25: SEM Image of Constructed 2DTA

The following three camera image of Figure 26 shows the 2DTA in three positions, the off position to the left, a 5 µm out-of-plane displacement in the center (note change in focus), and a 1.75 µm planar displacement in the far right image. The yellow indicates the TA edge in the off position, making it easier to distinguish the planar motion. Also notice no in-plane displacement for the center image.

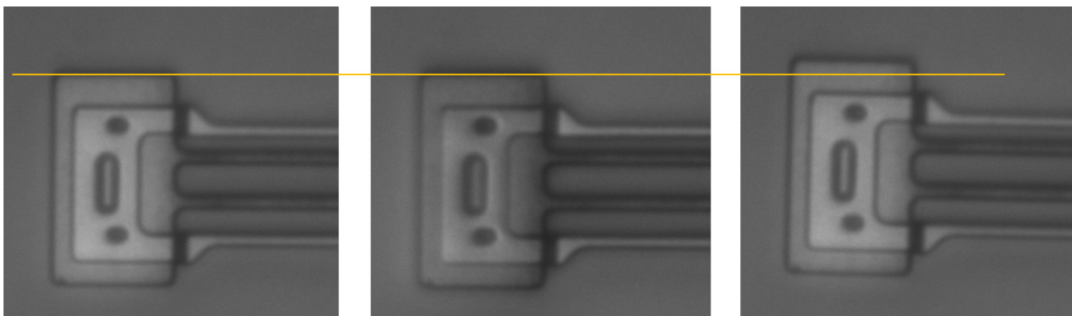

Figure 26: Actual 2DTA Displacement. From Left to Right, Off, Unfocused Maximum Z-Displacement (5 µm), and Maximum X-Displacment (1.75 µm)

Chapter 3: Finite Element Analysis

3.1: **Model**

Full featured 3D geometric models of the 2DTA were created in COMSOL Multiphysics® 4.0a in order to have a better understanding of the actuator before actual testing. The advantage of using COMSOL over other FEA simulation software is its ability to easily merge many physical domains together in one model.

The 2DTA tested had 175 μm and 150 μm long Poly1 and Poly2 arms respectively. The distance between the Poly2 and Poly1 arm was 3 μm. The Poly1 gap distance was 5 μm

3.1.1: **Importing the 2DTA Model**

Instead of modeling the TA in the COMSOL program itself, an external CAD program was used. Solid Edge V20 was used to model all three layers separately then combine them in an assembly. This assembly could then be exported in the Seimens Parasolid format (.x_b) which interfaces with the COMSOL 'Cad Import Model'. Solid Edge provides a much more intuitive GUI than COMSOL for modeling complex geometries.

3.1.2: **Domains Modeled**

With the 2DTA geometry modeled and imported within COMSOL, the boundary conditions and constraints must now be applied. In order to have a complete model with an input parameter of voltage potential and output of displacement, three subdomains must be modeled. These include 'Joule Heating', 'Thermal Expansion', and 'Stress

Strain'. In the latest versions of COMSOL, one physics setting already encompasses all three subdomains. This means the user does not have to manually set the crossover variables.

The following three headings describe in depth each subdomain and their respective settings.

3.1.3: **Stress-Strain Subdomain**

The Stress-Strain domain is the easiest to set as few boundary conditions must be applied. The default boundary condition for every surface is 'free', meaning they are not constraint in any direction or rotation. For the 2DTA, the four Poly1 pads must be fully fixed. Also the initial conditions for velocity and acceleration are set to 0 by default.

3.1.4: **Thermal Domain Subdomain**

Heat Transfer at the micro scale is dominated by conduction to both the substrate and through the arms to their anchor points. It is modeled as a combination of 2D and 3D heat transfers. The conduction along the arms is a full 3D model, in which heat can flow from element to element in all directions. Heat flow to the substrate is only modeled on the geometry surfaces with no elements representing the surrounding air.

The COMSOL Boundary setting for heat flux to the substrate follows the equation $q_o = h * (T_{ext} - T)$ where q_o is the external heat flow, the heat transfer coefficient (h), T_{ext} being the surrounding temperature (298.15 K) and T is the temperature (K) of the element from the previous iteration. The conduction coefficient (h) to the substrate is approximated by $h = k_{air}/\Delta z$ (Hickey [15]), where k_{air} is the Thermal conductivity of air (0.03 W/mK) and Δz is the height from the substrate to the center of the arm in

question (3 μm for Poly1, 3.5 μm for Poly2). Hickey only modeled in-plane actuators where Δz remained constant, but with a VTA this height is constantly changing. Therefore an expression must be entered for the heat flow from the arms, $h_{poly1} = k_{air}/(0.000003 + w)$ where 'w' the element Z-displacement for the previous iteration. The T_{ext} used for these cases was 298.15 K

A MEMS thermal actuator also loses heat to the substrate by conduction along the arm then down through the anchors. A fixed temperature boundary condition was imposed on the four Poly0 pads of 298.15 K, similar to the external temperature of the arm heat flux.

3.1.5: **Joule Heating Subdomain**

The default setting for the joule heating subdomain is a model with electrical insulation along all boundaries. This is the appropriate setting for all surfaces except the four voltage application points. An 'Electric Potential' boundary setting was chosen with a global variable as the input. This allow for easier changing of all four voltage from the 'parameters' tab.

The electrical conductivity of the polysilicon is not listed in the pre-defined material library and must be added. The nominal room temperature sheet resistivity (Rs) of all three polysilicon layers as stated in the PolyMUMPs Handbook [7] have units of Ω/sq. The conductivity can be calculated by dividing R_s by the layer thickness (t) as seen in (4).

$$\sigma_o = \frac{1}{R_s * t} \quad \textbf{(4)}$$

Discrete currents were applied to the bottom of all four Poly0 Pads as seen in the three dimensional (3D) isometric view of Figure 27.

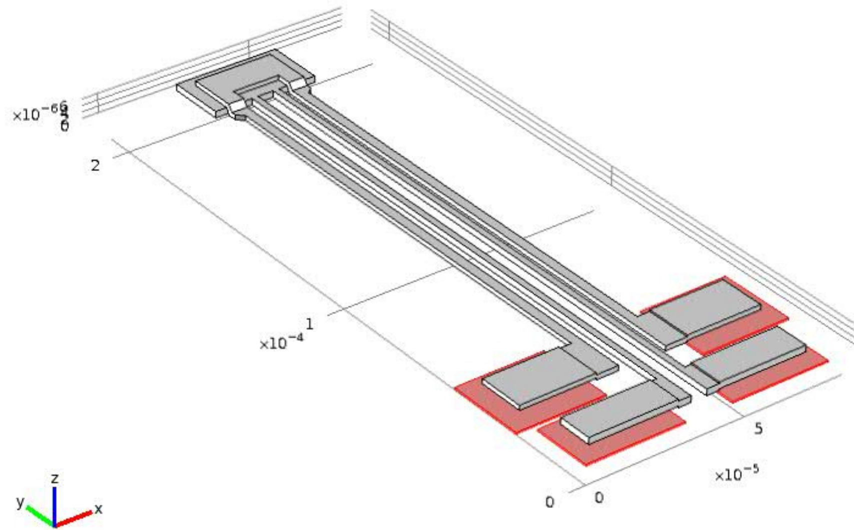

Figure 27: 2DTA COMSOL Model with Highlighted Poly0 Pads

3.1.6: **Model Physical Properties**

Table 3 shown below list the physical properties used in the FEA model, most are defined in Comsol's MEMS module with the exception of the electrical conductivity. Initial values used for σ_o were calculated using (4) and determined to be 50 000 and 33 333 S/m for both Poly1 and Poly2 respectively [7].

Table 3: FEA Polysilicon Properties

Property	Variable	Expression	Units
Coefficient of Thermal Expansion	α	2.6e-6	1/K
Heat Capacity	Cp	860	J/(kg*K)
Relative permittivity	ε	4.5	
Density	ρ	2320	Kg/m^3
Thermal Conductivity of polysilicon	k_{poly}	50	W/(m*K)
Thermal Conductivity of air	k_{air}	0.03	W/(m*K)
Electrical Conductivity [7] [30]	σ	$\sigma_o/(1+8.3e\text{-}4*(T-T_o))$	S/m
Young's Modulus	E	160e9	Pa
Poisson's Ratio	ν	0.22	

After comparing in-plane displacement at a given current with experimental results, it was determined that the actuator's Poly2 layer resistivity is much higher than the nominal resistivity. To calculate the new resistance, a current 2.2 mA (9.9 V) was passed through the actuators using the wires. Since the wires have an unknown resistance, two probes were positioned at the base of the actuator and recorded a voltage of 7.87 V. Using this voltage measurement and the known current, a new conductivity was calculated at 18637 S/m (compared to the 33 333 S/m nominal value). To ensure the contact resistance of the probes did not negatively affect the measurement, it was measured by touching both probes to a metal bonding pad. A resistance of approximately 100 Ω was negligible compared to the actuator resistance of 3577 Ω.

3.1.7: **Convergence Study**

For ease of meshing, tetrahedral elements were used. The Comsol software has by default 9 size settings ranging from 'Extremely Coarse' to 'extremely fine'. To ensure validity of the FEA results, a convergence was performed using preset tetrahedral element sizes.

Table 4 summarizes the convergence study results. Element sizes were compared using the resulting displacements and computational time.

Table 4: Comsol Convergence Study Results

Comsol Size Setting	Elements	Displacement Results (µm)	Computational Time (s)
Extremely Coarse	3640	9.087	68
Coarser	6047	9.062	76
Coarse	9678	8.913	90
Normal	15141	8.806	115
Fine	21066	8.780	165
Finer	30456	8.737	225
Extra Fine	44913	8.705	335
Extremely Fine	67343	8.675	515

Simulations were run with as low as 3640 elements and as high as 67343 elements but the resulting displacement only varied by 4.75% while the simulation time increased by 657%. Figure 28 plots the displacement versus the number of elements. A model with the 'Normal' element size setting or more will produce results within 1.51% of the 'Extremely fine' setting. This accuracy is higher than the anticipated accuracy of the FEA

analysis itself. The ‘Fine’ setting was used for all subsequent testing and results because of the combination of accurate results and it takes only 165s to complete the calculation.

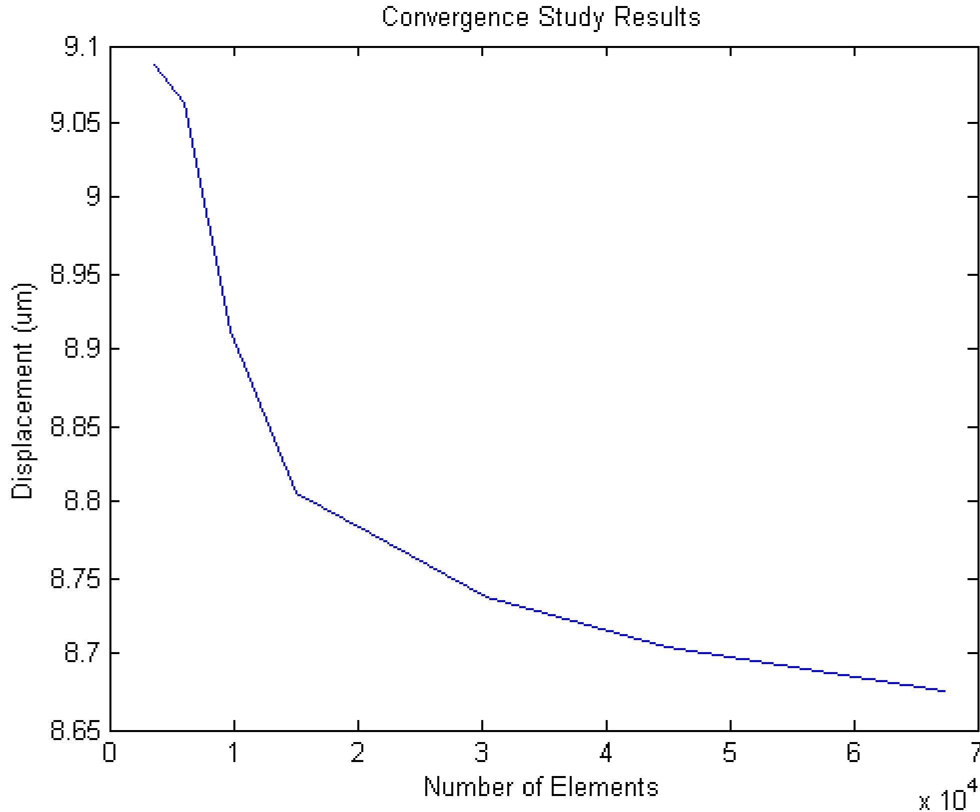

Figure 28: Convergence Study. Displacement Results versus Number of Elements

3.2: **Displacement Results in Common Stepping Positions**

A planned use for the 2DTA would be in a simplified lift and slide shuttle. In order to complete an actuation cycle, the actuator must move to a minimum of four locations. It must be able to lift the shuttle off its resting pads, while in the lifted position up it should move in-plane, and finally lower the shuttle once again on the resting pads but this time slightly ahead from its starting location. The fourth step brings the actuator once again to its starting location. Figure 29 shows all four steps of a lift and slide cycle.

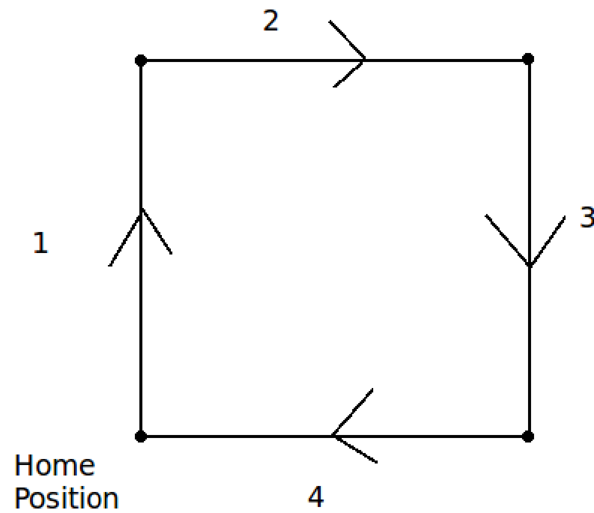

Figure 29: Four Step Lift and Slide Actuation Cycle (side view in the ZX plane)

3.2.1: **Maximum Z Lift Position**

For maximum lift, only the Poly1 should be heated as discussed in Chapter 2. For an approximate maximum temperature of 1000 K, a maximum current of 2.85 mA could be applied. The resulting temperature was 981.7 K (Figure 33) which produced an out-of-plane displacement of 4.91 μm (Figure 30). Table 5 summarize both the electrical setup along with the resulting displacements for the settings. The negative currents represent a current flowing in the negative Y direction.

Table 5: FEA Maximum Z Lift Electrical Settings and Displacement

<table>
<tr><th>Arm</th><th>Arm Current (mA)</th><th>X</th><th>Y</th><th>Z</th></tr>
<tr><td>P1_right</td><td>2.85</td><td rowspan="4">0.10</td><td rowspan="4">0.25</td><td rowspan="4">4.91</td></tr>
<tr><td>P1_left</td><td>-2.85</td></tr>
<tr><td>P2_right</td><td>0.00</td></tr>
<tr><td>P2_left</td><td>0.00</td></tr>
</table>

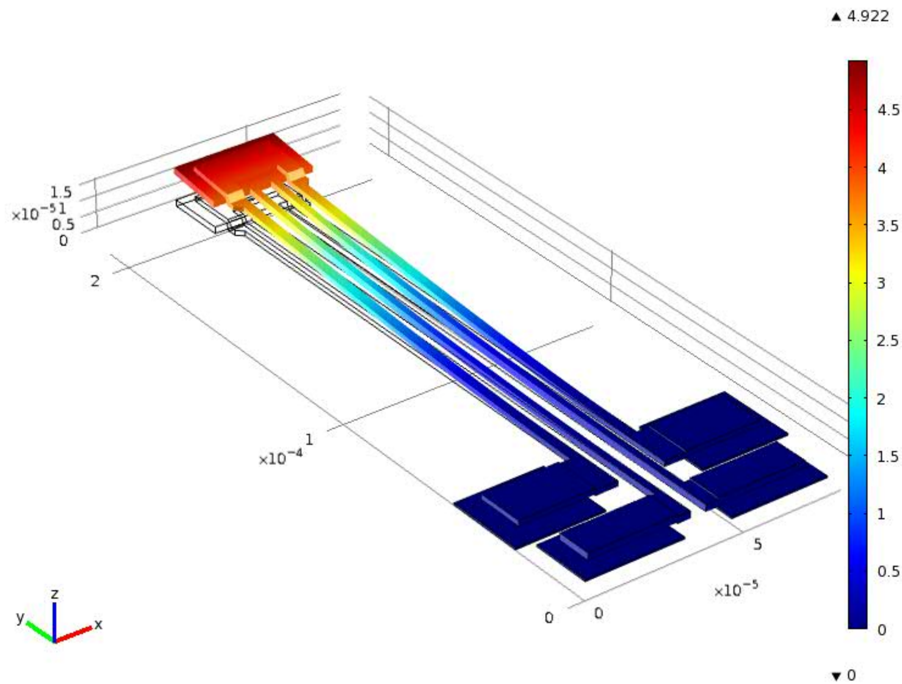

Figure 30: FEA Maximum Z-Displacement (µm)

Figure 31 shows the extracted height of the actuator for all elements along its Poly1 arm up to the TA tip. The TA tip is represented to the right of the plot with the anchors to the left. It shows that most of the flexing occurs at the beginning of the arm

with the end of the arm being rather straight. The displacement is exaggerated by a factor of 40.

A view of XZ plane looking towards the anchors is shown in Figure 32. The two black rectangles represent the edge outline of the TA in its off position. It provides a better view of the actual displacement of interest.

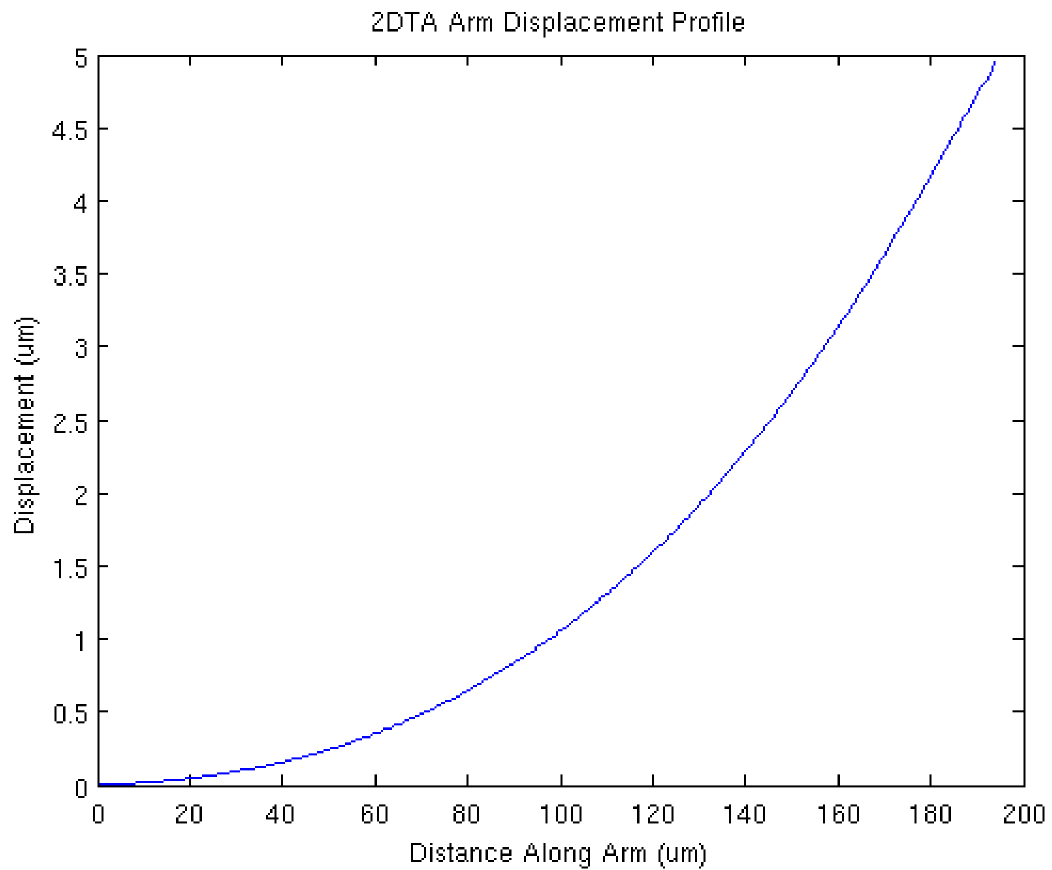

Figure 31: FEA 2DTA Displacement Profile along a Poly1 Arm

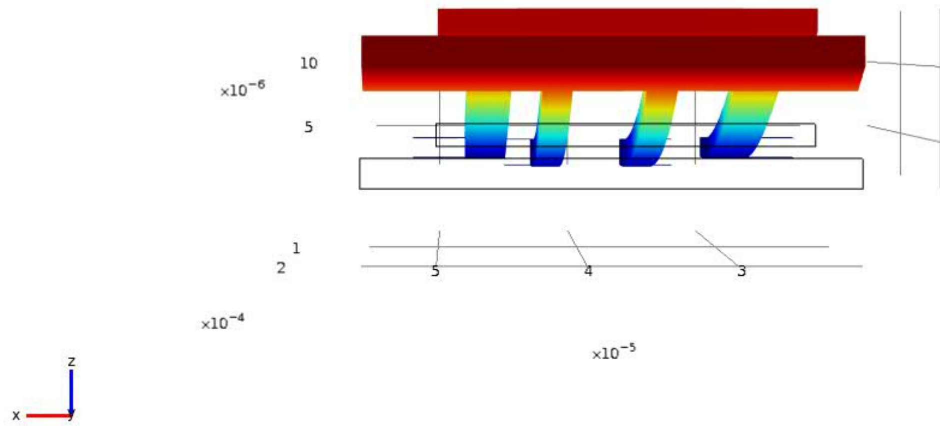

Figure 32: FEA Maximum Z- Displacement End View (XZ Plane)

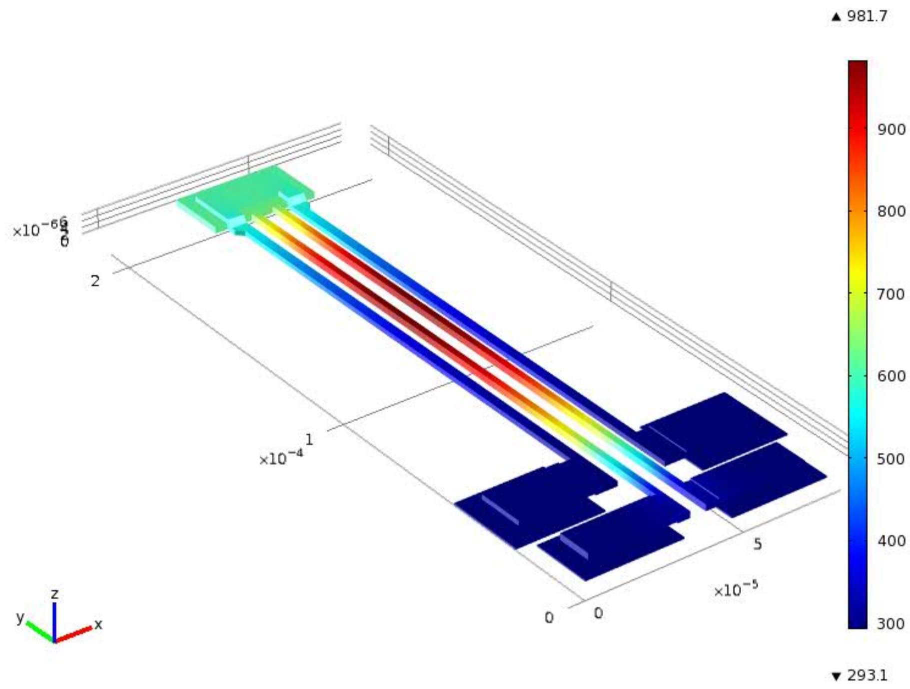

Figure 33: FEA Maximum Z-displacement Arm Temperature (K)

The induced current flow can also be seen in Figure 34. The same current density magnitude is found in both Poly1 arms but the direction is different resulting in two differently coloured arms. Also the maximum and minimum values labelled in the legend do not represent the average current density through the arm but the current density at the peak concentration points.

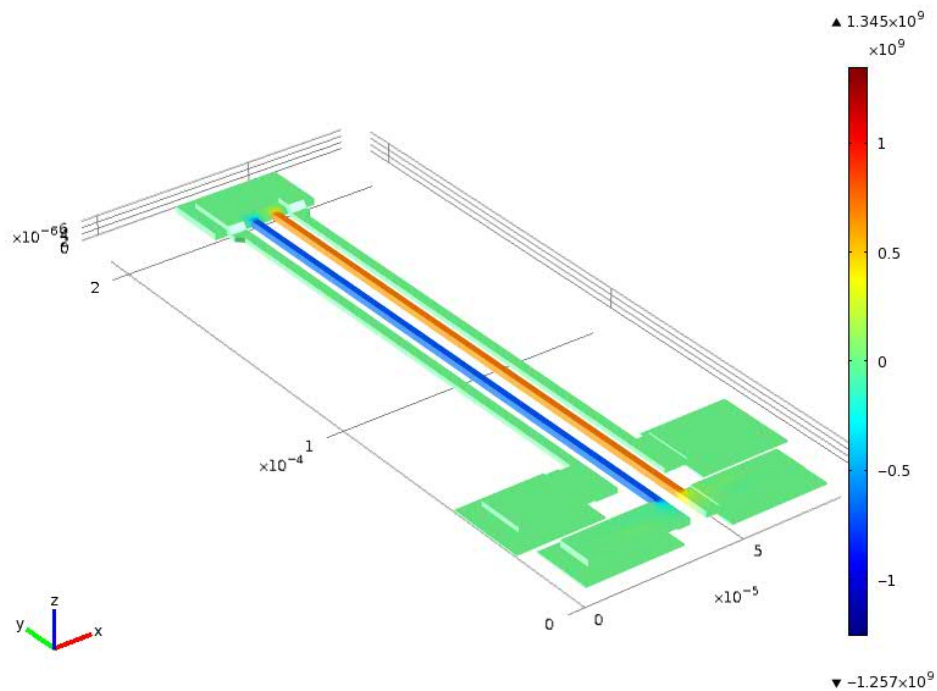

Figure 34: FEA Maximum Z- displacement Arm Current Flow (A/m^2)

3.2.2: **Maximum X-Displacement**

To produce a pure X-displacement, three of the four arms must be powered. When only the two side arms (P1_left and P2_left), the resulting displacement also has a significant downwards component. Partially heating the P1_right arm causes the tip to lift

producing pure X-displacement. This increased current also flows through the P1_left arms allowing further expansion.

Table 6 summarizes the voltage applied along with the induced currents within the arms. The current through the Poly1 arm is higher than the previously mentioned maximum of 2.85 mA. Since the displacement is in-plane, the height dependant heat conduction to the substrate does not diminish, allowing higher currents.

The in-plane displacement is a function of the lateral gap distance between arms. For the 2DTA, the distance between both Poly1 arms is 5 µm with 2 µm between the Poly1 and Poly2 arms. When comparing this to the 0.5 µm vertical separation of the Poly1 and Poly2 layers, the in-plane displacement is expected to be much less. A maximum in-plane displacement was calculated at 1.12 µm (Table 6)

Table 6: FEA Maximum X Electrical Settings and Displacement

Arm	Arm Current (mA)	X	Y	Z
P1_right	0.6	1.12	0.29	0.01
P1_left	-2.8			
P2_right	0.00			
P2_left	2.2			

Figure 35 shows the 2DTA in a pure X-displacement. The maximum displacement is 1.12 µm at the very tip.

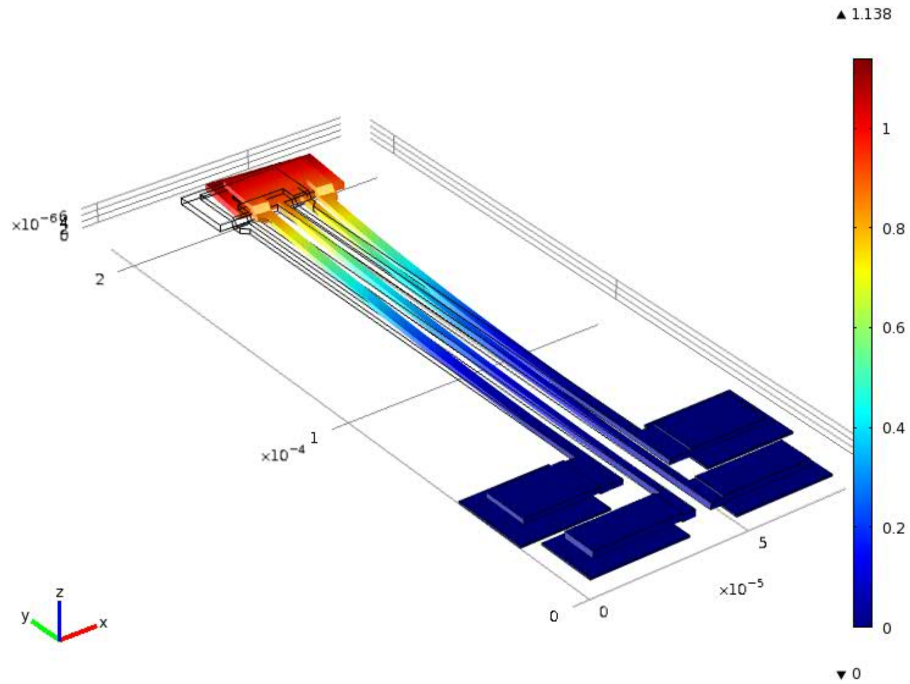

Figure 35: FEA Maximum X-displacement (μm)

Figure 36 shows the X-displacement from the tip XZ plane. The two black rectangles represent both the Poly1 and Poly 2 layers in the off position. You can notice the movement is not pure X, as a very small out-of-plane component can be seen. It is only approximately 1% of the in-plane displacement. With the 'perfect' P1_right voltage, no out-of-plane motion would be produced.

The temperature profile is shown in Figure 37. Even through 0.6 mA is applied to the right Poly1 arm, the temperature does not rise significantly. The goal of powering this arm is to provide slightly more current to the P1_left arm in order to counter the downward effect of a hotter Poly2 arm.

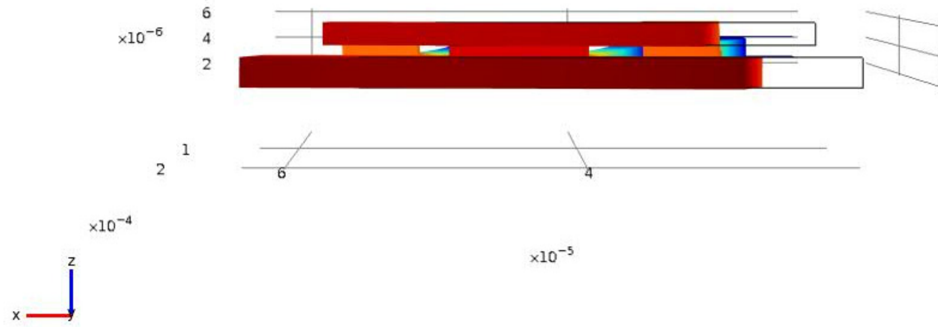

Figure 36: FEA Maximum X-Displacement End View (XZ Plane)

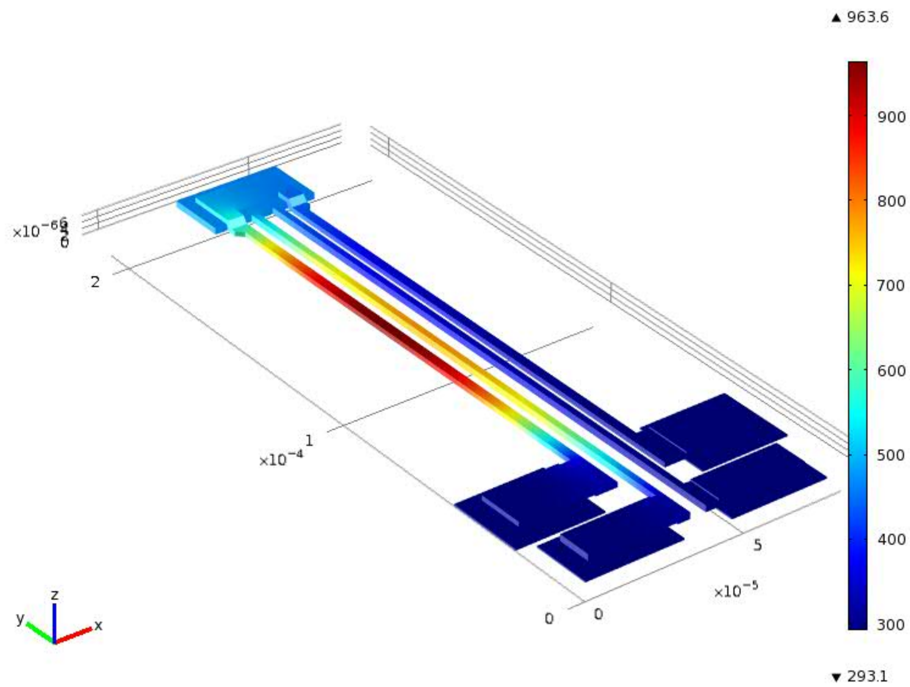

Figure 37: FEA Maximum X Arm Temperature (K)

The current flow shown in Figure 38 has a positive and negative direction relative to the Y axis. Most of the current flows through the two side arms as indicated in Figure 23. It is also worth noting the max and minimum values on the legend represent the value at the current density concentration points, not the average current through the arm.

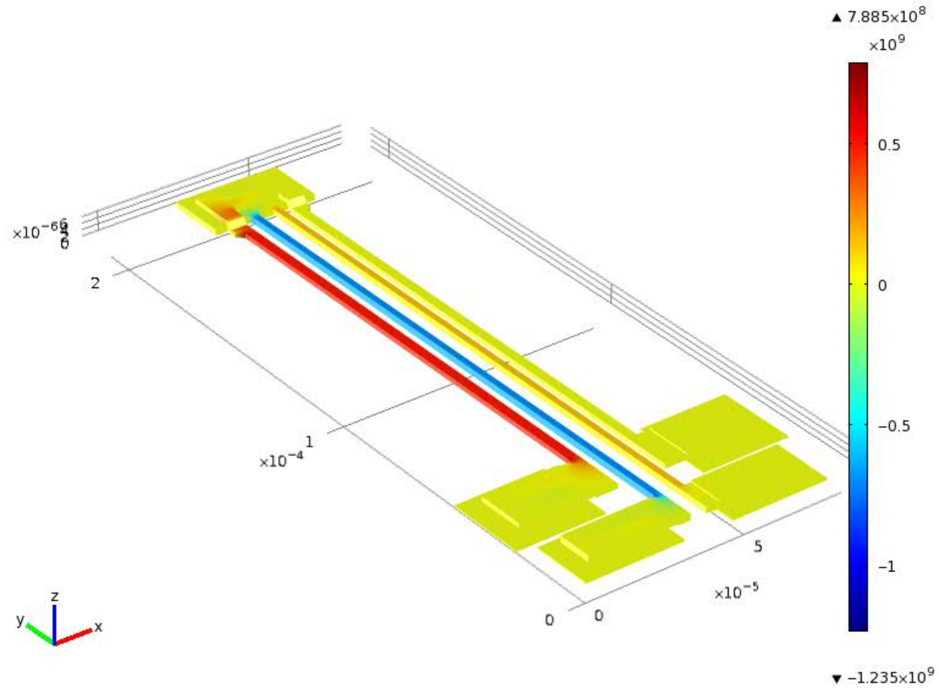

Figure 38: FEA Maximum X Arm Current Density (A/m^2)

3.2.3: **Combination X and Z Displacement**

To produce a complete step, an XZ combination displacement is needed. This is accomplished by increasing the P1_right voltage and decreasing the P2_left voltage from the pure X-displacement case. Both Poly1 arms and one Poly2 arm should be considerable heated to produce the XZ-displacement. Table 7 summarized the applied voltages necessary for the displacement. In the PolyMUMPs process it is possible to create a stationary pad 1 μm higher that the off position of the 2DTA. A significant lift above this pad is needed to ensure stiction does not glue the shuttle to the pad.

Thus the target displacement was roughly 2 µm while trying to maximize the X-displacement. While maintaining an out-of-plane displacement of 1.92 µm half the height, 0.76 µm was achieved.

Table 7: FEA XZ Combination Electrical Settings and Displacement

Arm	Arm Current (mA)	X	Y	Z
P1_right	1.35	0.76	0.27	1.92
P1_left	-3.00			
P2_right	0.00			
P2_left	1.65			

Figure 39 shows the same isometric view as the previous two sections. Because the in-plane component is small compared to the out-of-plane displacement, the figure looks very similar to Figure 30. Both displacement components can clearly be seen in Figure 40. Again, the two black rectangle represent the outline of the Poly1 and Poly2 two in their off position. With only a displacement of 0.76 µm, it does not seem to be sufficient for shuttle driving but the actuator can theoretically operate equally in both the positive and negative directions. A single step could thus produce 1.52 µm of motion.

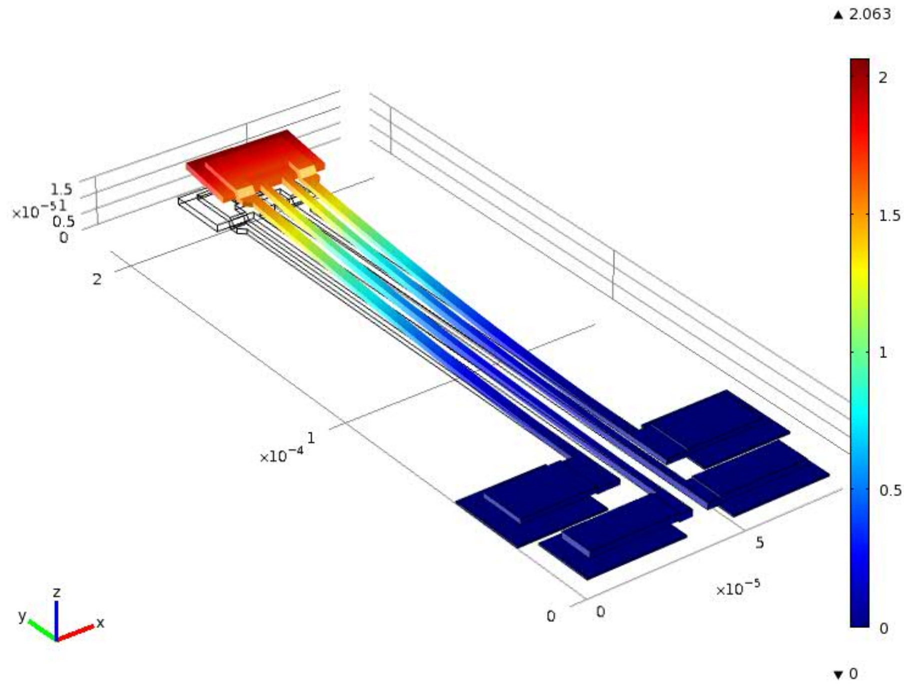

Figure 39: FEA XZ Combination Displacement (µm)

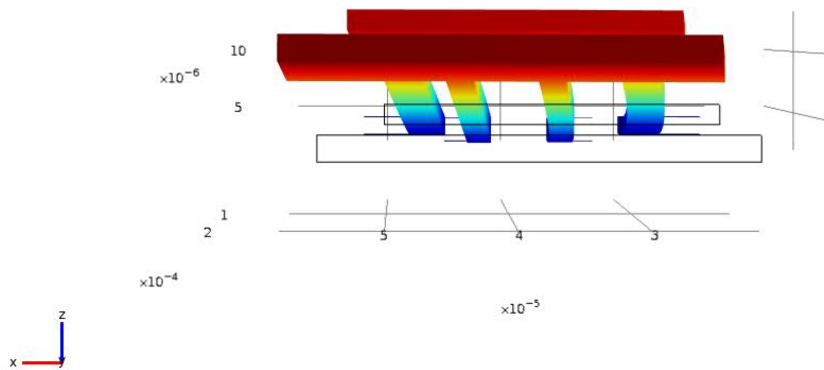

Figure 40: FEA Maximum XZ Combination Displacement (XZ Plane)

The temperature profiles are seen in Figure 41. Only one of the arms is heated to 944.5 K with the Poly2 arms reaching approximately 650 K and the P1_right arm at approximately 400 K. If the Poly2 arm does heat further, the out-of-plane displacement

diminishes with no additional planar motion as one of the other two arms will also heat up.

The current flowing through the arms is much more uniform than the two previous cases and more arms are heated. Figure 42 shows the FEA current density of throughout the 2DTA, one thing to notice is the zero point of the figure is not green as in Figure 34 and Figure 38 but a gold colour instead.

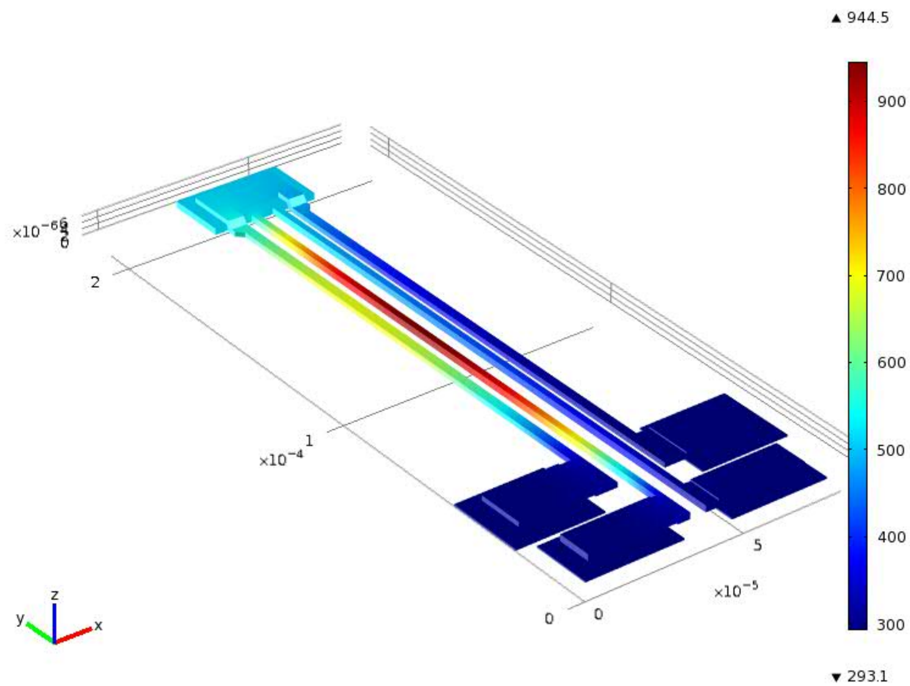

Figure 41: FEA XZ Combination Arm Temperature (K)

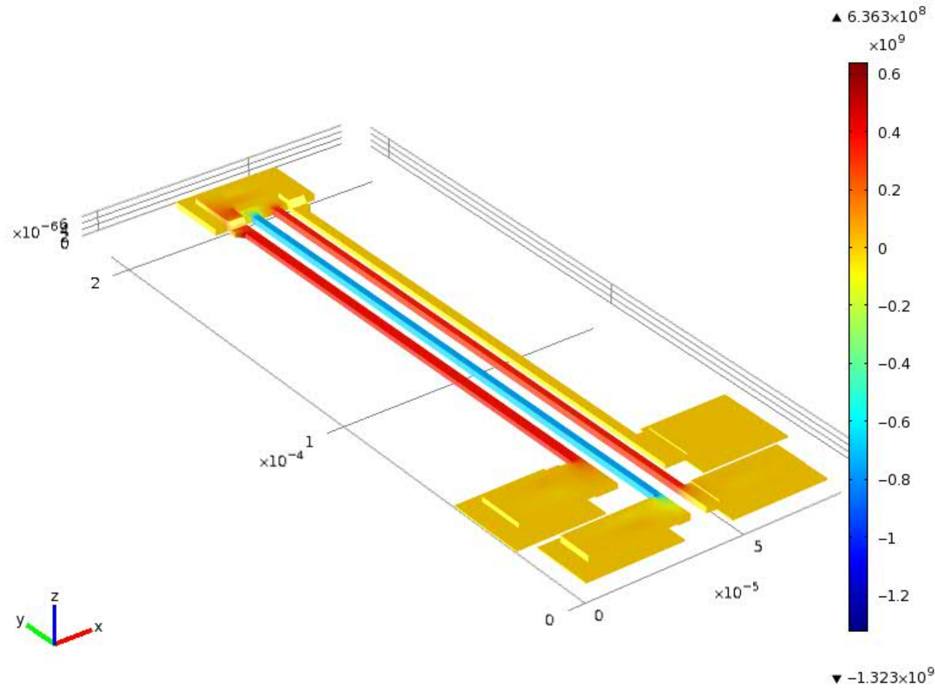

Figure 42: FEA XZ Combination Arm Current (A/m^2)

3.3: Maximum Displacement Range

The maximum displacement for the 2DTA is hard to define as it is possible to actuate it in many combinations of both X and Z position. An actuator was needed to accomplish a specific role and thus its maximum displacement in every direction is not as important as its ability to reach a select few.

3.3.1: Out-of-Plane Displacement versus Current

The easiest displacement to quantify is its out-of-plane displacement since its only dependant on one variable, the current through both Poly1 arms. To avoid inconsistencies in wiring resistance changes from chip to chip in the actual device, the tip displacement is plotted versus the current flowing through the arm. Figure 43 plots the displacement

versus current from 0 to 3mA. Remember the highest current achievable was 2.85 mA before a temperature of 1000 K was reached.

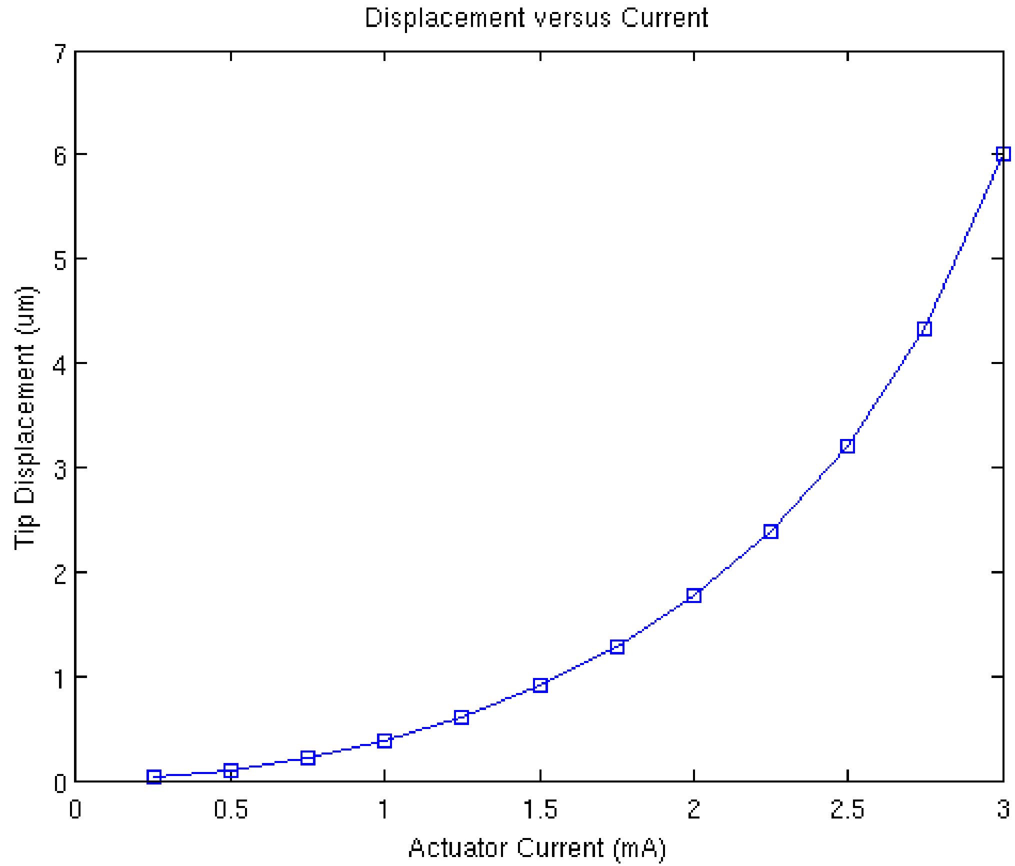

Figure 43: FEA Z-Displacement versus Poly1 Current

3.3.2: **Theoretical Displacement Envelope**

To determine what kind of range the 2DTA has, a FEA displacement envelope was constructed in which the actuator is capable of reaching every point within it. All points in the graph are displacement when one of the arms is heated to 1000 K. It is very useful to know the displacement of your envelope since you can then determine whether the specific actuator meets the displacement requirements for the job. E.g., if the four step sequence for the lift and slide cycle can fit within the envelope, it should be a suitable

actuator. Figure 44 shows the simulated displacement envelope for the 2DTA described above.

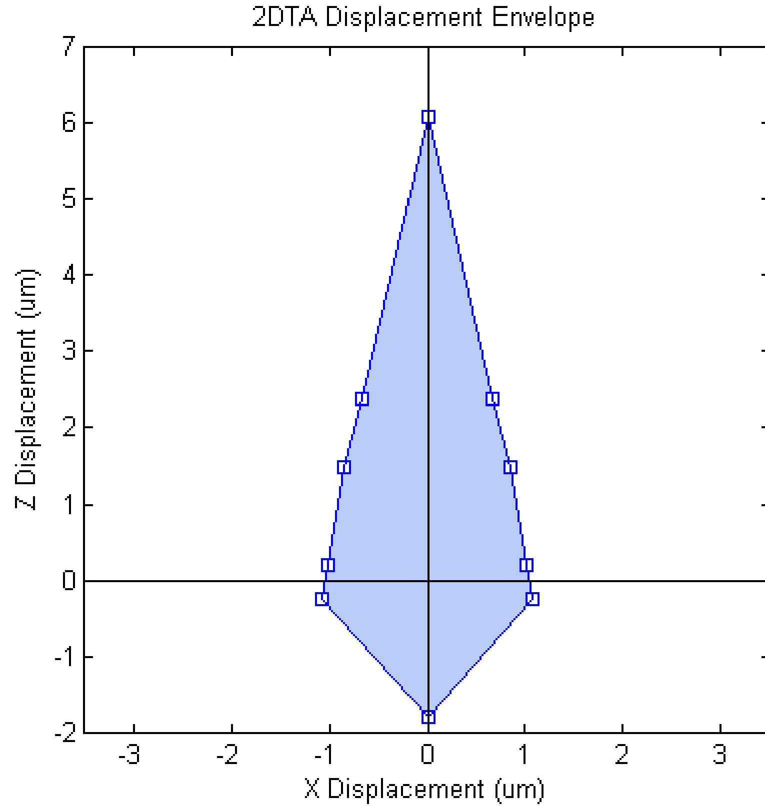

Figure 44: FEA 2DTA Displacement Envelope

Figure 44 provides a good idea of the anticipated in-plane and out-of-plane displacement but no information about the axial displacement cause by the rotation. The Y-displacement for the pure X-displacement is approximately 0.29 μm. This represents the maximum Y-displacement which is found in the tip corner in the opposite direction of the displacement, e.g. top left corner of the tip for a displacement to the right. This axial displacement is present in other existing TA designs.

3.4: **Effects of Changing Heat Transfer Coefficient as Out-of-Plane Displacement Increases**

As mentioned in section 3.1.4, heat conduction to the substrate varies as the actuator lifts out-of-plane. As the actuator is lifted out-of-plane the tip loses its ability to shed extra heat to the substrate. As a result, the temperature profile is skewed towards the tip. Figure 45 shows the significance of modeling this variable heat transfer. The blue line corresponds to the variable delta z heat transfer; the red for fixed delta z heat transfer. For a given voltage potential across the Poly1 arms; the maximum temperature is approximately 200 K higher. The red constant heat transfer line is also symmetric about the arm midpoint whereas the blue line has its maximum moved towards the tip, which also has a higher temperature. Modeling the heat transfer as variable is thus very important in VTAs.

Since the heat transfer diminishes as the actuator lifts, the efficiency of the actuator rises as less power is needed per displacement. The maximum temperature increases very quickly at the upper end of allowable current.

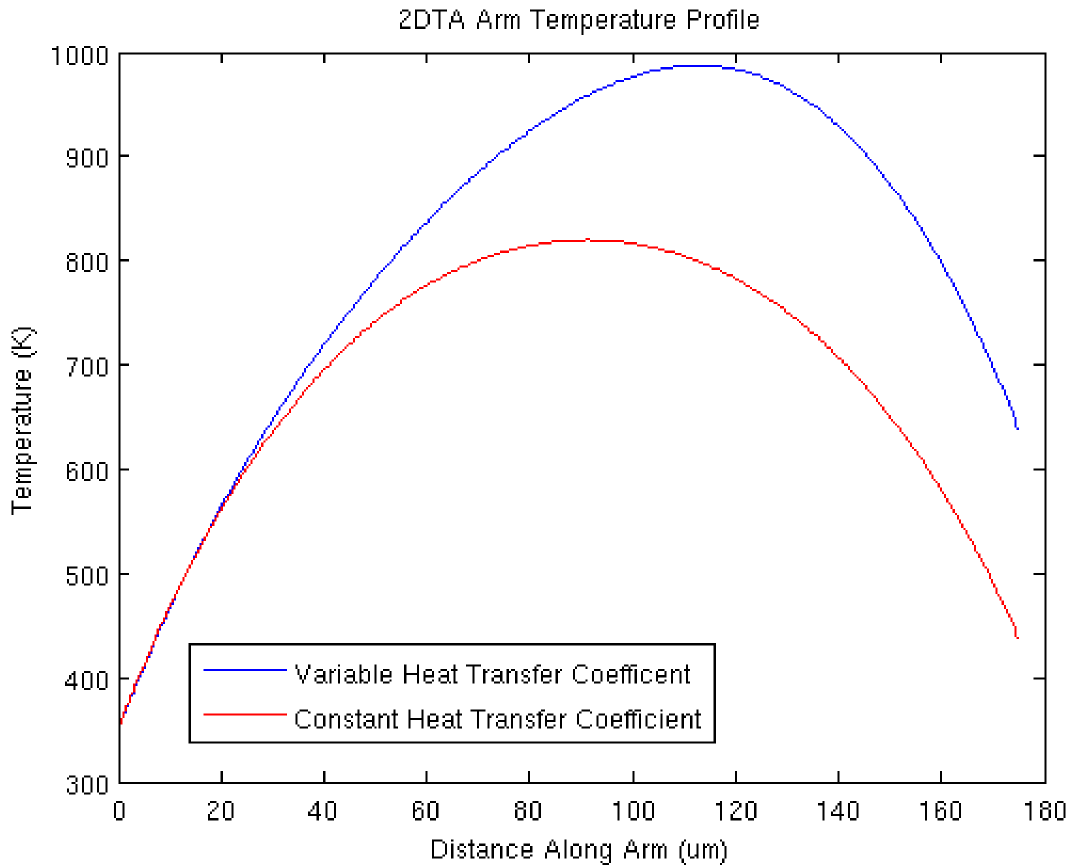

Figure 45: 2DTA Arm Temperature Profile With and Without Height Dependant Heat Conduction to the Substrate

3.5: Mechanical Natural Frequency

The natural frequency of the structure was also simulated, with the first four modes show below. For eigenfrequency calculation using COMSOL, the 'Joule Heating and Thermal Expansion' physics setting cannot be used, the 'Stress Strain' physics must be used instead. The same material properties as listed in Table 3 were used.

The first mode (Figure 46) occurs at 44 kHz and is purely out-of-plane. That result was expected around this range as similar natural frequencies were measured for in-plane actuators (Hickey[15]). The second mode (Figure 47) occurs at 131 kHz and is

in-plane. It is about 3 times higher than the reported STA natural frequency which I attribute to a much higher gap distance which stiffens the structure in the planar orientation. The last two modes are the second out-of-plane mode (Figure 48) at 362 kHz and the torsional mode (Figure 49) at 434 kHz.

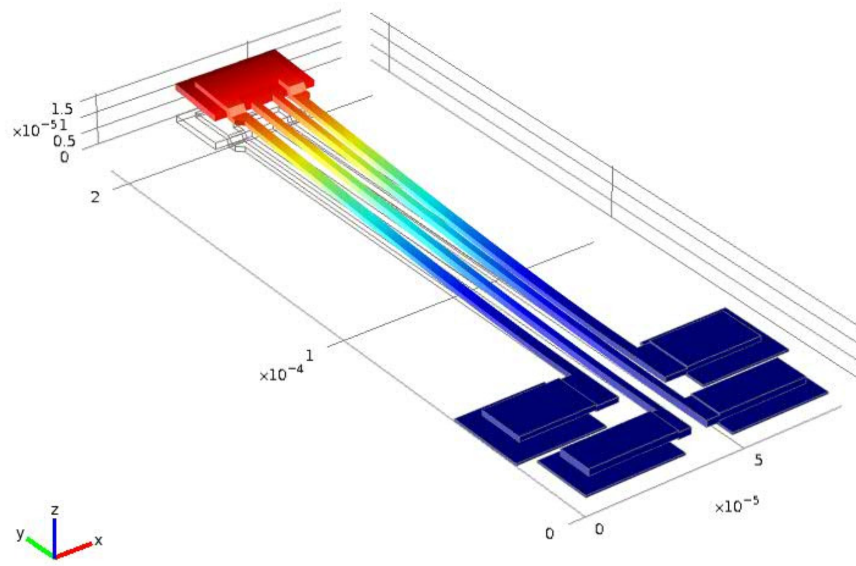

Figure 46: First Out-of-Plane Mode (44 kHz)

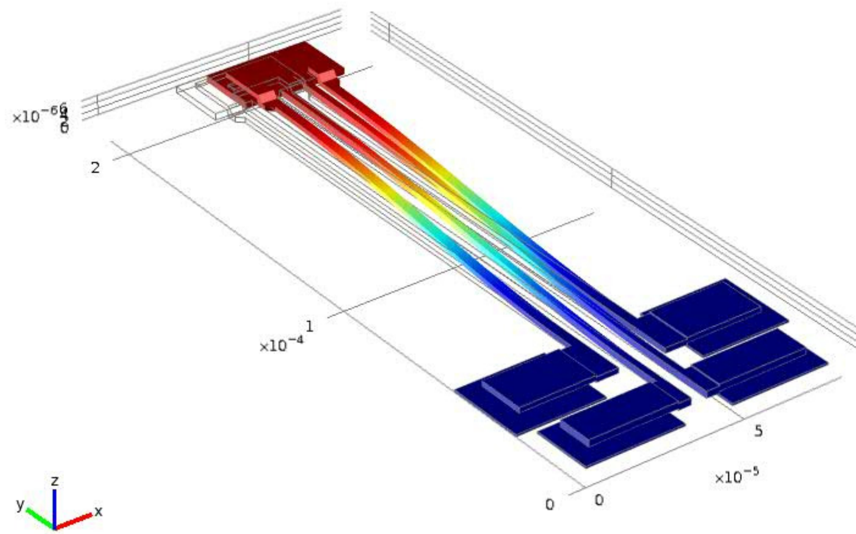

Figure 47: Planar Mode (131 kHz)

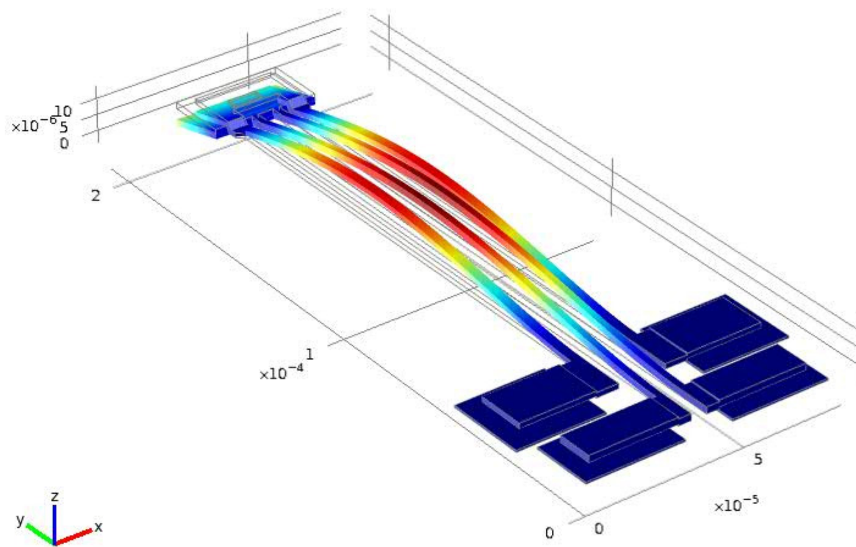

Figure 48: Second Out-of-Plane Mode (362 kHz)

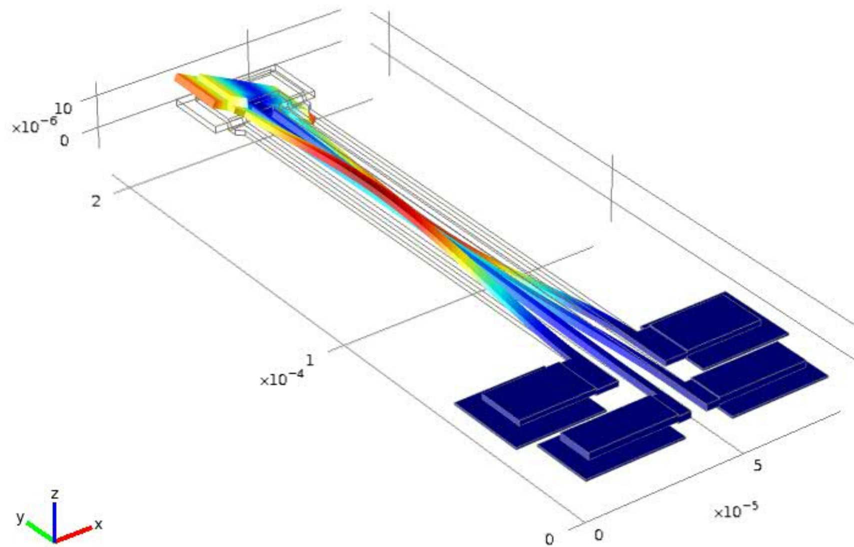

Figure 49: Torsional Mode (434 kHz)

3.6: Transient Heat Transfer Analysis

The limiting factor in operational speed for MEMS thermal actuators is the thermal time constant (τ). To estimate the time constant a transient analysis was performed using a constant height gap from the substrate to the actuator (Figure 50). A time constant of 170 μs was calculated, resulting in a cut-off frequency of approximately 1 kHz. The cut-off frequency (f_{3db}) is defined as the frequency in which the sinusoidal displacement is $\frac{1}{\sqrt{2}}$ of the full range displacement, roughly half power [11]. For a first order system: $f_{3db} = \frac{1}{2\pi\tau}$. We can see the thermal cut-off is much lower than the first mechanical mode at 44 kHz. With a constant height gap, the time constant represents the time required to heat of the arm irrelevant of the displacement. The actual device should

have a lower time constant since as the arm lifts, the heat dissipation drops. These values agree with the reported value of 160 μs by Hickey [11] for a STA.

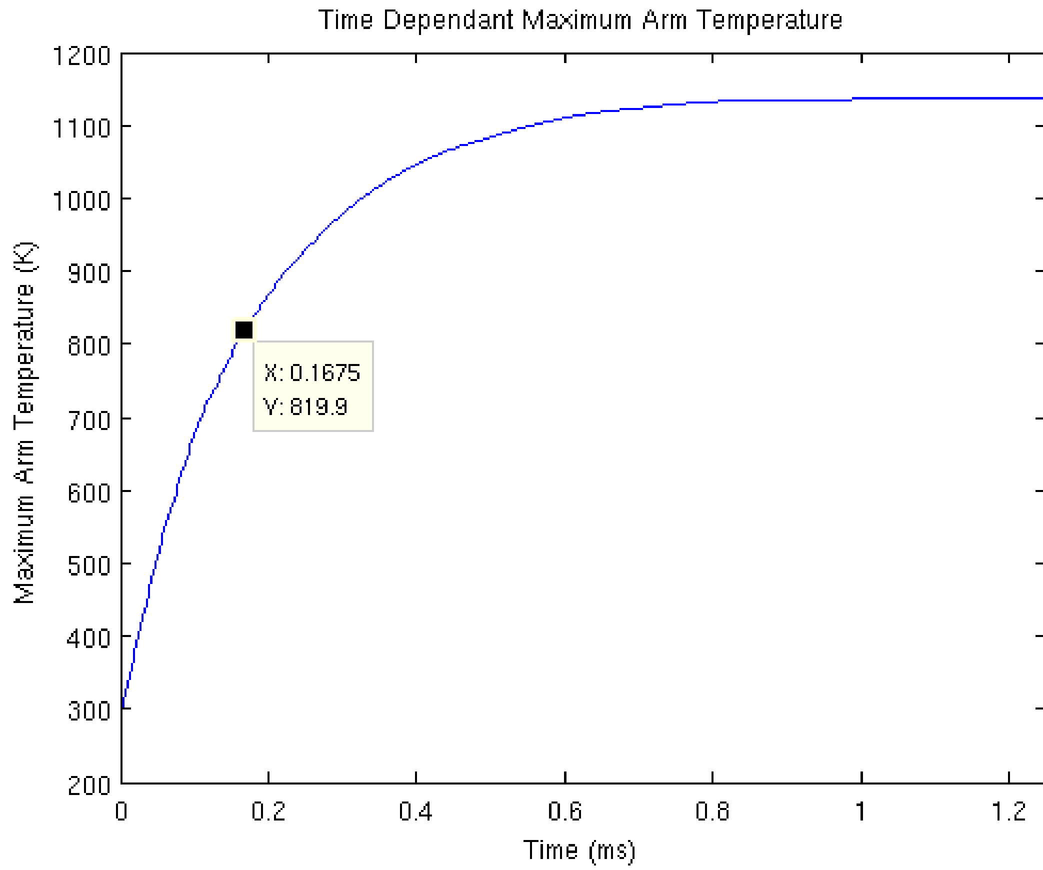

Figure 50: FEA Thermal Time Constant with Constant Heat Dissipation

Chapter 4: Hardware Setup

The MEMS chips fabricated by MEMSCAP are constructed off-site. Completed die are shipped to CMC for mounting. At Dalhousie, we prefer the die be mounted onto a 68 pin grid array (PGA). The 68PGA chip can then be inserted in a Zero Insertion Force (ZIF) socket for electrical connection with external circuitry. The ZIF can then be mounted to the Wentworth™ Probe station (Model 901). The probe station features an X-Y-θ stage for proper positioning of the chip under the optics. The microscope head is also mounted on a separated X-Y stage which must be used when probes are touching the chip.

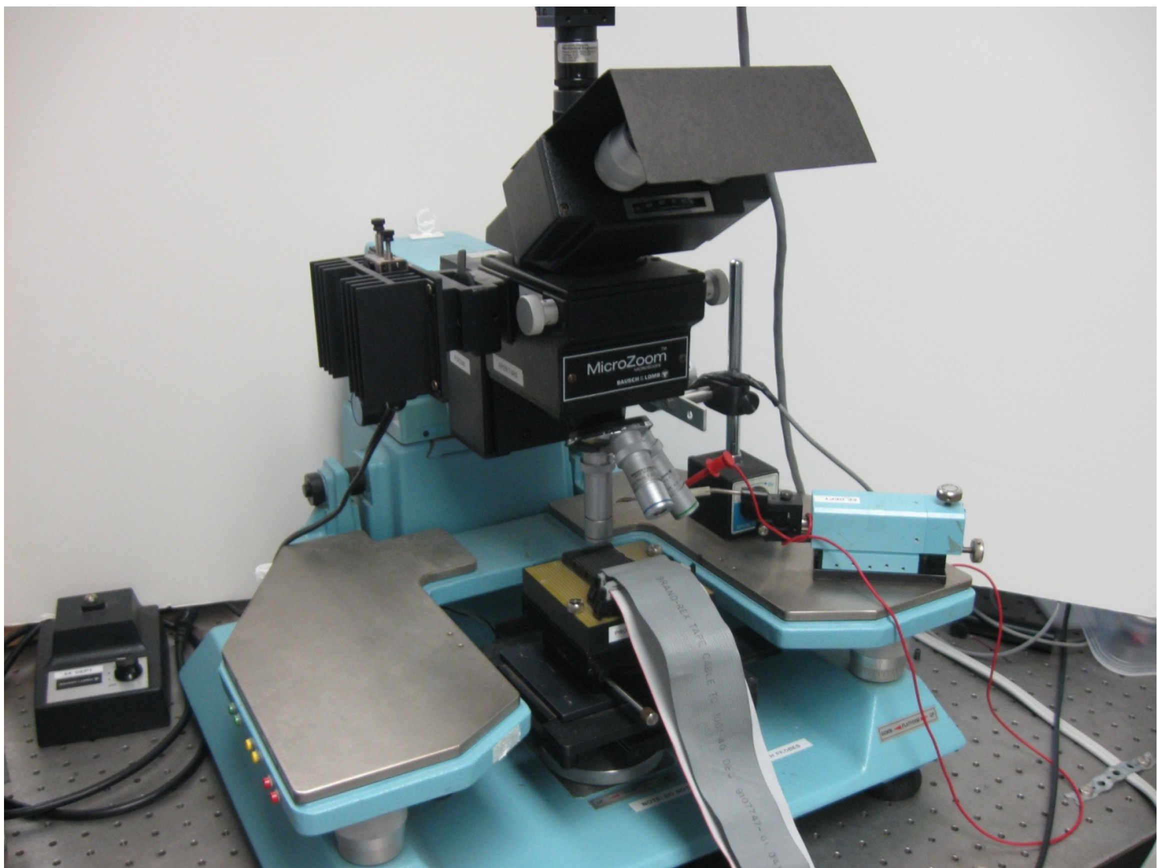

Figure 51: Microscope Setup with Probe and ZIF Holder

The chips arrive at Dalhousie with minimum work needed to begin testing. The exception is usually shuttles and plated which must be manipulated into the correct position. Thin tethers are attached to removable structure so they do not dislodge during the oxide release process. Wentworth (Model PRO195RH/PRO195LH) probes are used for breaking thee tethers and other physical manipulation of the devices on-chip. 0.30 mm diameter stainless steel acupuncture needs are used due to their fine tip (Figure 52). The thin tethers are very weak; a slight push from the side will break them.

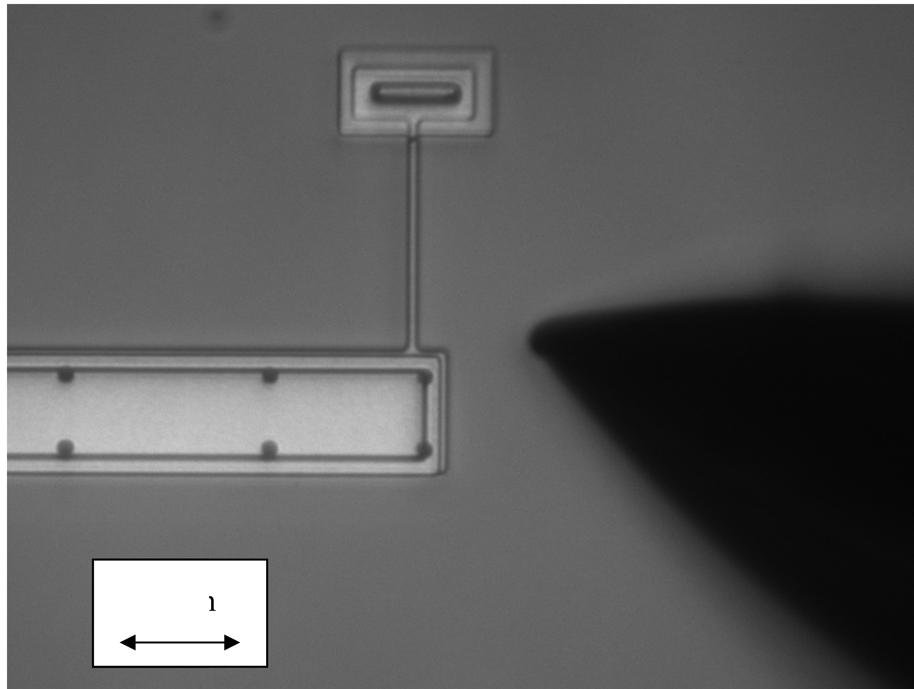

Figure 52: Probe Needle Ready to Break 2 µm Poly1 Tether

4.1: Electrical Setup

Once the chip is mounted to the ZIF it can be powered by external sources. A large box with 68 female banana plugs is used to transit power via a pair of ribbon cables (Figure 53). It allows a quick and easy method of connecting either power supplies,

switched, circuits or data acquisition cards to the MEMS device to individual pins on the chip.

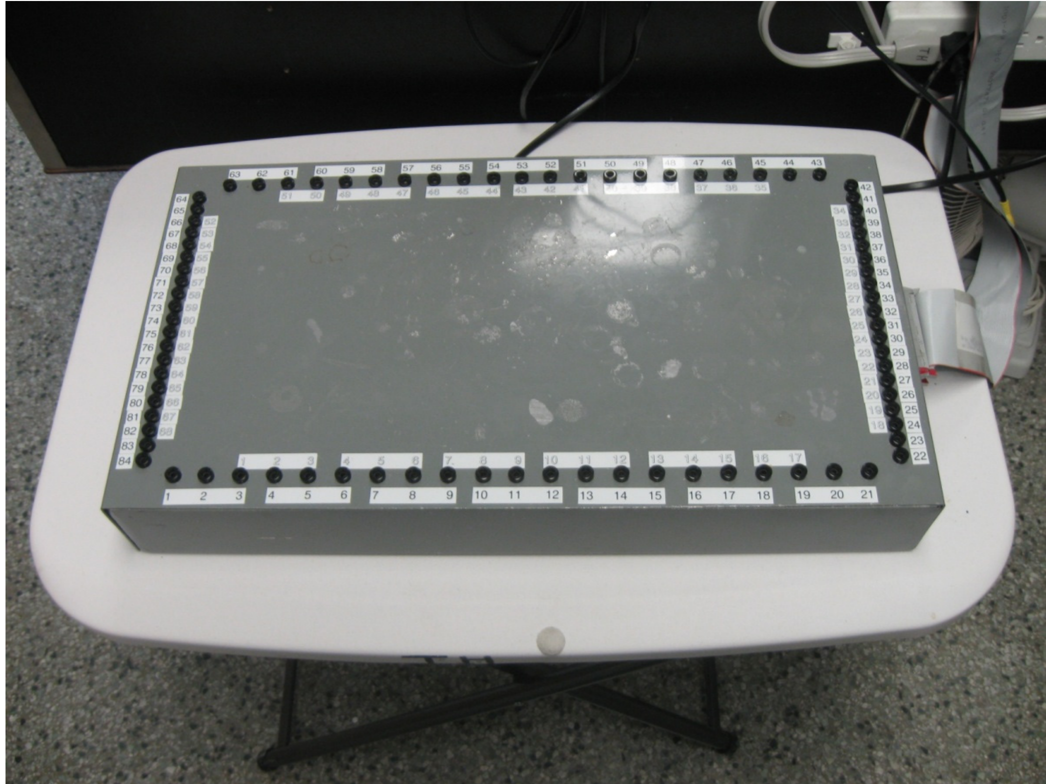

Figure 53: Wiring Box with Attached Ribbon Cable

4.1.1: **LabVIEW**

When complex signals or timed sequences are needed, National Instruments (NI) LabVIEW 2009 is used. LabVIEW is referred to as a graphical programming language aimed towards data acquisition and signal generation. NI calls programs created in LabVIEW as Virtual Instruments (VI) as they all have front panels and many interact with external signals. The NI DAQ card used was the PCIe-6323 which is capable of 4 analog outputs (±10 V range) and 48 digital I/O lines (NI [31]). The current limit is 5 mA, meaning they can power one 2DTA in any position. If the 2DTA is positioned in parallel, a current amplifier circuit is required.

One advantage of using LabVIEW is the easy creation of Graphical User Interfaces (GUI). As elements are added to the code, the corresponding objects are added to the GUI or Front Panel as LabVIEW calls it. Figure 54 demonstrate the front panel for control of the stepper motor. It features an assortment of buttons and switches to control the program in real time.

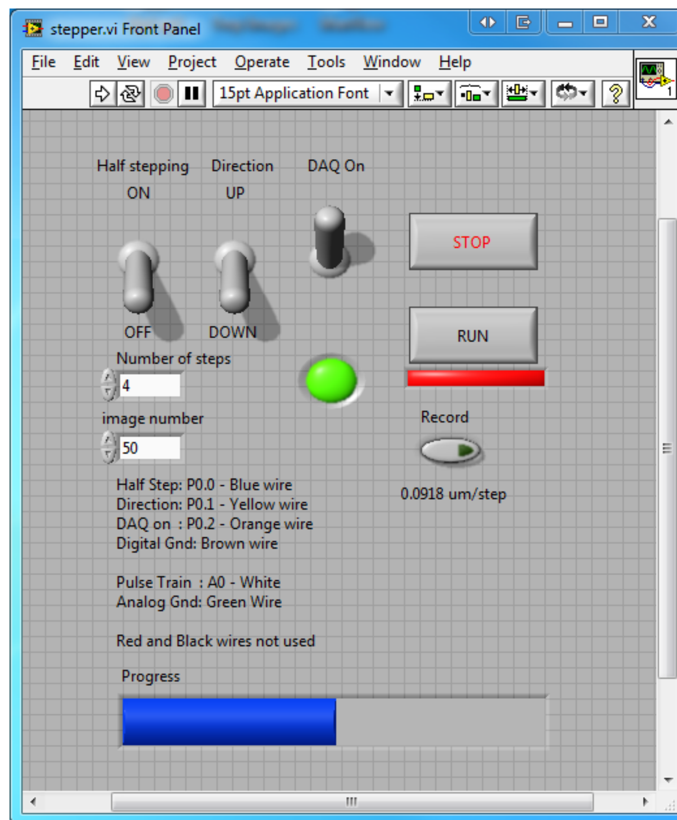

Figure 54: Stepper Motor Control LabVIEW Front Panel

Coding in LabVIEW is significantly different than text based languages. Each command or function is symbolized by blocks. Values are then passed between blocks via wires of different variable types. Figure 55 shows the code associated with the stepper motor front panel shown above (Figure 54)

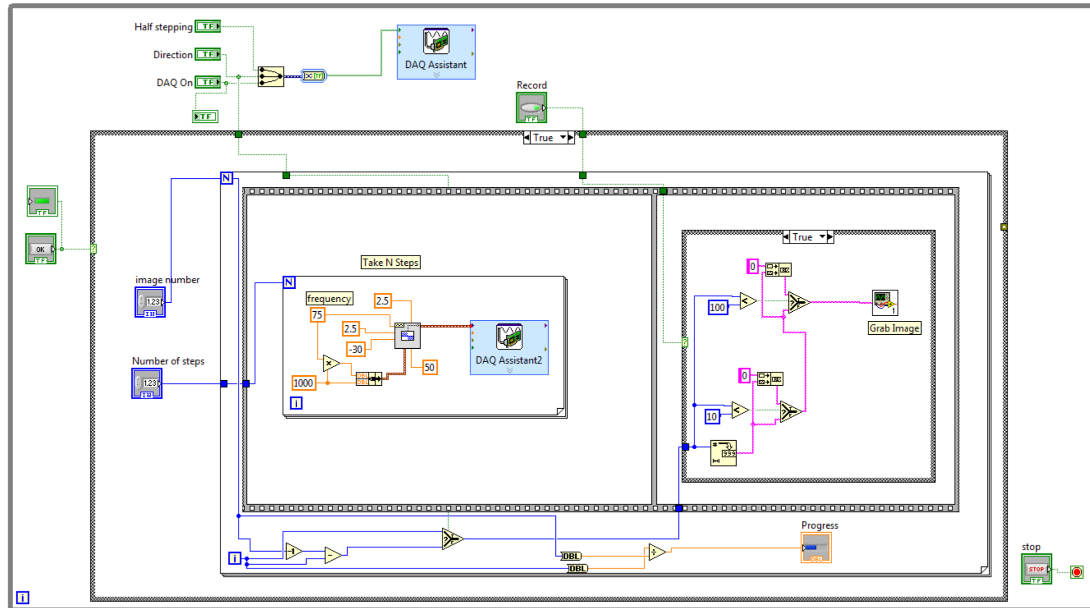

Figure 55: Stepper Motor Control LabVIEW Code

4.1.2: **Stepper Motor Control Hardware**

With the Wentworth microscope being manually controlled, a method to automate the focusing was needed. The height from focus technique requires a consistently small step size between focal planes. The technique was attempted by manually turning the fine focus knob in 1 μm increments but no reliable results could be extracted. Touching the sensitive microscope would move the image and the 1 um step size could not be consistently controlled. A geared down stepper motor was used in conjunction with a belt to attain these smaller step sizes. The belt connecting the fine focus knob to the stepper motor shaft can be seen in Figure 56. To determine the step size, the start position was noted, then the motor was turned 1000 steps and finally the end position was read. The resolution in full step mode was calculated at 0.0918 um/step, much finer than the 1 um/step attainable by hand.

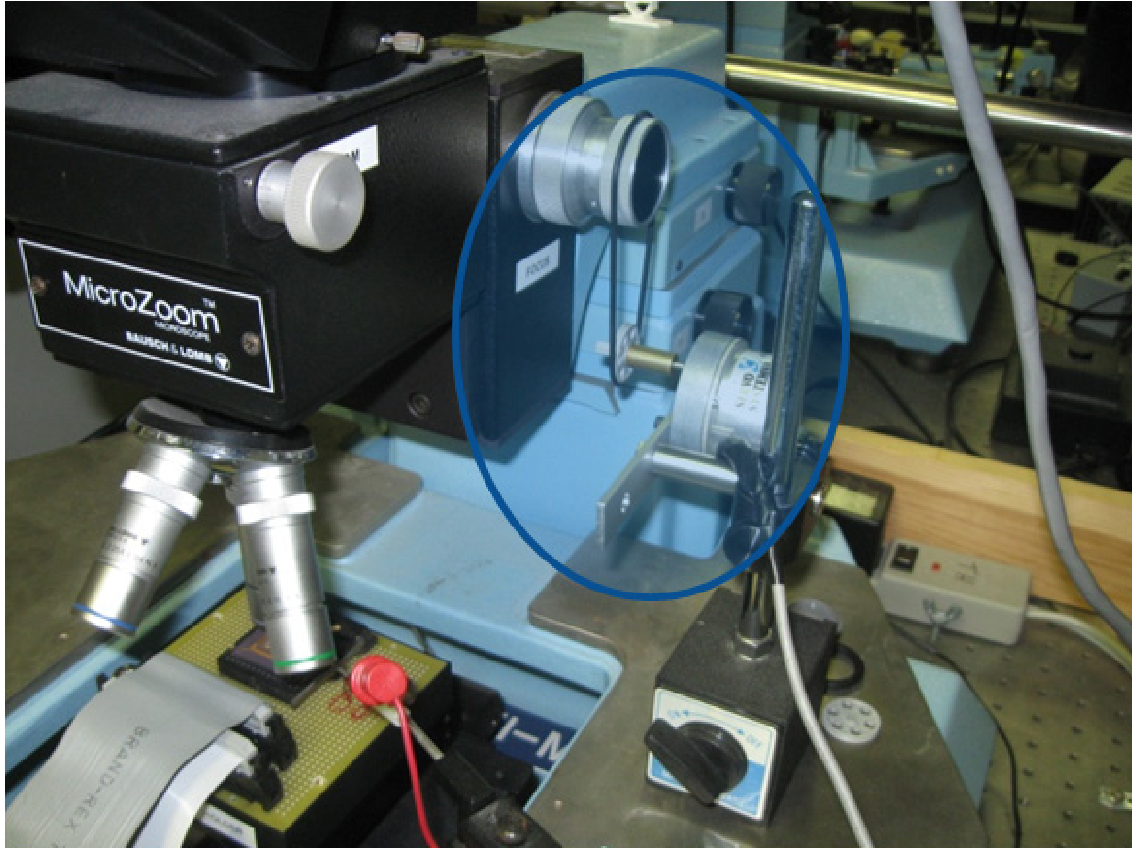

Figure 56: Microscope Setup with Attached Stepper Motor

To implement the height measurement technique by variable focal plane, many images must be taken. It is also very important to have consistent focal plane spacing between each image, taking 100+ images can be very time consuming if taken manually. The setup was assembled using LabVIEW, a stepper motor and an external controller. Even the camera is all controlled using a LabVIEW VI via a modified C++ program supplied by the camera manufacturer. A stepper motor cannot be controlled directly from a DAQ due to current limitations, so the Pololu 8-35 V, 2 A bipolar stepper motor driver was used, [32]. It is essentially a breakout board for the Allegro A4983 microstepping chip and contains an on board voltage regulator for the logic. A picture of the board can be seen in Figure 57.

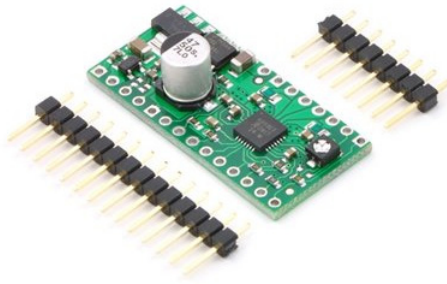

Figure 57: Allegro A4983 Stepper Motor Driver

A few signals must be supplied to the controller for proper operation. A 10V power supply is needed by the stepper motor. One pin controls the direction the motor will turn and one toggles the full / half stepping signal. The other microstepping inputs all have pulldown resistors making an external connection unnecessary unless finer microstepping is needed.

To produce motion of the stepper motor, a rising edge must be supplied to the 'step' input. A complete cycle requires 4 steps in full step mode, 8 for half stepping. These rising edges were produced by the LabVIEW VI of Figure 54 by the creation of a discrete length Pulse Width Train (PWT). The PWT length was controlled by the LabVIEW program and depended on how many steps were required between each image.

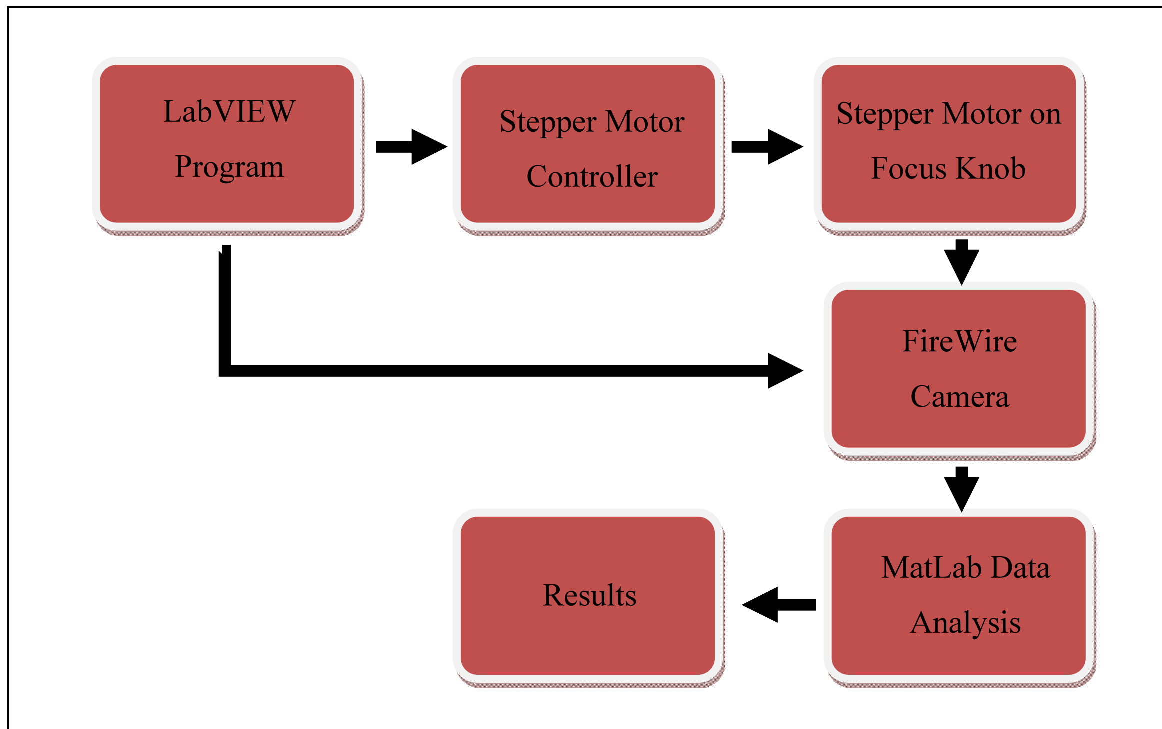

Figure 58: Out-of-plane Focus Measurement Flowchart

4.1.3: **Camera Setup**

Images were acquired using a Point Grey Research (PGR) camera model GRAS-14S3M. It used a ½" black and white 16 bit CCD sensor capable of 15 frames per second (fps) at a resolution of 1280x960. Connection to the computer was by FireWire cable to propriety PGR FireWire 1394-b PCI card. Even though the frame rate is slightly lower than the common 30 fps, the tests only require still images. No velocity testing was performed. Camera control was performed using the PGR FlyCap program provided by the manufacturer. The camera also comes with sample C++ programs for various tasks. As mentioned above, one such program was modified to take only one image the executable was run.

Chapter 5: Profiler Measurements

5.1: Experimental Setup

To measure the out-of-plane displacements of the 2DTA, a Nanovea interferometer was used. The profiler includes a moveable x-y stage along with a modular pen (see Figure 59). The setup also comes with two other pieces of equipment seen in Figure 60: he black box on the left controls the stage through BNC connection while the white box on the right processes the information from the pen and transits the data to the CPU.

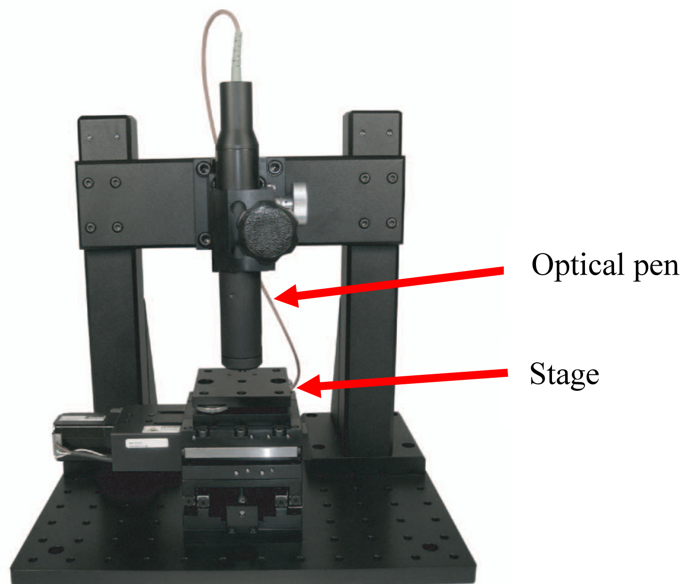

Figure 59: Nanovea Optical Profiler (Nanovea Documentation [33])

The stage model acquired by Dalhousie University was the (Nanovea Documentation [33]). It features an x-y stage with 50 mm of travel with a resolution of

0.1 μm (useful for X-displacement measurements). The total stage footprint is approximately 1x1 feet. The pens are modular and can easily be swapped.

Due to the small size of MEMS actuator, an optical pen with a vertical accuracy of 20 nm with a resolution of 5 nm was used. The smallest height separation between PolyMUMPs features is 500nm therefore the pen choice was adequate. The pen has a measurement range of 130 μm.

The Optical Profiler is a useful tool to measure out-of-plane displacements, but it can also be used to measure planar displacement as well. The resolution of X-displacement is limited to the 0.1 μm resolution of the x-y stage motion. Chapter 6 compares the X-displacement results with the common optical camera methods. The profiler does have some limitations though: it is expensive (~$50k); it is slow to use since it cannot take real-time measurements; to position the profiler's pen, area scans must be used which can take considerable time as iteratively smaller scans must be taken to home in on the device in question. This positioning usually takes approximately 15 minutes for a small feature.

Since the stage is the moving part, probes providing electrical contacts cannot be used under the Optical Profiler. Any device not properly wired by design cannot be actuated. Also, if a device gets stuck, one cannot flick it free. Instead one must remove the chip from the profiler and bring it back to the microscope for unstucking then restart the entire Optical Profiler process.

Figure 60: Nanovea Hardware (d'Entremont [34])

5.1.1: **Profiler Theory**

The Nanovea Optical Profiler operates on the principle of white light axial chromatism. The different wavelengths of light are focused at different heights (Figure 61) and depending on which wavelength is reflected and returned to the sensor, the surface height can be determined.

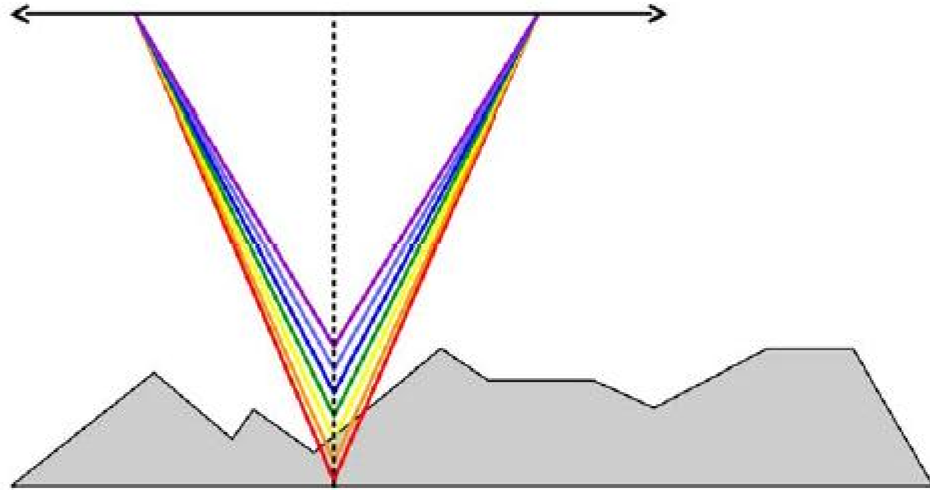

Figure 61: White Light Axial Chromatism (Nanovea Documentation [33])

The measurement range is the height difference between the highest focused wavelengths to the lowest. The returned light travels through the fibre optic cable and gets read by the sensor.

5.2: Area scans

The Optical Profiler can be used to generate 3D profiles of objects.

Area scans must also be used to position the optical pen directly above the device in order to perform the quicker profile scan. There are five settings associated with area scans; both the X any Y scan dimensions, the X and Y scan resolution and the number of averaging for each data point. The first performed scan is used to roughly position the pen on the MEMS chip. Common sizes include a 1 by 1 mm scan with a resolution of 5μm in the scanning direction and 10 μm for the perpendicular direction. This scan will take approximately 2 minutes to complete. Proper positioning takes many progressively smaller scans until the device it perfectly position below the pen. For a good quality scan,

a resolution of 0.5 by 0.5 μm should be used along with an averaging of 4. These scans will take considerably more time especially if a large area is needed. As example, a 100 μm square area will take approximately 6 minutes.

Varying different settings have different effects on the scan time. Varying either the number of averaging or scanning direction dimension only increases the scan time by 10% for a doubling of the setting. The scanning direction resolution has a huge effect on time when the resolution is set below 1 μm. It seems to increase asymptotically as the resolution approaches 0 μm. The non-scanning direction dimension varies proportionately with time, whereas the resolution has an inversely proportional relationship.

Common operations performed on area scans include 'thresholding', 'fill non-measured points', and 'levelling'. When the profiler attempts to read the reflected light in location of some step height increases and device corners, no light is reflected back to the sensor. These points are read as zero height points. And distort the scan especially if 3d views are needed. Thresholding simply removes those points from image and inserts a 'non-measured' point which does not distort the color scale. 'Fill non-measured points' estimates the height of non-measured points from their surrounding points.

Inserting the chip perfectly horizontal is not possible using the ZIF sockets. There might be a difference of 10-30 μm from each side of the 5x5 mm chip. To use the levelling operation, the user identifies three locations which should have the same height. An algorithm is them applied to level the scan so actual height can directly be compared.

5.2.1: **Off Position**

Figure 62 show the area scan of the 2DTA in its off position. All four arms are visible along with both layers at the tip. The blanket effect can be seen where the two outer Poly2 arms are laid over the Poly1 pad at the tip. The tip has an absolute height of 7.4 µm but the substrate also has an absolute height of approximately 0.5 µm.

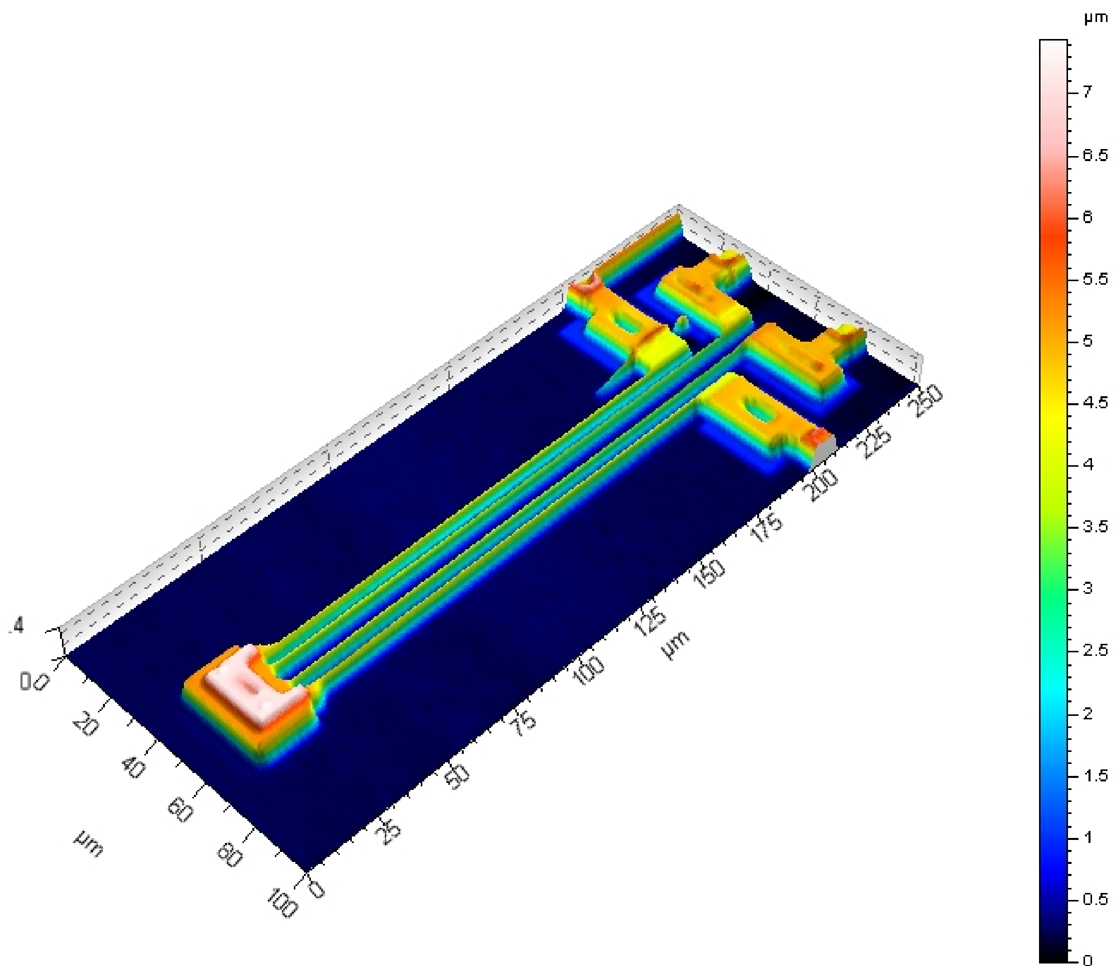

Figure 62: Area Scan of the 2DTA in the Off Position

5.2.2: **Maximum Lift Position**

An area scan when fully actuated was also taken. Figure 63 shows the 2DTA much higher than the surrounding structures. The maximum height reached above the

substrate is 11.4 μm. The fabricated 2DTA is theoretically 6.25 μm above the substrate, therefore is has displaced approximately 4.5 μm with a current flow of 3.0 mA through both Poly1 arms.

The arms of the 2DTA are only 2 μm wide and appear very thin in the area scans, especially when they are angled towards the TA tip. This happens since the profiler spot size is itself 2 μm in diameter. Unless the spot is directly above the arm, portions of the light spot will reflect from the substrate. It is unclear exactly how the hardware treats a spot partially on and off a sharp edge.

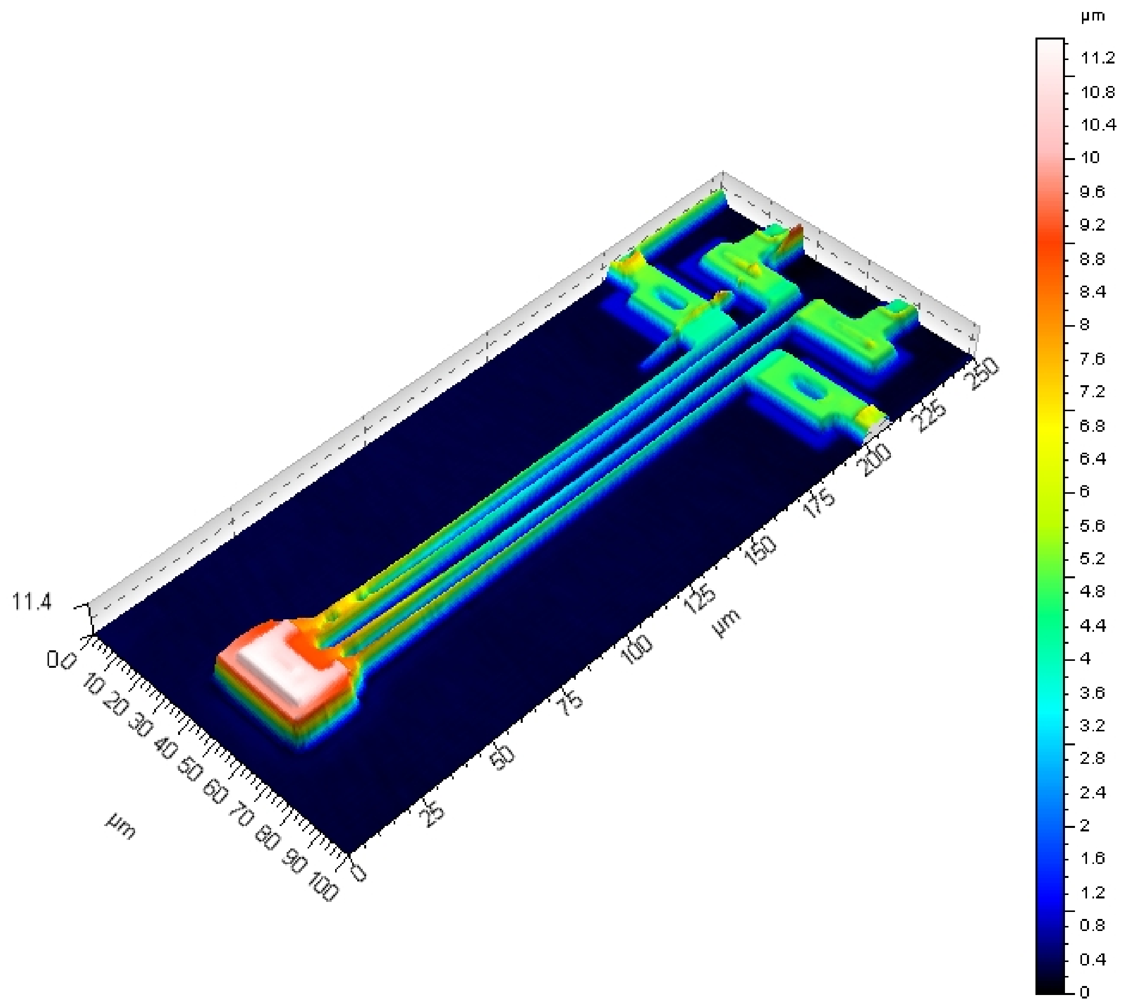

Figure 63: Maximum Lift Position Area Scan Isometric

A scan showing the maximum planar displacement would not be noticeably different than the off position since the in-plane displacements are only a few µm. The 2DTA tip is 33 µm wide so the displacement would only be 5% of the tip width, imperceptible at this magnification.

5.3: Profile Scans

As opposed to extracting 2D profiles from area scans as mentioned above, the Nanovea Optical Profiler can be used to only perform one line scan. Scan times are

reduced to approximately 5-10 seconds. This allows one to quickly measure either the X or Z-displacement of a TA tip. The smallest step size available is 0.1 µm with the total scan length having a minimum of 100µm. 100 µm is much larger than necessary for measuring the TA displacement but at only 7s per run, is insignificant.

5.3.1: **Cross Section Diagram**

When taking profiles, one must carefully consider what part of the TA one wants to scan. For height measurement scans, the profile must be taken in the arm oriented as shown in Figure 64. In this orientation one will capture the displacement and rotation of the tip. A tip rotation of approximately 4.5 degrees was measured when the 2DTA was fully actuated, resulting in a 1 µm height difference at each edge of the Poly2 layer. The tip rotation must be measured and the highest Poly2 point being the tip displacement.

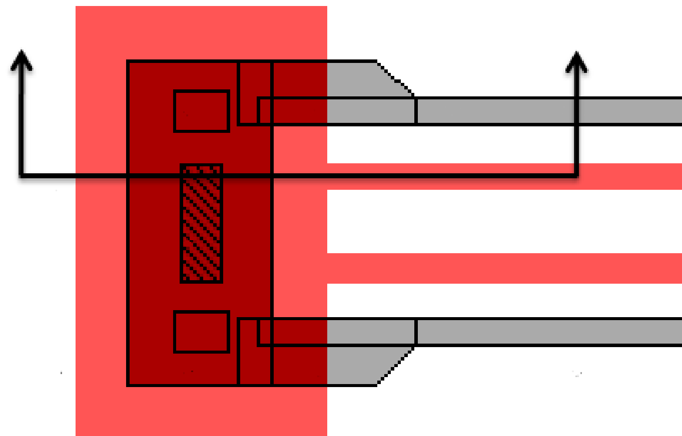

Figure 64: Height Measurement Cross Section Explanation

When measuring for in-plane displacement, the profile direction must be aligned with the displacement. For the 2DTA, the profile is perpendicular to the arms as seen in

Figure 65. The measurement should also be taken towards the free end of the arms as it will have the largest displacement.

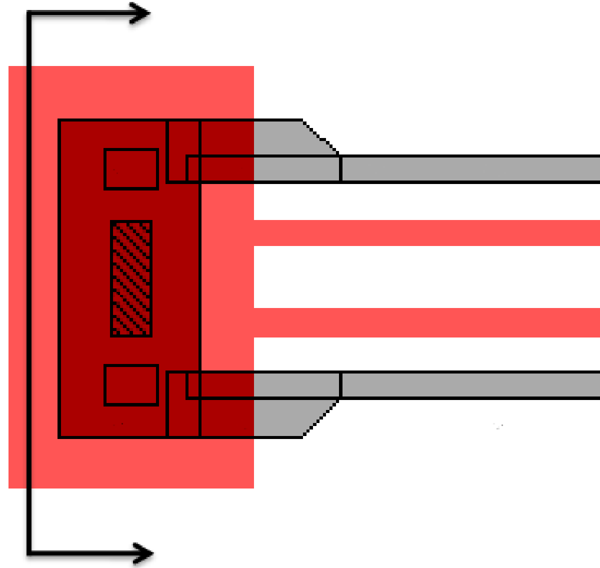

Figure 65: Planar Displacement Measurement Cross Section Explanation

5.3.2: Off Position Measurement

A profile of the 2DTA tip is shown in Figure 66. The profile has been taken in the direction shown in Figure 64. The sharp peak in Figure 66 located at a 'Scan Distance' of 55 µm is an artefact of the measurement technique not present in the actual device. To extract the actuator height above the substrate, the height reading of the flat portion on top are isolated first then a linear fit is applied. This is required as opposed to a simple average because the tip can have a rotation of up to 5°. The maximum value of the linear fit is used as the actuation height because that is the point which will contact the external object (e.g. shuttle).

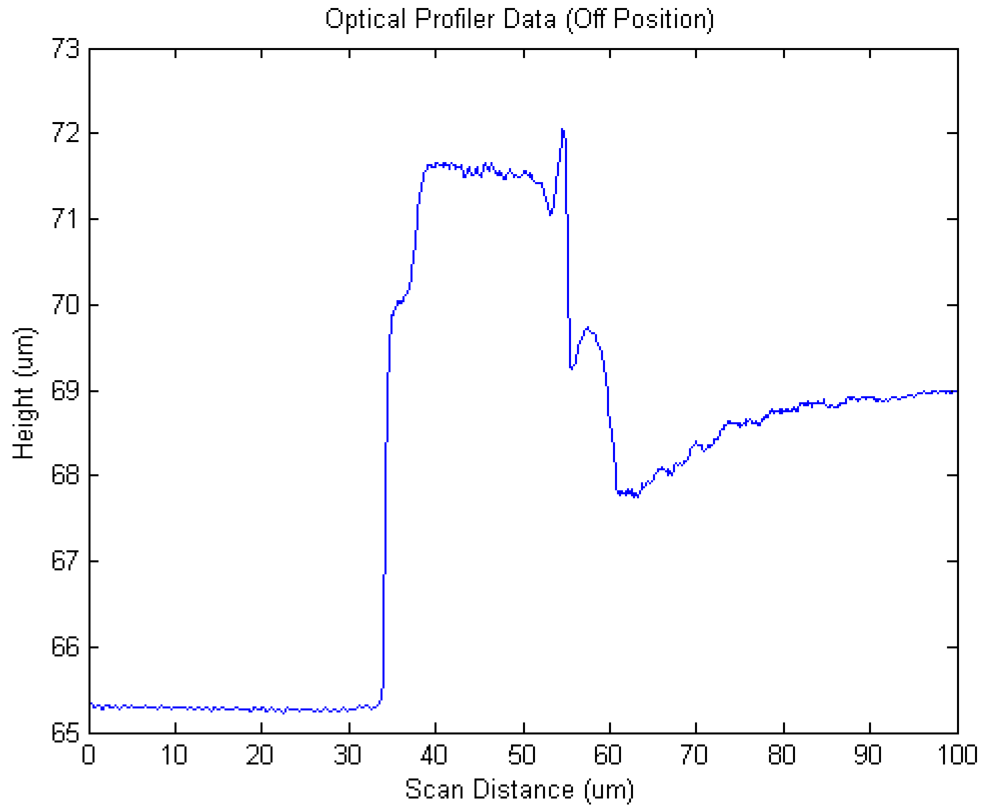

Figure 66: Optical Profiler Scan

The following two profile scan (Figure 67 and Figure 68) shows the effect of stiction in the off position. The mean step height reported in the stuck position is 5.33 µm while it is 6.48 µm in the unstuck position. This agrees with the theoretical height the actuator should be above the substrate. The theoretical height from the lower dimple surface to the substrate is 1.25 µm while the profiler measured a 1.15 µm difference between the stuck and unstuck positions. There is no way of determining whether the actuator is stuck in its off position other than analysing the results.

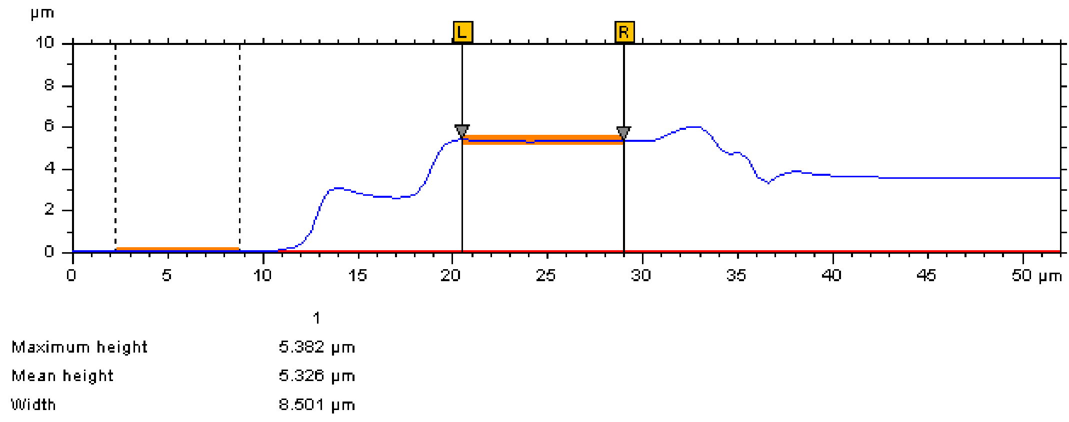

Figure 67: Stuck VTA

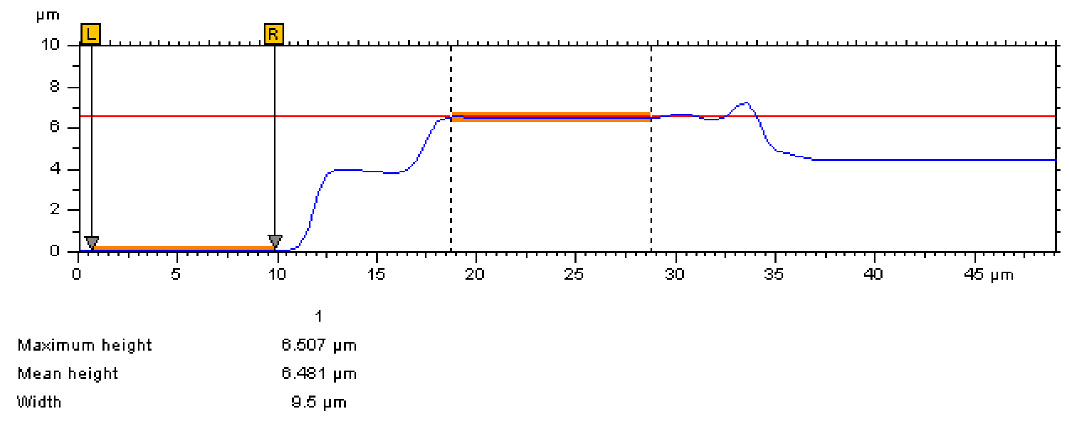

Figure 68: Unstuck VTA

5.3.3: **Maximum Lift Position**

To characterize the vertical lift of the 2DTA, the measured tip displacement was plotted versus Poly1 arm current (Figure 69). Three measurements were taken at each arm current with the average being plotted. The error bars show the maximum and minimum of the dataset. The resulting plot has a slight parabolic trend as is consistent with VTAs. The FEA results of Figure 43 are also overlaid and have an approximate error of -20% over the entire measurement range.

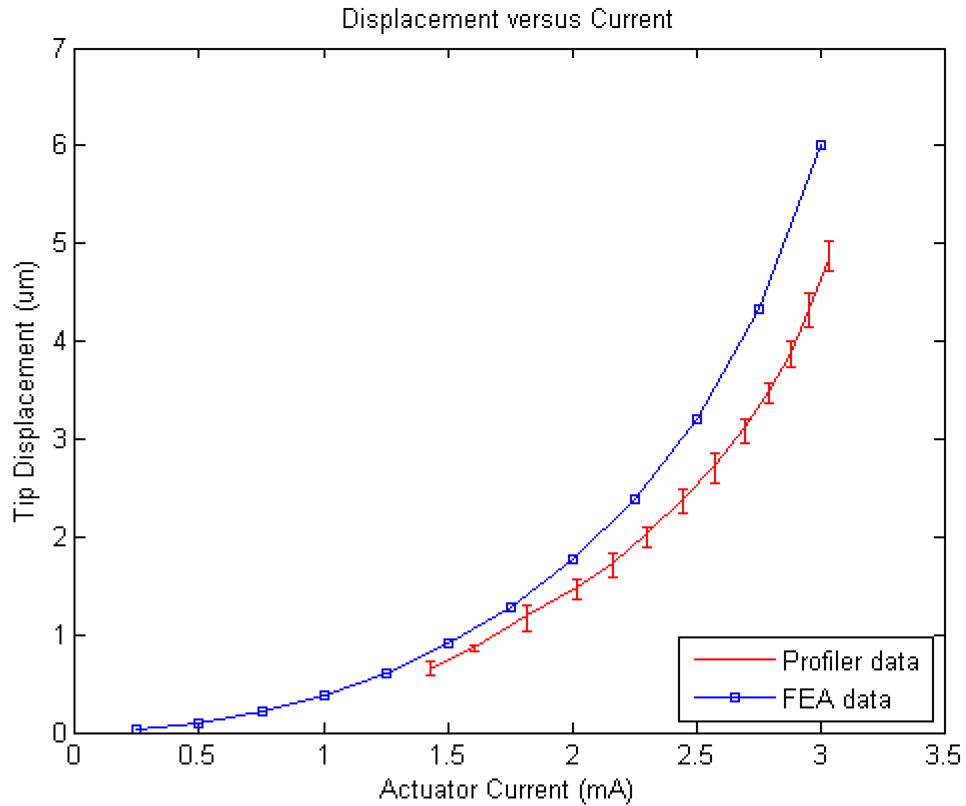

Figure 69: 2DTA Displacement versus Actuator Current Compared to FEA Results

To determine whether the actuator is stuck in it's on position under the Optical Profiler, the voltage and current must be compared. At a given voltage, the actuator will draw more current when it is stuck caused by the arm touching the substrate and therefore has greater heat dissipation. A hot arm has a higher electrical resistance when heated (Table 3). How much more current flows depends on many different variable such as how high the actuator should the displaced and what percent of the arm is stuck to the substrate. Before attempting to test on the Optical Profiler, a current versus voltage chart should be produced under the camera where you can be certain the TA is not stuck. The experiment can then be reproduced under the Optical Profiler with certainty the actuator is free.

5.3.4: **X and Z Displacement Combination**

To characterize the 2DTA, its displacement in various positions was measured and compared to FEA. First the actuator was powered under the microscope to determine an appropriate range of motion without burning the actuator. These same currents were then used to power the 2DTA under the Optical Profiler and implemented in the FEA model. Figure 70 below shows the overlaid results with the actual measurements in red and the FEA results in blue. Each measurement point is the average X and Z positions of three measurements.

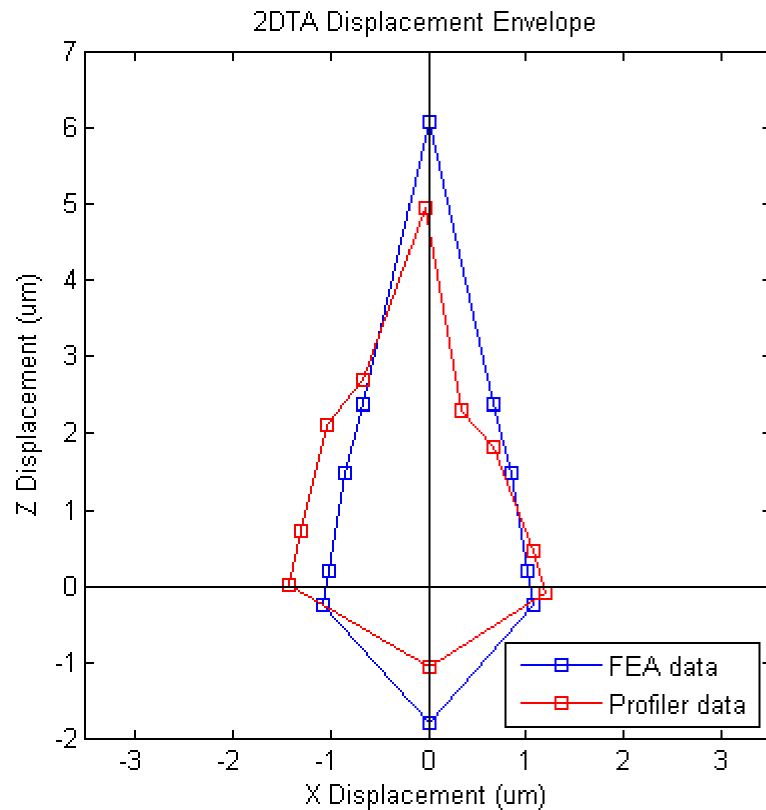

Figure 70: Overlaid 2DTA Displacement Envelope Comparing Experimental Results to FEA

Figure 70 indicates the actuator has a preferential actuation direction to the left. This is caused by PolyMUMPs layer alignment problems. The two center Poly1 arms are not perfectly centered between both Poly2 arms as seen in Figure 71. The actuator has higher displacements in the direction the arms are closer together. For Figure 71, the preferential actuation direction would be towards to top edge of the picture.

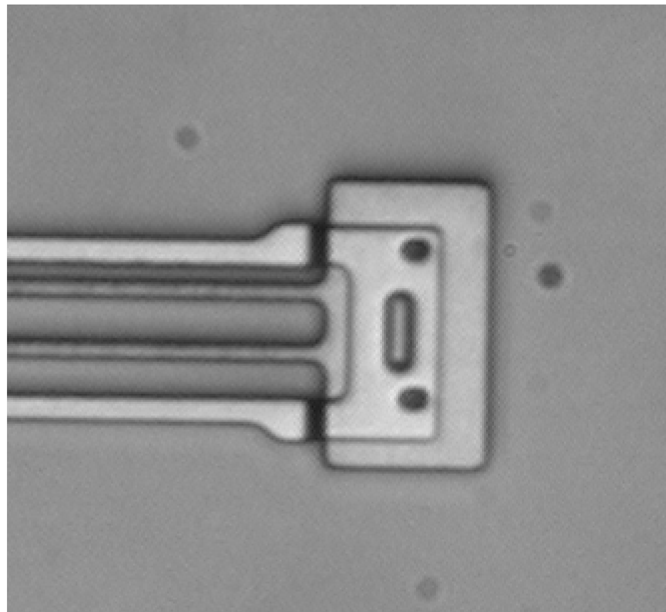

Figure 71: PolyMUMPs Layer Alignment Issues

Chapter 6: Collecting X-Displacement Data Using Camera Images

6.1: Experimental Setup

The planar motion measurements were performed on the lab setup outlined in Chapter 4: with the omission of the stepper motor and LabVIEW. Standard lab power supplies were used to apply the electric potential.

6.2: X-Displacement Using an Optical Camera

Due to the small size and forces produced by MEMS devices, taking physical measurements can be challenging. Displacement measurements using contacting methods could damage fragile features. The common method for measuring sub-micron displacement involves taking images with a standard CCD camera and tracking features from one image to another. Many complicated displacement methods exist, which track image phase change or use confocal microscopy. For example Yamahata [35] achieved sub-nanometre accuracy by performing a discrete Fourier transform on images of structured periodic micropatterned features designed on moving parts.

Using a simple camera, there are multiple ways of extracting object positions from an image. The most common of these include edge detection or pattern matching. Edge detection alone can then be performed in multiple ways. Common methods include extracting a line profile from an image then differentiating the profile. The edge would then be found at the maximum slope. The fastest form of edge detection for MEMS devices is simply looking for the minimum pixel intensity along the profile. The edge of interest is not a step change in intensity but more of a valley. Pattern matching attempts to track a pre-defined region of interest in consecutive images.

The two software packages evaluated in this study include National Instruments Vision Assistant and author developed MatLab code. The results will also be compared to experimental data collected using the Optical Profiler.

6.2.1: **NI Vision Assistant**

National Instrument Vision Assistant is a program used for extracting XY position data from an image stack or video. It allows you to create scripts using various functions then batch processing an entire image stack.

Common steps used include: Color Plane Extraction, Image Calibration, Edge Detection, and Pattern Matching.

6.2.1.1: **Color Plane Extraction**

Most computer vision functions require greyscale images. Depending on the video acquisition card, the captured image might contain the three RGB (Red, Green, and Blue) layers making it incompatible with the computer vision functions. The Dalhousie MEMS lab commonly uses the 'Pinnacle Dazzle' USB video acquisition device. It captures images using the VGA format maintaining all three RGB layers. The image must then be converted to an HSI (Hue, Saturation, and Intensity) image with the simple function, 'Color Plane Extraction' and choosing 'HSI' in the settings tab. The conversion is a weighted average of the three RGB colors for each pixel as shown in (5).

$$F = 0.2989 * Red + 0.5870 * Green + 0.1140 * Blue \tag{5}$$

The Point Grey cameras are true black and white cameras which store its image directly as greyscale images, making the color plane extraction step unnecessary.

6.2.1.2: **Edge Detection**

LabVIEW edge detection uses a derivative based method. The function first extracts a profile from the image then differentiates it. It finds edges by determining where the differentiated profile crosses a user defined threshold level. LabVIEW interpolates between values providing sub-pixel results.

6.2.2: **Matlab**

Two methods were programmed in MatLab by the author. The first is edge detection which attempts to find a black edge along a user defined profile. The second is pattern matching, in which the CPU is programmed to find the user defined region of interest (ROI) in each subsequent image.

6.2.2.1: **Edge detection**

Edge detection is the simplest form of displacement measurements. The user defines along which vector the program will search for the edge. A black edge looks like a deep valley when plotting pixel intensity versus arc length. The minimum pixel intensity value corresponds to the edge. As the edge translates, so does the valley.

To find the true edge, it is useful to average many parallel vectors. This greatly smoothes the resulting profile making the edge location easier to pinpoint giving more consistent results. Once a single profile has been isolated, the horizontal edge location must be calculated. A smooth polynomial is fitted near the profile's minimum value. The minimum value of the smooth curve is used as the result.

6.2.2.2: **ROI cross correlation**

The built-in MatLab function used to perform cross correlation is ‘normxcorr2’. The user inputs the ROI along with the image stack. The function is much more computationally expensive than the Edge detection algorithms. It overlays the ROI at all possible pixel location of the image and determines how well the ROI correlates. It is also limited by the pixel resolution of the image (0.147 µm/pixel).

6.2.3: **Optical Profiler X Measurements**

The Optical Profiler can also be used for in-plane measurements. The XY stage can be moved in steps of 0.1 µm, roughly 30% smaller increments than the camera pixel resolution. Figure 72 shows the profile when scanning across a 2DTA tip. The substrate is represented by the 0 µm height. The first step represents the 0.5 µm thick layer of Poly0 followed by the Poly1 layer actuator tip. The edge we are interested in the steeper Poly1 edge. Since the profile has low noise levels, the easiest solution involves differentiating the profile (Figure 73) then finding the maximum. Two larger peaks can be seen, the first being the rising edge, its position can easily be determined using the ‘max’ command. The two much smaller peaks represent the Poly0 edges.

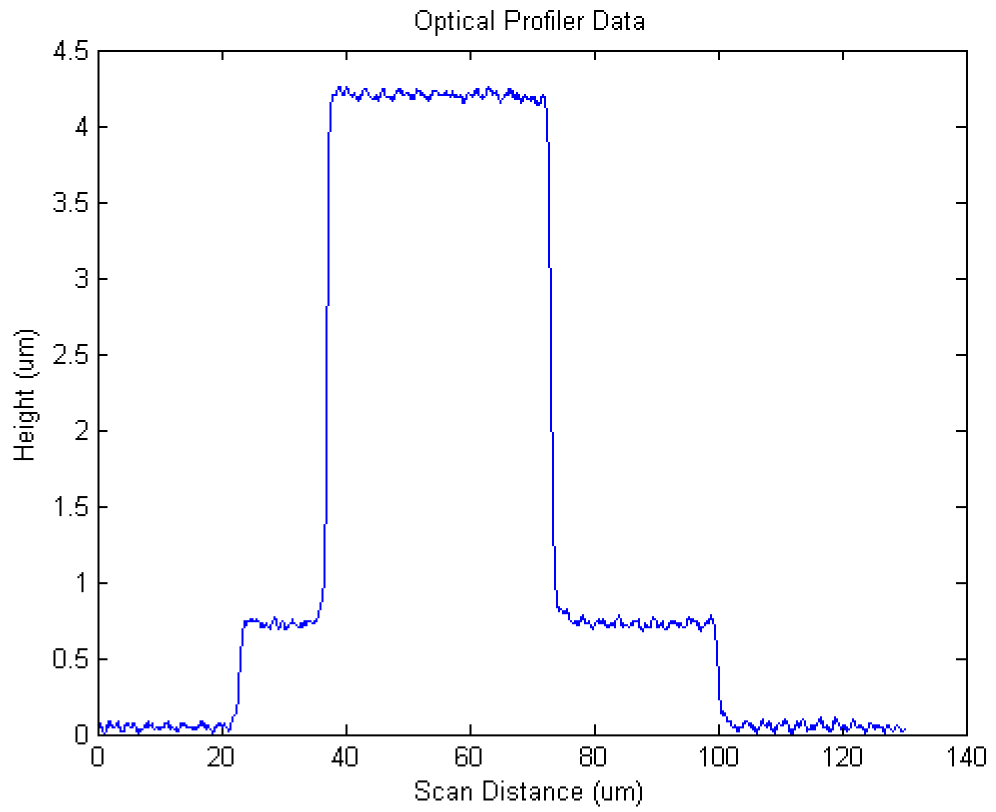

Figure 72: Raw Optical Profiler Data

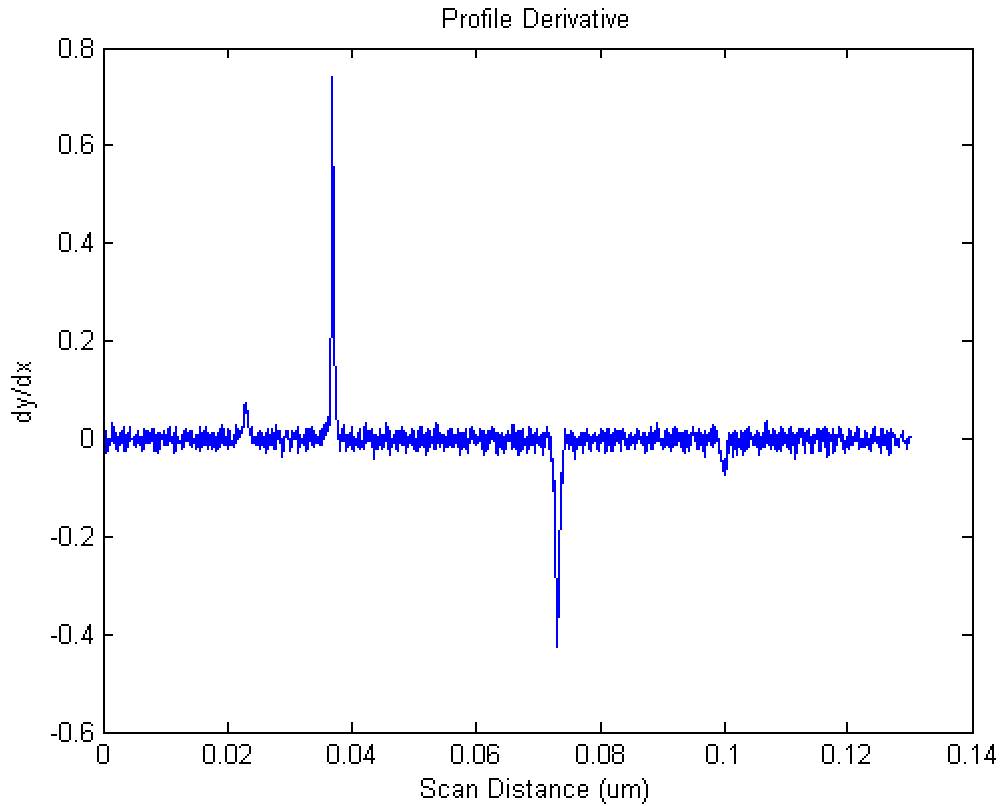

Figure 73: Profile Derivative

6.2.4: **Results**

To compare the suitability of each measurement method, they will all be applied on the same set of images. The actuator voltage was increased from 2.5 to 8 V in 0.5 V steps. Three runs in total were captured. A separate set of data was taken for the Optical Profiler data as it does not use images but profiles for its in-plane measurements. The images were all processed then the results overlaid in Figure 74. The error bars represent the maximum and minimum of each measurement with the data point being the average. As can be seen, four of the techniques provide similar results. With four methods giving the same results, I am thus considering them to be 'correct'. The LabVIEW edge detect results are within the error of the other measurement techniques up until approximately 5

V where its lower error bar is only touching the other's upper error bars. For the last three data points, there is significant error.

The LabVIEW edge detection is reporting higher displacements than the other four methods. It appears this tool is not appropriate for making displacement results of MEMS devices. This could be caused by what the line profile looks like. The Poly0-Poly1 edge appears as a black line meaning the profile pixel values will look as a valley not a step height which is what the software is looking for. Also as the actuator rises, light reflections can also be seen making the edge harder to distinguish using the LabVIEW software.

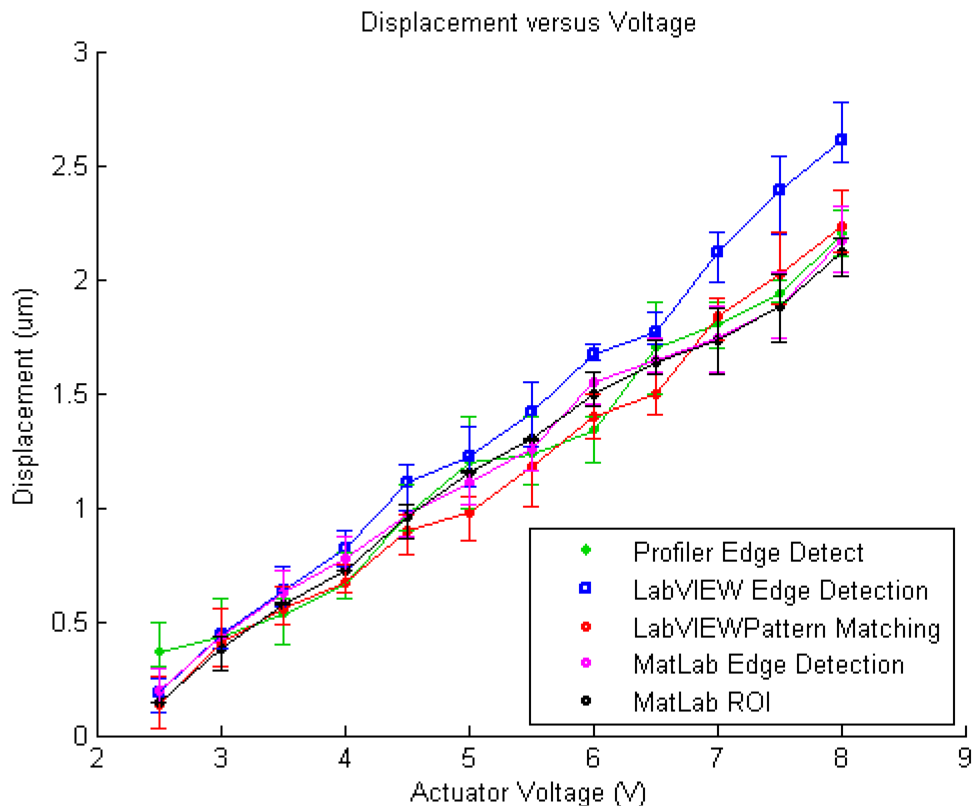

Figure 74: Displacement versus Voltage for Five Measurement Methods

To clarify the trends in Figure 74, linear fits are plotted in Figure 75. The resulting plot is much cleaner. We can see four of the measurements are practically overlaid.

In conclusion, either the Optical Profiler, both MatLab methods and the LAbVIEW pattern matching methods give similar results therefore any could be used for in-plane measurements.

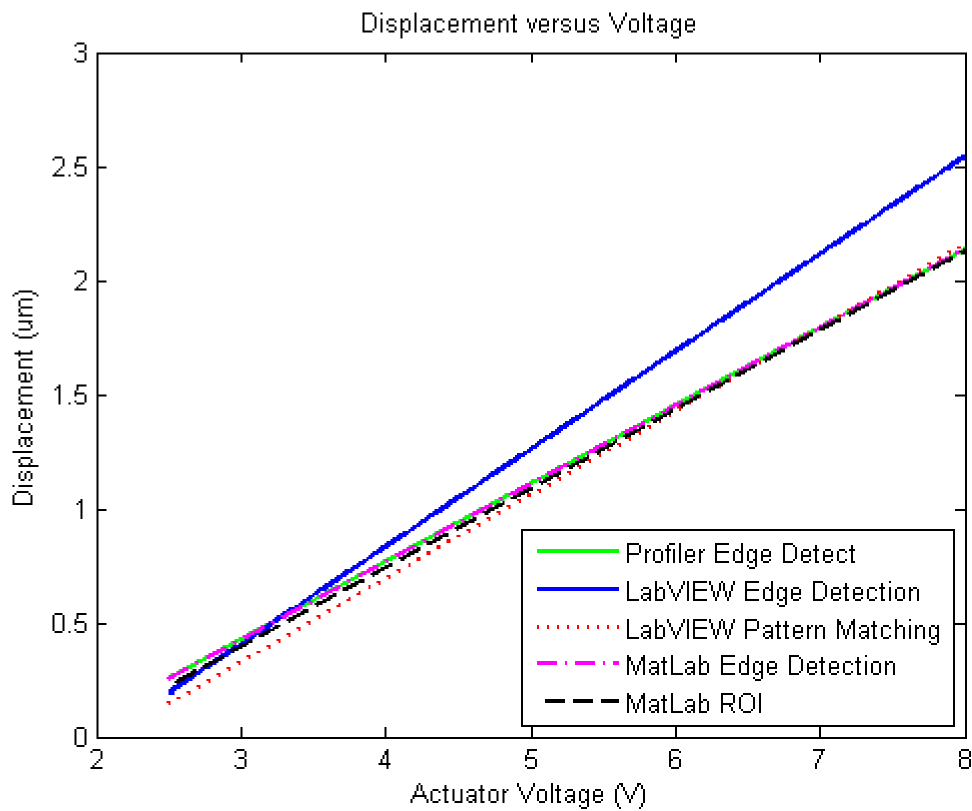

Figure 75: X-Displacement Linear Fits

Chapter 7: Collecting Z-Displacement Data Using Camera Refocusing

7.1: Theory

The goal of my research involves creating and measuring out-of-plane displacement; but with an optical camera as the primary viewing tool it is difficult to accomplish. One method is using an Optical Profiler as described in Chapter 5: but they are very expensive and some models do not allow the use of probes. They are very accurate (+- 20nm) but are considered specialty equipment only recently accessible to the Dalhousie MEMS Team.

A second method using an optical camera consist of taking multiple images (100+) at different focal planes and determining which image is most in-focus (Figure 76). A way of measuring or knowing the exact distance between focal planes is needed so a stepper motor driven distance adjustments will be used to take a discrete number of focusing steps

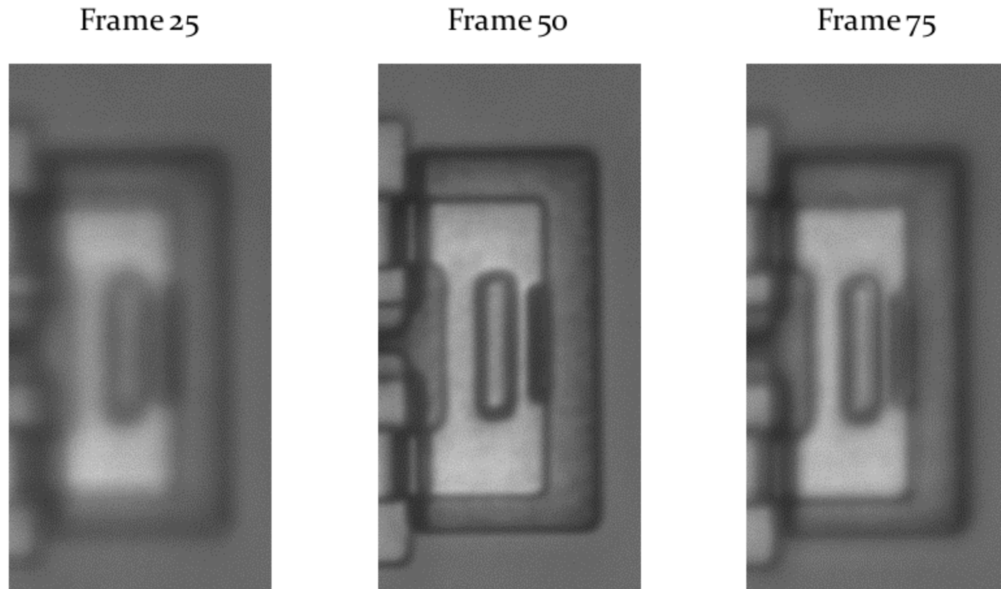

Figure 76: Example of Images when Varying the Focal Plane. The In-Focus Image is Frame 50

Once a set of images for incrementally varied distance from the objective has been taken, an algorithm is applied to each image's numerical representation which produces a single value for each frame. These values are then compared to the other images in the set to determine the most in-focus image. The highest value corresponds to the most in-focus image. A good algorithm must possess low noise and provide a clear and significantly high peak.

7.2: Experimental Setup

The hardware setup is described in Chapter 4, including the microscope and stepper motor setup and control.

7.3: Determination of Best Focus for MEMS Devices

Four algorithms are tested to determine their suitability for height measurements of MEMS devices. They were chosen because of their good results reported by Sun

(2004) and Santos (1997). These four algorithms include the Auto-Correlation, the Tenengrad gradient, Normalized Variance, and the Energy Laplace.

7.3.1: **Auto-Correlation Algorithm**

The Auto-Correlation was first reported by Vollath [36] and can be seen below in equation (6), where i(x,y) represents the pixel intensity. The equation looks for high frequency changes in pixel values along the X axis.

$$F_{auto_{cor}} = \sum_{Height} \sum_{Width} i(x,y) * i(x+1,y) - \sum_{Height} \sum_{Width} i(x,y) * i(x+2,y) \qquad \textbf{(6)}$$

After processing all images in the set and plotting the function value versus image focal plane height, Figure 77 was created. There is a clear peak at approximately 20 µm. virtually no noise is seen in the results with the peak being approximately 8 times higher than the out-of-plane images.

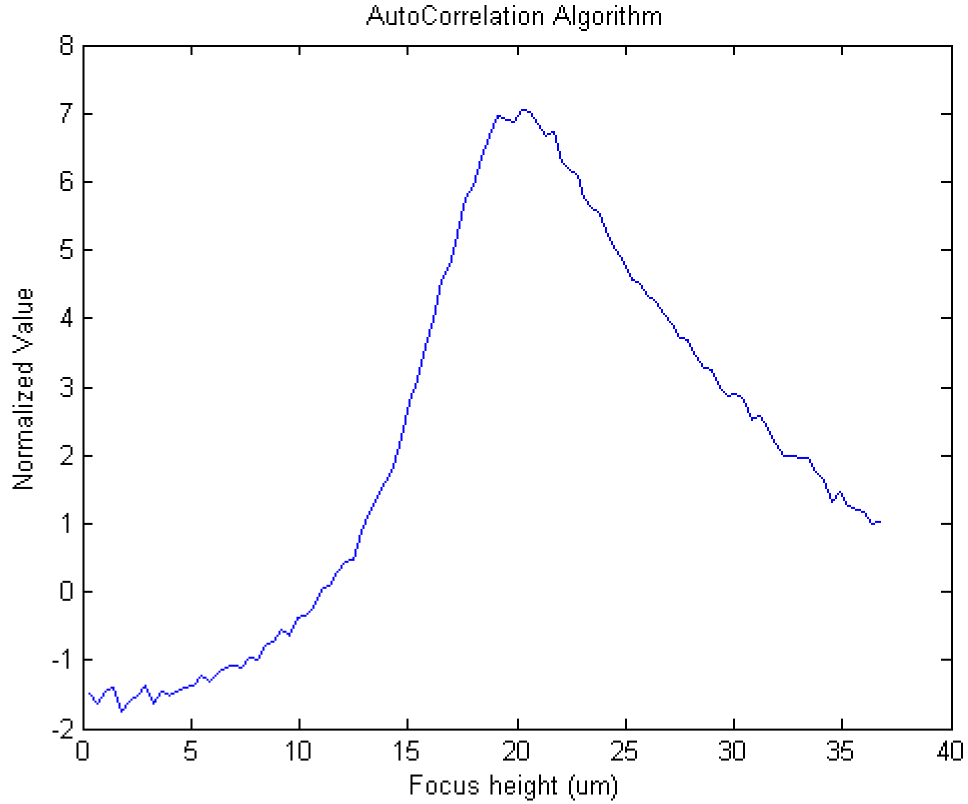

Figure 77: Normalized Autocorrelation Algorithm

7.3.2: **Tenengrad Gradient Algorithm**

The Tenengrad Gradient (7) uses the Sobel operators to emphasize the areas where pixel values are rapidly changing. Again these algorithms all attempts to determine which image is in focus by looking for higher frequency noise.

$$F_{Tenengrad} = \sum_{Height} \sum_{Width} S_x(x,y)^2 + S_y(x,y)^2 \quad \textbf{(7)}$$

Where $S_x(x,y)$ and $S_y(x,y)$ are the resultant images from convolution with the Sobel operators (Sun, 2004)

The result of the Tenengrad Gradient looks very similar to the Auto-Correlation Algorithm with the exception of slightly more noise. The peak is also at approximately

the 20 μm focal plane but it is only 25% higher than the out-of-focus value (note minimum value of y axis), which can cause problems in certain circumstance or noisy images.

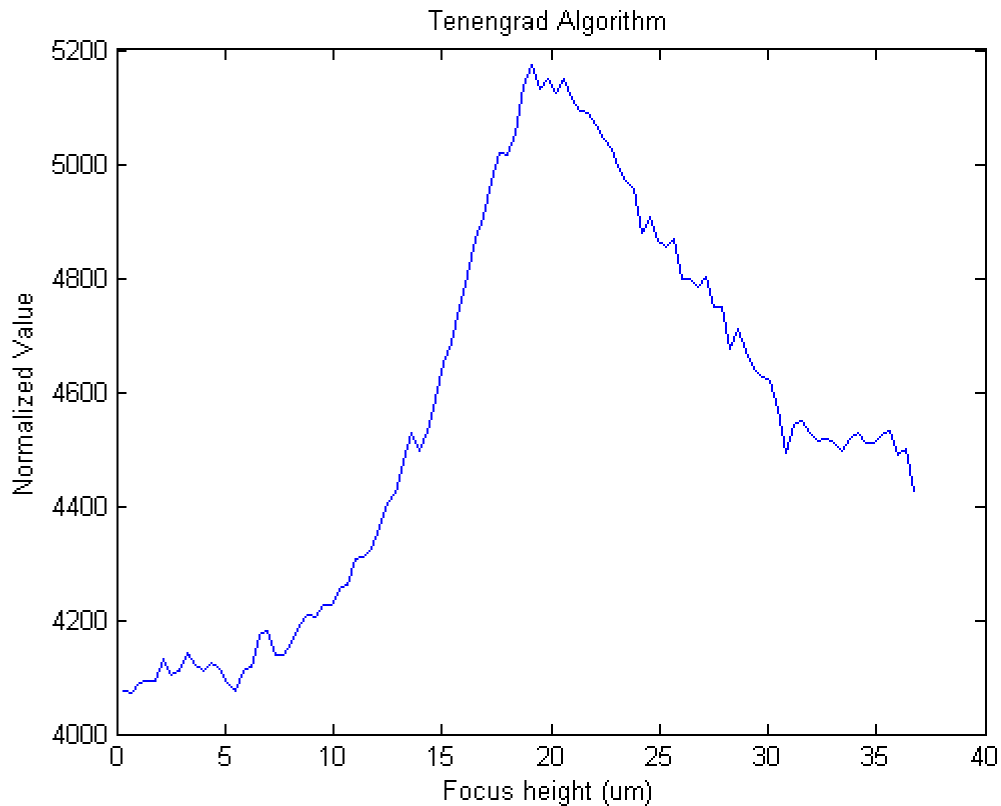

Figure 78: Tenengrad Algorithm

7.3.3: **Normalized Variance Algorithm**

The third algorithm (8) sums the difference of each pixel value and the image mean squared. The sum is them normalized by dividing by the image size and mean. It is a measure of the pixel variance in the image.

$$F_{normed_variance} = \frac{1}{H * W * \mu} \sum_{Height} \sum_{Width} (i(x,y) - \mu)^2 \quad \textbf{(8)}$$

Where H and W are the pixel sizes of the image and μ is the mean pixel intensity for the image. The resulting plot shown in Figure 79 has a wider peak but relatively low noise levels. The in-focus values are roughly twice as high as the out-of-focus images. The peak is approximately at the 22 μm focal plane.

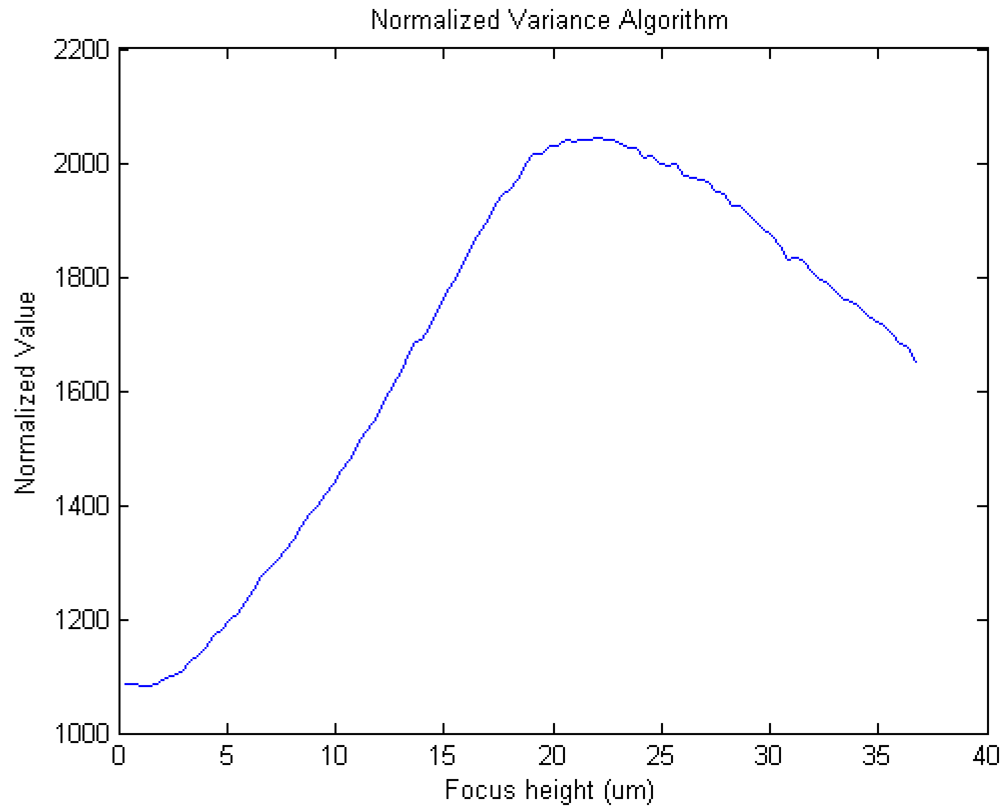

Figure 79: Normalized Variance Algorithm

7.3.4: **Energy Laplace Algorithm**

This method begins by convoluting the image with the high pass convolution mask *L* (9). It then sums the pixel intensity squared of the convoluted image as seen in (10). It is one of the easiest to program but gives poor results in highly zoomed images of MEMS devices (Figure 77)

$$L = \begin{bmatrix} -1 & -4 & -1 \\ -4 & 20 & -4 \\ -1 & -4 & -1 \end{bmatrix} \tag{9}$$

$$F_{energy_Laplace} = \sum_{Height} \sum_{Width} C(x,y)^2 \tag{10}$$

It can be seen in Figure 80 that the resulting plot is much noisier than the three previous algorithm tested. A rough peak can be seen at approximately the 17.5 µm focal plane.

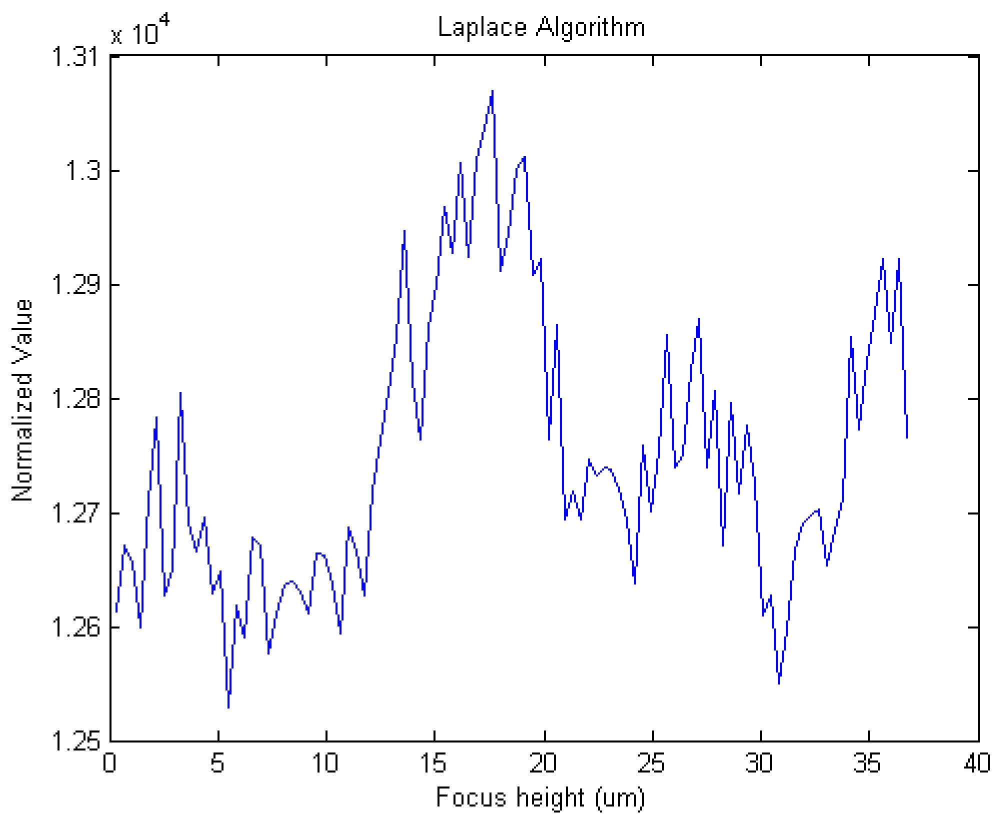

Figure 80: Laplace Algorithm

As all of the first three algorithms can be applied very quickly to each dataset, they will all be evaluated and compared to the Optical Profiler results obtained from the

same actuator. The resulting plots will be compared to experimental data obtained using the Optical Profiler.

7.4: **Results**

To calculate a height displacement, two sets of images must be taken. First, a set of images with the device off must be taken and analysed. The in-focus frame will be used as the reference focal plane. A second set with the device in the on position is then taken. The peak position will be shifted. Since the following tests were conducted by raising the focal plane for each image, the peak shift will be towards the right. Figure 81 shows two of these image sets using the Autocorrelation Algorithm. Notice the on data is shifted approximately 5 μm to the right. The peak is also significantly lower than in the off position, signifying the frame is less in-focus for the on position. The magnitude does not matter as long a clear peak is still present. For height measurements we are only interested in the lateral shift.

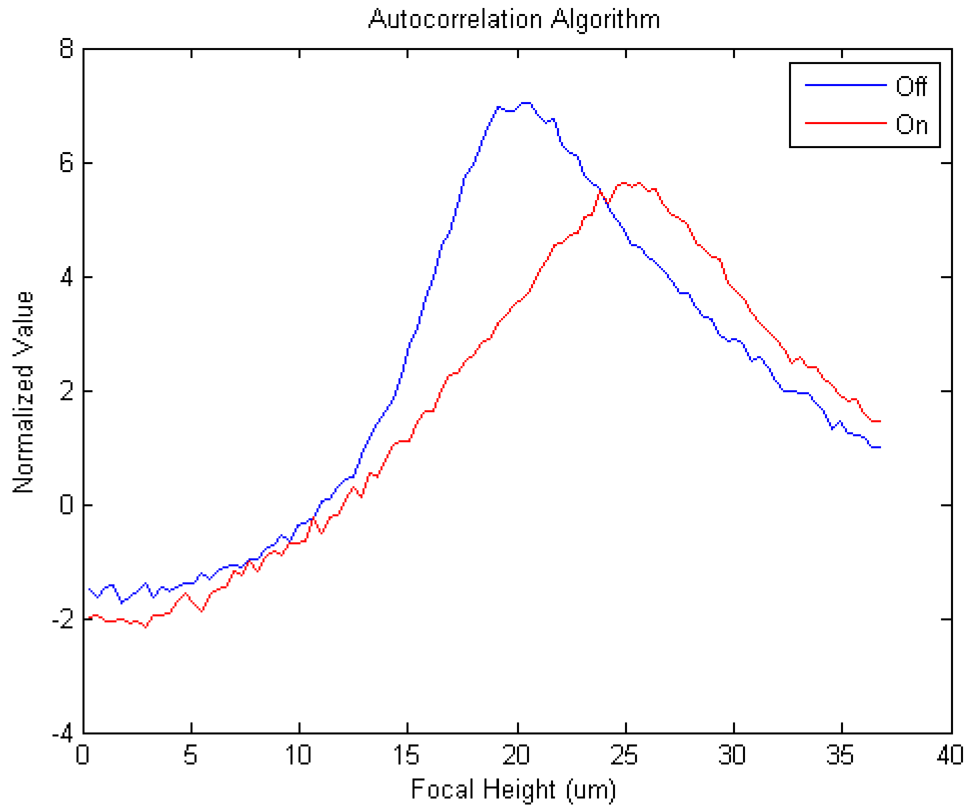

Figure 81: Overlaid Autocorrelation Results

In order to determine the horizontal peak location using MatLab, a section of the plot about the maximum algorithm value was isolated. A third order polynomial curve was fitted and the maximum of the fitted curve was used as the in-focus height. Figure 82 shows this fitting curve applied to the Auto-Correlation results.

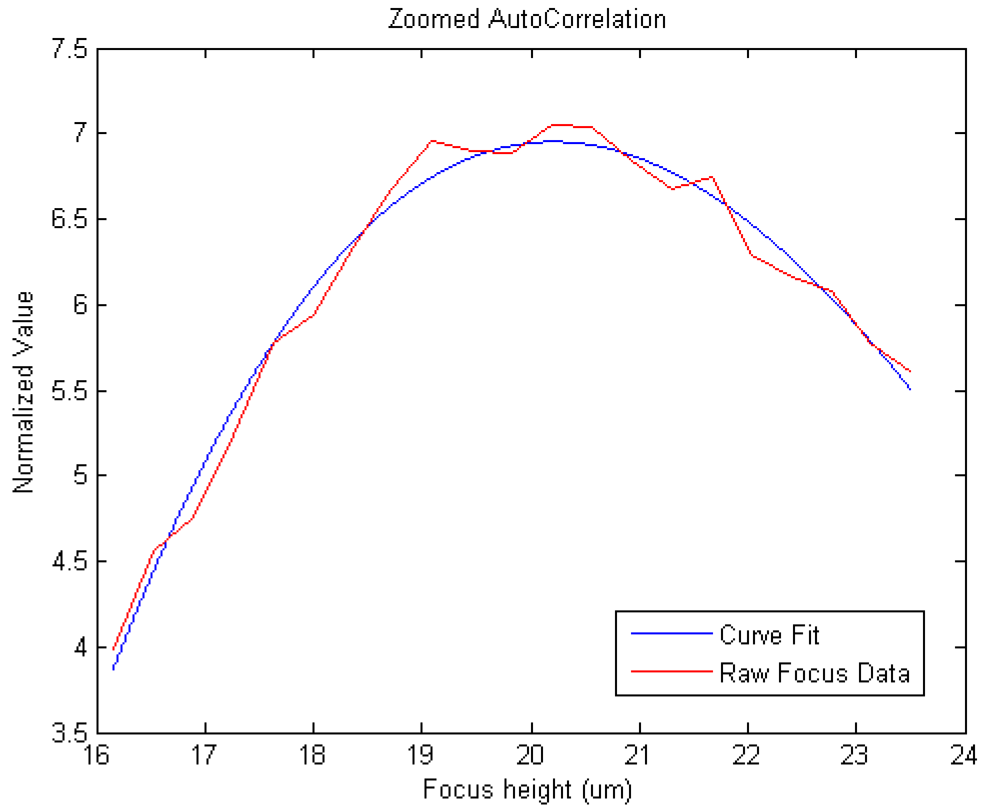

Figure 82: Zoomed in Autocorrelation Algorithm with Curve Fit

Common focus plane steps are either 2 or 4 stepper motor steps as they seem to give both a smoother curve and are less susceptible to noise.

The images were taken with the maximum zoom possible on our microscope (100x).

7.4.1: **Accuracy**

To evaluate the accuracy of the focus measurement technique, the results of each algorithm is compared to results from the Optical Profiler. Similar to the previous graphs shown, the error bars show the min/max with the data point being the average of all three values.

Figure 83 compares the Normalized Autocorrelation results. We can see the general trend follows the profiler results. The two results compare very well at both ends but the focus measurement returns values approximately 1 μm too high for the middle data points.

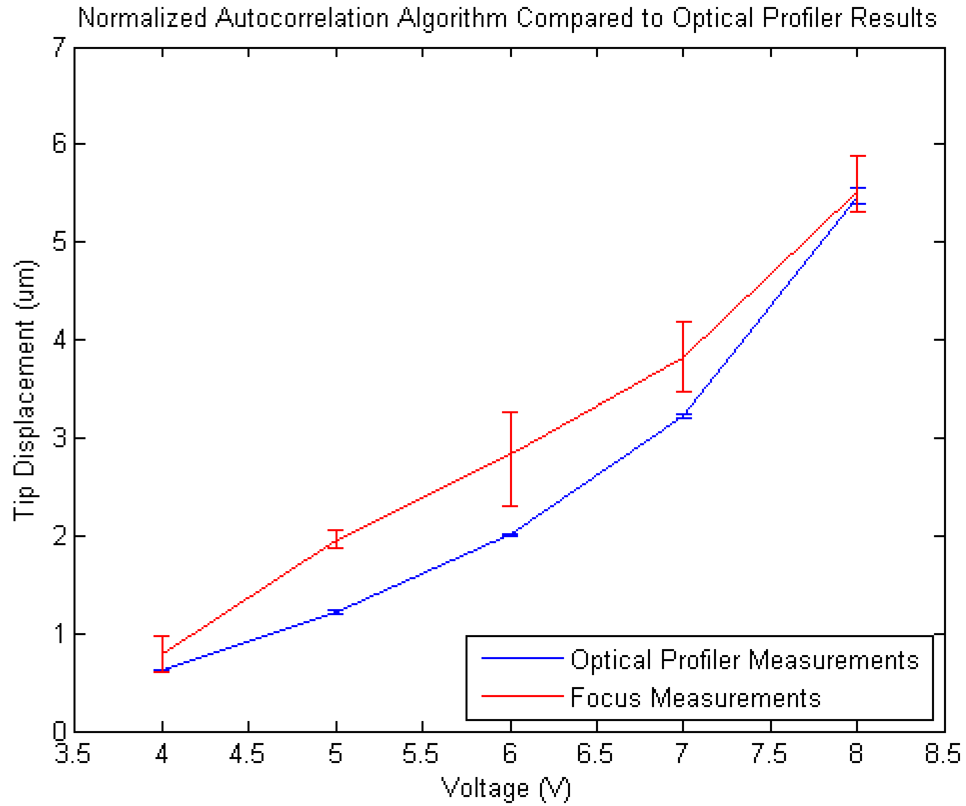

Figure 83: CV1 Autocorrelation Algorithm results compared to measured Optical Profiler Measurements

The second algorithm tested was the Normalized Variance. Figure 84 shows the results are not as accurate as the autocorrelation results. Each measurement features a larger variation. Also the trend looks linear as opposed to a quadratic trend for the profiler results.

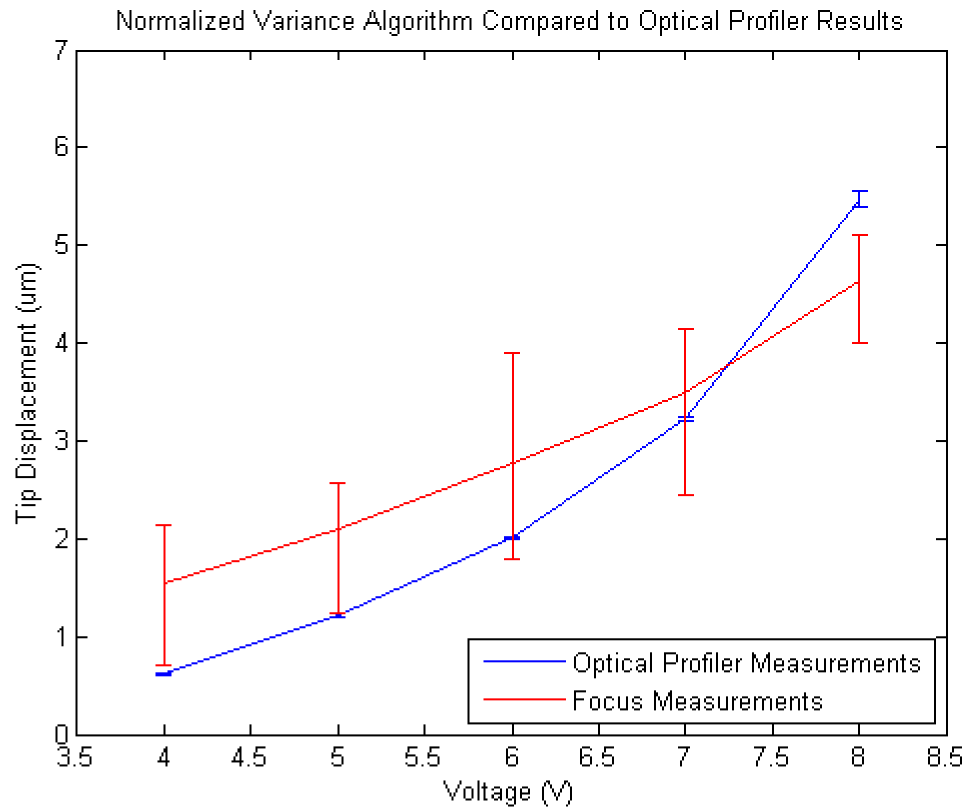

Figure 84: CV1 Normalized Variance Algorithm results compared to measured Optical Profiler Measurements

The Tennengrad Gradient shown below in Figure 85 features some of the largest single measurement variation of all three algorithms tested. The general trend follows the profiler results except the average focus measurements are consistently 0.5-1 µm high for all voltages tested.

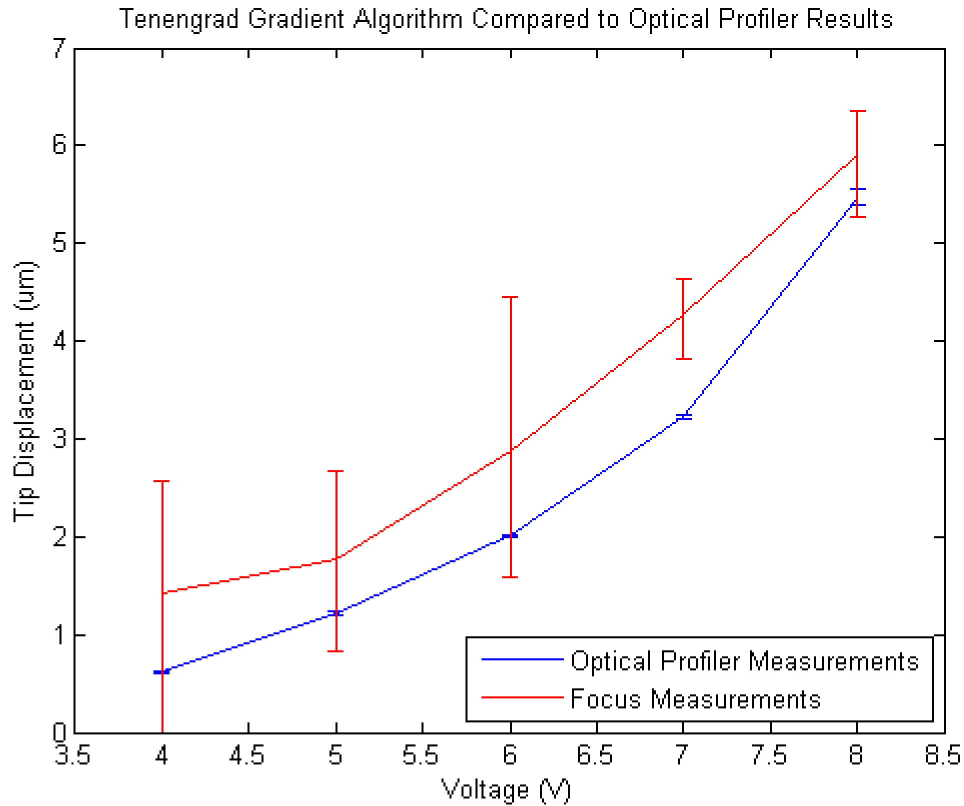

Figure 85: CV1 Tenengrad Gradient Algorithm results compared to measured Optical Profiler Measurements

It was determined that the focus algorithm give better results when only the actuator tip is present. Other devices in the frame widen the peak. If too much of the image is at a plane you do not wish to measure, you could produce a false peak.

Focus based methods could be valid measuring techniques under ideal conditions, but the consistency and accuracy of the method can quickly deteriorate. One of the largest problems was stiction, but not during the powered position. When measuring the 'off' set of images, it is hard to determine whether the actuator is in its 'off' position or partially stuck to the substrate. There is a 1 μm height difference between both position,

which is not large enough to positively determine whether the discrepancy is caused by measurement drift, stiction, or a combination of both.

7.4.2: **Recommendation**

To quantify the accuracy of the focus measurements, they were compared to measurements from the Optical Profiler. Figure 83 to Figure 85 demonstrates the overlaid results for a VTA at five different voltages. None of the three algorithm tested could reliably measure out-of-plane displacements to sub-micron accuracy. The focus results are usually within 1 μm of the profiler results. The focus results seem to be mostly higher than the profiler results which I attribute to some measurements being made with stiction in the off position.

Chapter 8: Future Work & Recommendations

An extension of the research presented in this thesis would be the transient analysis of the 2DTA using Comsol. The mechanical natural frequencies were calculated but the thermal time constant is estimated to be much lower as is common in MEMS actuators. Attempts have been made to obtain a more accurate time constant using the full non-linear model described in Chapter 3 but the results were inconsistent.

Fixing the wiring problem that plagued the most recent chip designs could make the 2DTA more reliable. A whole array of actuators could be assembled and tested to determine whether they do indeed make good shuttle drivers. A combination of broken jumpers and stiction prevented the testing of the shuttle arrays on the current chips. Figure 86 shows an SEM picture of a fabricated shuttle array. It features four separate actuators wired in parallel and three stationary pads. The stationary pads have the maximum attainable static height of 7.25 μm in PolyMUMPS.

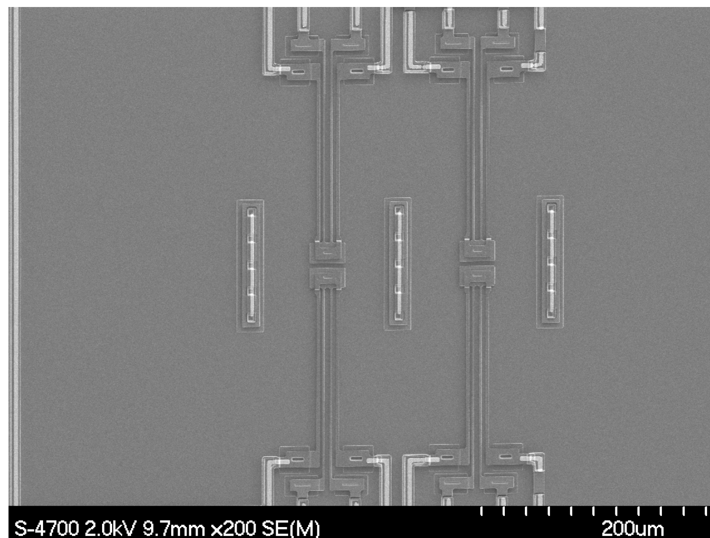

Figure 86: SEM Picture of a Shuttle Assembly

A complete cycle can be achieved in the following manner:

1. The shuttle lies on the pads until the actuators are lifted.
2. With the shuttle laying on the actuators, a small planar component to the displacement can be added to move the shuttle ahead.
3. The actuator then lowers while maintaining the planar displacement to replace the shuttle on the pads but slightly ahead of its starting location.
4. Power off the actuator to move it back to its starting location. This cycle can be repeated to produce long range motion.

Rebuilding the actuator with a smaller gap distance between arms could also be advantageous. Lee [14] concluded higher STA planar displacement could be achieved when using a gap distance of 1.8 μm.

Chapter 9: Conclusion

As indicated in Chapter 1, the main goals of this thesis involve the design of a novel 2DOF thermal actuator and the evaluation of various measurement techniques of its motion. The goals have been reached.

The concept of a 2 DOF actuator was derived by combining features of both an STA (Standard TA) and VTA (Vertical TA) into one actuator by using four separate arms and two structural layers of the PolyMUMPS process. A total of three 5x5 mm chips have been designed with each containing multiple designs. In total, 5 distinctly different geometry configuration of the actuator have been tested. A FEA was performed to determine whether the new actuator would perform as intended. The actuator displacements could not be compared using actuator voltages due to wire resistance variation from chip to chip so through current was used instead. Suitable displacements were found when using a 150 μm long actuator prototype. The out-of-plane displacements were consistent with a non-linear FEA simulation and were separately measured to reach 5 μm using an Optical Profiler. Planar displacements were measured at 1.5 μm, slightly higher than the FEA.

Because of the complex interactions of three current loops, a temperature dependant resistance, and height dependant heat transfer coefficients, it is recommended that an FEA model be used to characterize the actuator. Small variations in current can have a profound effect on tip displacement.

In-plane measurements methods using a camera were compared to determine their consistency. In total 5 different methods were tested including two with edge detection,

two with pattern matching, and one with edge detection using the Optical Profiler. All methods were acceptable except the edge detection using LabVIEW. Measuring out-of-plane displacements using a CCD camera and a stepper motor driven refocusing was also attempted. Four of the more popular biological autofocus algorithms for image processing were tested: the Autocorrelation algorithm produced the best results, as there was less variation between repeated measurements and they followed the Optical Profiler's trend the closest. The Laplace Energy Algorithm did not produce any usable results. I believe that the MEMS devices usually do not provide enough focus information in each image to obtain sub micron accuracy, but accuracy on the order of a few microns is possible under conditions with good illumination and no stiction.

Appendix A: Designed Chips

Three chips were designed and used for the research presented above. They all attempt to create a usable 2 DOF thermal actuator using the PolyMUMPS process. The names of all three chips in the order presented are IMUDTVT1, IMUDTVT2, and IMUDTVT3.

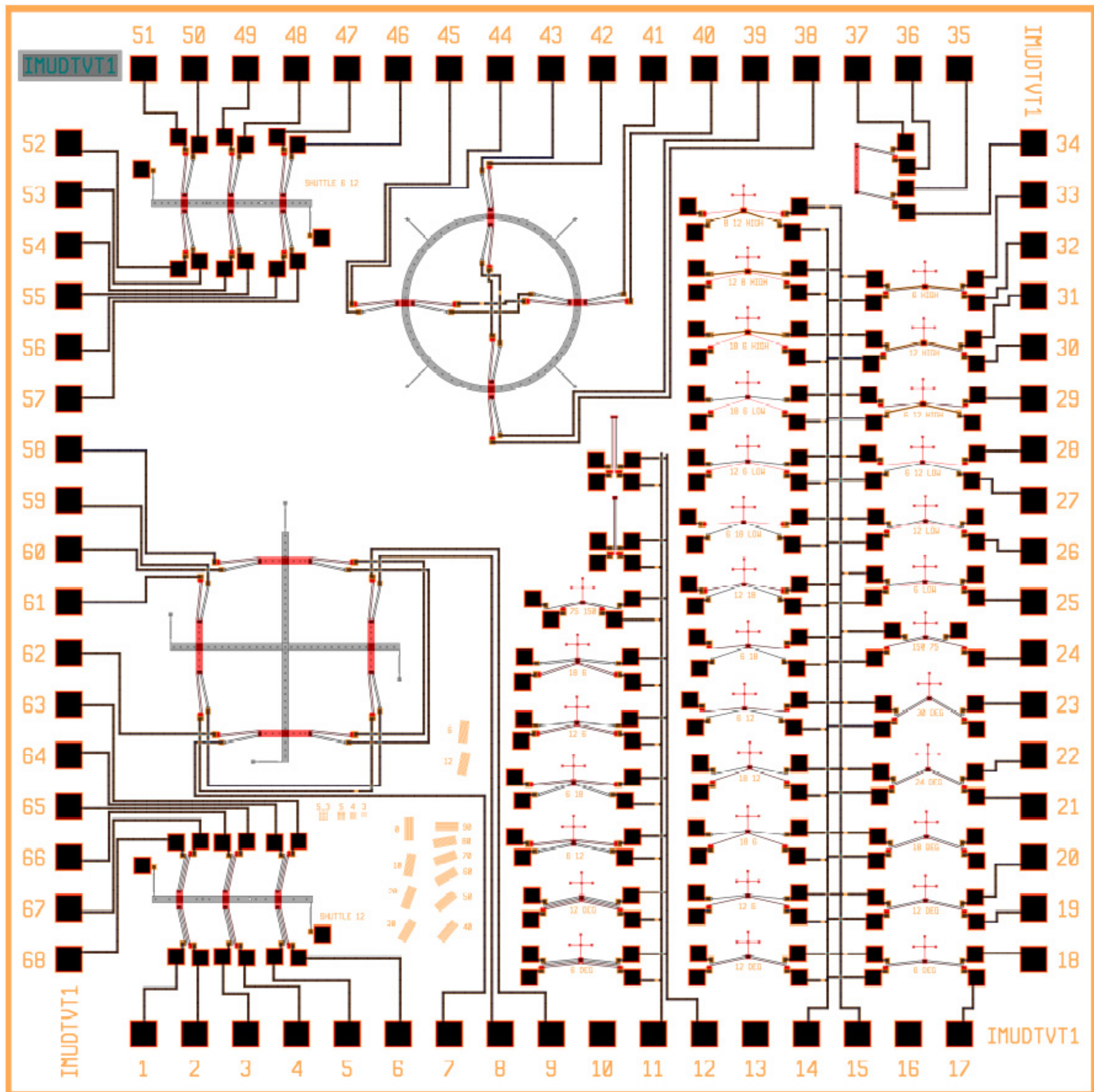

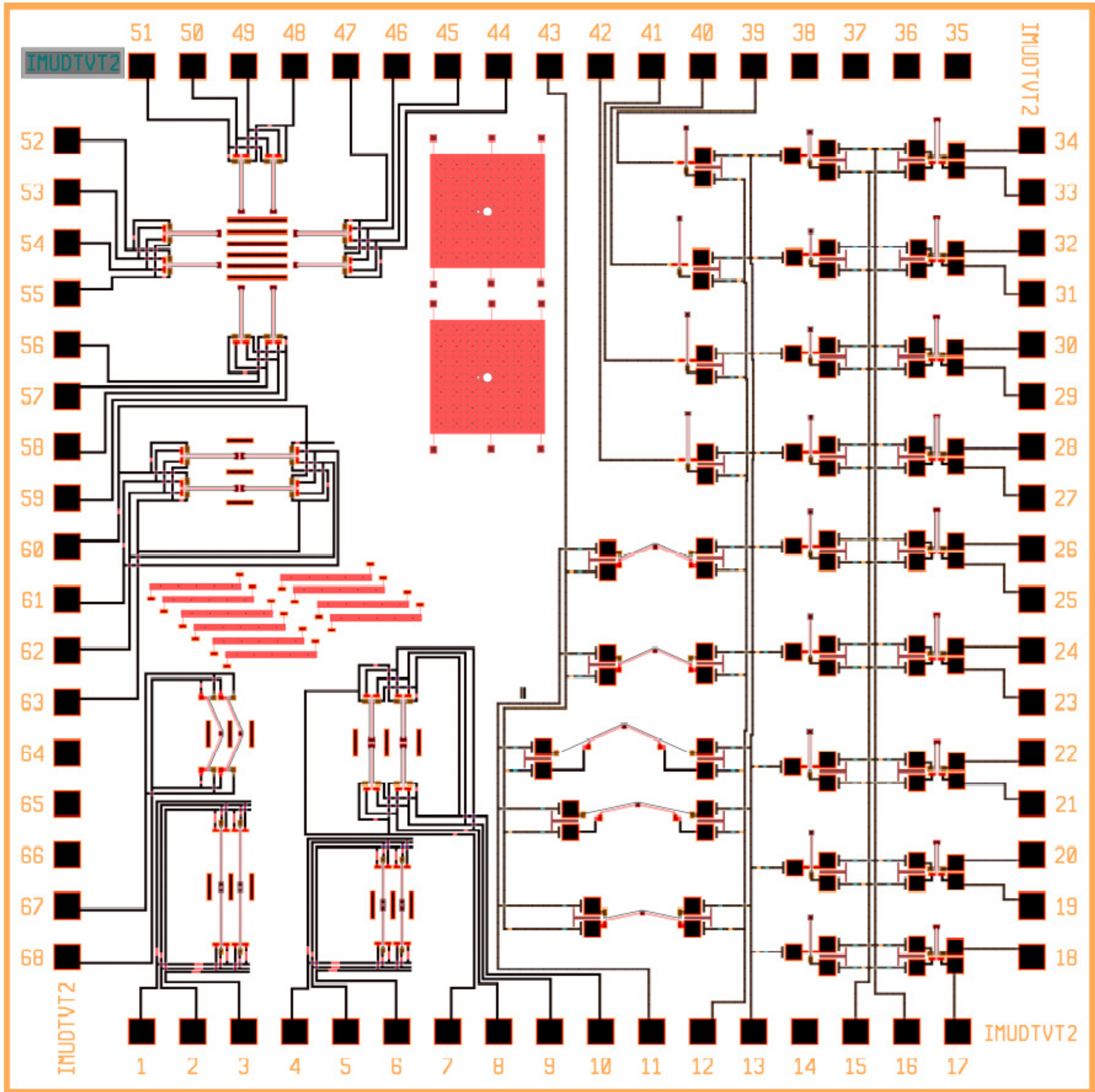
IMUDTVT2
51 50 49 48 47 46 45 44 43 42 41 40 39 38 37 36 35
IMUDTVT2
52
53
54
55
56
57
58
59
60
61
62
63
64
65
66
67
68
34
33
32
31
30
29
28
27
26
25
24
23
22
21
20
19
18
IMUDTVT2
1 2 3 4 5 6 7 8 9 10 11 12 13 14 15 16 17
IMUDTVT2

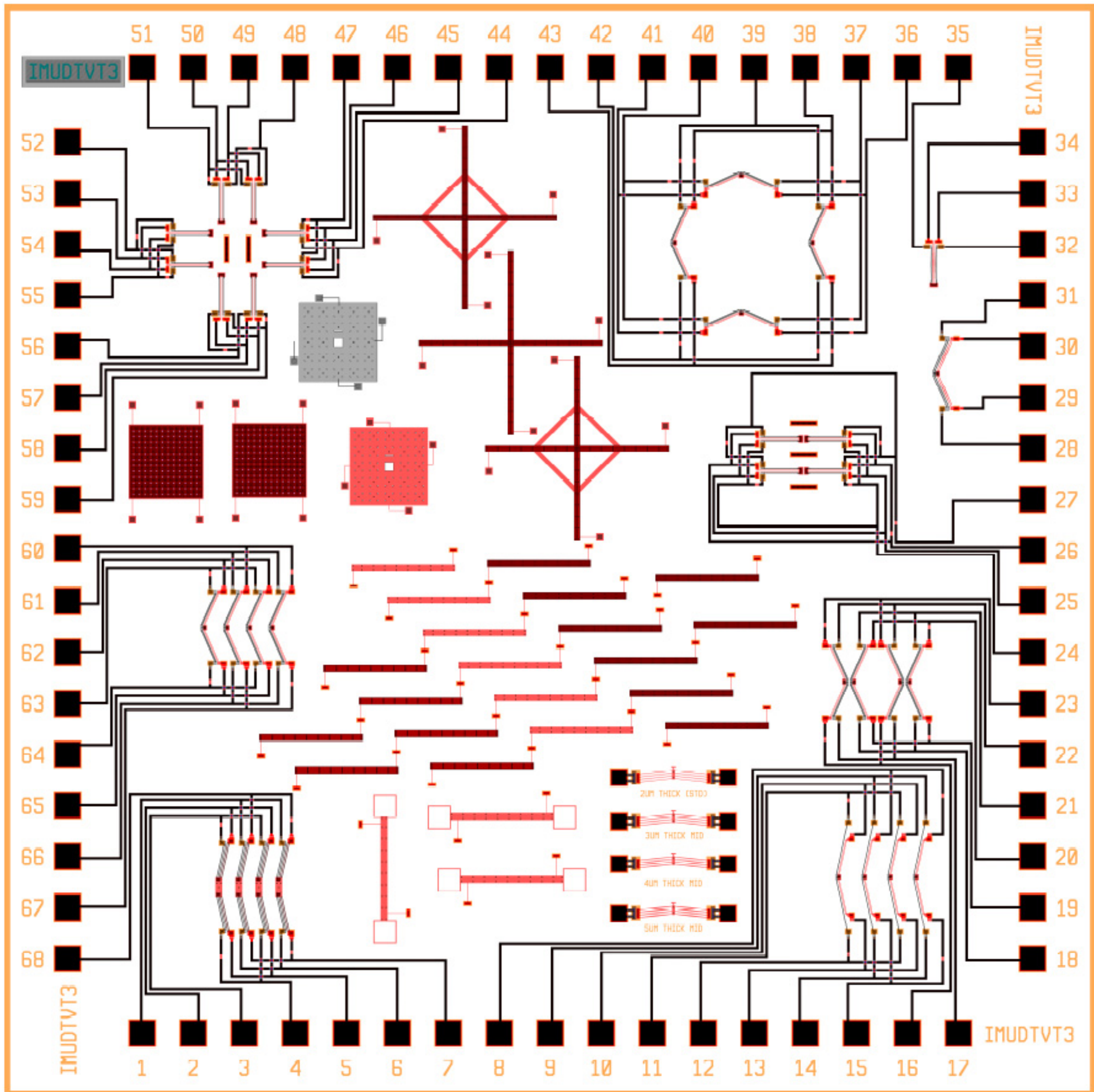
IMUDTVT3
51 50 49 48 47 46 45 44 43 42 41 40 39 38 37 36 35
IMUDTVT3
52
53
54
55
56
57
58
59
60
61
62
63
64
65
66
67
68
34
33
32
31
30
29
28
27
26
25
24
23
22
21
20
19
18
2UM THICK (STD)
3UM THICK MID
4UM THICK MID
5UM THICK MID
IMUDTVT3
1 2 3 4 5 6 7 8 9 10 11 12 13 14 15 16 17
IMUDTVT3

Appendix B: MatLab Code

B.1: Batch Sub-Micron Edge detection using the Optical Profiler

```
% this script plots displacement versus voltage from csv txt files
% change the 'path' variable to the folder containing the data files
% Inputs include the path variable and the actuator voltages 'v'


clc
clear all
close all
path='/media/MEMS RD/MEMS/THESIS/profiles/May24/run3';

cd(path)
path=strcat(path,'/*.txt');
list=dir(path);
s=size(list);
v=[0:3];
d=ones(1,s);

for i=1:size(list)

    %read in data
    M=csvread(list(i).name);
    x=M(:,1);
    y=M(:,2);

    % set data floor to 0
    m=min(y);
    for j=1:size(y)
        y(j)=y(j)-m;
    end

    % determine inflection point
    y1=[0; diff(y)];
    [r,j]=max(y1);
    d(i)=x(j);
end
d=d*1000; %converts mm to microns

figure;
plot(x,y1);
title('Profile Derivative')
xlabel('Scan Distance (um)')
ylabel('dy/dx')

m=max(d);
for j=1:size(d')
    d(j)=-(d(j)-m);
end
figure;
plot(v,d)
```

```
% Save height variable to file
str=regexp(pwd, '\', 'split');
l=length(str);
savefile=strcat(char(str(l)),'.mat');
cd('../')
save(savefile,'d');
```

B.2: Batch Height Measurements using the Optical Profiler

```
% this script plots Out-of-Plane displacement versus voltage from csv
% txt files change the 'path' variable to the folder containing the
% data files Inputs include the path variable and the actuator voltages
% 'v'

close all
clc
clear all

path='/media/MEMS RD/MEMS/THESIS/profiles/May24/run3';
cd(path);
path=strcat(path,'/*.txt');
list=dir(path);
s=size(list);
for i=1:s

        A=importdata(list(i).name);
        X=A(:,1)*1000;  % Converts to microns
        Y=A(:,2);%-min(A(:,2));       % Units already in microns

        windowSize = 10;
        Y=filter(ones(1,windowSize)/windowSize,1,Y);
        if i==1
            plot(X,Y)
            [x,y]=ginput(2);
            x=round(x*10)/10;
            for j=1:2
                [val, idx(j)] = min(abs(X-x(j)));
            end
        end

        for j=idx(1):idx(2)
            Y2(j-idx(1)+1)=Y(j);
            X2(j-idx(1)+1)=X(j);
        end
        p=polyfit(X2,Y2,1); % y=p(1)*x+p(2)
        Y3=polyval(p,X);
        height(i) = max(Y3);

end
figure(2)
v=[0:3];
height=height-height(1)
plot(v,height)
xlabel('Actuation Voltage')
ylabel('TA Tip height (um)')
```

B.3: Normalized Autocorrelation Function

```
function F = auto_corr(Image)
I=double(Image);
s=size(I);
sum1=0;
sum2=0;

for i=1:s(2) % y dimension
    for j=1:s(1)-2 % x dimension
        sum1=sum1+I(j,i)*I(j+1,i);
        sum2=sum2+I(j,i)*I(j+2,i);
    end
end
F=sum1-sum2;
end
```

B.4: Normalized Variance Function

```
function F = norm_var(Image)
I=double(Image);

mu=mean2(I);
s=size(I);
sum=0;
for i=1:s(2) % y dimension
    for j=1:s(1) % x dimension
        sum=sum+(I(j,i)-mu)^2;
    end
end
F=sum/(s(1)*s(2)*mu);
end
```

B.5: Tennengrad Gradient

```
function F = tenengrad(I)
I=double(I);
s=size(I);

%% Setup both Sobel filters
Gy=[-1  -2  -1;
    0   0   0;
    1   2   1];
Gx=Gy';

%% Perform Convolution
Sx=conv2(I,Gx,'same');
%figure; imshow(Sx);
Sy=conv2(I,Gy,'same');
%figure; imshow(Sy);

%% Tenenbaum Gradient
sum=0;
for i=1:s(2) % y dimension
    for j=1:s(1) % x dimension
        sum=sum+Sx(j,i)^2+Sy(j,i)^2;
    end
end
F=sum;
end
```

B.6: Maximum Focus Determination and Curve Fitting

```
function F = MEMS_max_focus(x,y,step,interval,plotting)

[ ~ , idx]=max(y);
y2=ones(size(y)-1);
x2=ones(size(x)-1);

for i=1:interval/(0.0918*step)*2
    y2(i)=y(uint16(idx-interval/(0.0918*step)+i-1));
    x2(i)=x(uint16(idx-interval/(0.0918*step)+i-1));
end

p=polyfit(x2,y2,3);
x3=min(x2):0.001:max(x2);
y3=polyval(p,x3);
[ ~ , idx]=max(y3);

if plotting==1
    figure; plot(x3,y3,x2,y2, 'r');
end

F=x3(idx);
```

B.7: Main

```
clear all
close all
clc

%%%%% INPUTS %%%%%%%%%%
path='C:\Users\Public\User Files\Rene\THESIS\Image Blur\stepper motor
focus\march23\4V\run3\on\aligned\';
stepper_step=4;
interval=6;
plotting=0; % toggle zoom plot (1-on 0-off)
%%%%%%%%%%%%%%%%%%%%%%%%

cd(path);
list=dir(strcat(path,'*.pgm'));
s=size(list);

% Initialize variables
x=zeros(1,s(1));
t=zeros(1,s(1));
g=zeros(1,s(1));

tic
for i=1:size(list);
    I=imread(list(i).name);
    f(i)=norm_var(I);   % Normalized Variance Function
    g(i)=auto_corr(I);  % Normalized Autocorrelation Function
    h(i)=high_freq(I);  % Laplace Function
    t(i)=tenengrad(I);
    x(i)=i*0.0918*stepper_step;
end
toc
%%
autocorrelation=MEMS_max_focus(x,g,stepper_step,interval,plotting)
%#ok<NOPTS>
title('Zoomed AutoCorrelation'); xlabel('Focus height
(um)');ylabel('Normalized Value');
norma_var=MEMS_max_focus(x,f,stepper_step,interval,plotting)
%#ok<NOPTS>
title('Zoomed Norm_Var'); xlabel('Focus height (um)');
tenen=MEMS_max_focus(x,t,stepper_step,interval,plotting)
title('Zoomed Tenengrad'); xlabel('Focus height (um)');
Laplace=MEMS_max_focus(x,h,stepper_step,interval,plotting)
title('Zoomed Laplace'); xlabel('Focus height (um)');
```

References

1. *A reliable single-layer out-of-plane micromachined thermal actuator.* **Chen, Wen-Chih, et al.** Hsinchu, Taiwan : Elsevier Science B.V., 2003, Vol. 103, pp. 48-58.

2. *A Low-Power-Consumption Out-of-Plane Electrothermal Actuator.* **Girbau, David, et al.** 3, s.l. : Journal of Microelectromechnical Systems, 2007, Vol. 16, pp. 719-727.

3. *A Bubble-Jet MEMS printhead Integrated with CMOS De-Multiplexer.* **Liou, Jian-Chiun, Liu, Chien-Hung and Chen, Chun-Jung.** Hsinchu, Taiwan : IEEE/SEMI Advanced Semiconductor Manufacturing Conference, 2004. 0-7803-8312-5/04.

4. Three Axis Accelerometer. *RobotShop.* [Online] [Cited: May 2, 2011.] http://www.robotshop.com/ca/sfe-mma7260q-triple-axis-accelerometer.html .

5. **Ellerington, Neil.** *Macro Friction, Micro Friction & Stiction.* Mechanical Engineering, Dalhousie University. Halifax, Canada : s.n., 2009.

6. *In Situ Characterization of Induced Stiction in a MEMS.* **Yu, Tao, et al.** 2, Lubbock, USA : Journal of Microelectromechanical Systems, 2006, Vol. 16, pp. 355-364. 10.1109/JMEMS.2007.893061.

7. PolyMUMPs. [Online] [Cited: 05 15, 2011.] http://www.memscap.com/mumps/documents/PolyMUMPs.DR.v11.pdf.

8. **Tabib-Azar, Massood.** *Microactuators Electrical, Magnetic, Thermal, Optical, Mechanical, Chemical and Smart Structures.* Norwell, USA : Kluwer Academic Publishers, 1998.

9. **Sameoto, Dan.** *Operation and Characterization of MUMPs Produced Microactuators in a Water Enviroment.* Mechanical Engineering, Dalhousie University. Halifax, Canada : s.n., 2004. Masters Thesis.

10. *Tilted folded-beam suspension for extending the stable travel range of comb drive actuator.* **Zhou, Guangya and Dowd, Philips.** Signapore, Signapore : Journal of Micromechanics amd Microengineering, 2003, Vol. 13. 0960-1317/03/020178+06.

11. *Time and frequency response of two-arm micromachined thermal actuators.* **Hickey, Ryan, et al.** Halifax, Canada : Journal of Micromechanics and Microengineering, 2001, Vol. 13, pp. 40-46. 0960-1317/03/010040+07$30.00.

12. *Force, deflection and power measurments of toggled microthermal actuators.* **Lai, Yongjun, et al.** Halifax,Canada : Journal of Micromechanics and Microengineering, 2003, Vol. 14, pp. 49-56. 10.1088/0960-1317/14/1/307.

13. *An in-plane, bi-directional electrothermal MEMS actuator.* **Venditti, Roberto, et al.** Toronto, Canada : Journal of Micromechanics and Microengineering, 2006, Vol. 16. 0960-1317/06/102067+04.

14. **Lee, Jeongkwan.** *Analysis and Optimization of MEMS Out-of-Plane Thermal Actuators.* Mechanical Engineering, Dalhousie Unviersity. Halifax, Canada : s.n., 2003. Masters Thesis.

15. *Heat transfer analysis and optimization ot two-beam microeletromechanical thermal actuators.* **Hickey, Ryan, Kujath, Marek and Hubbard, Ted.** 3, Halifax, Canada :

Journal of Vacuum Science Technology, 2002, Vol. 20, pp. 971-974. 0734-2101/2002/20(3)/971/4/$19.00.

16. *Extending the traveling range with a cascade electrostatic comb-drive actuator.* **Chiou, Jin-Chern, Lin, Yung-Jiun and Kuo, Chin-Fu.** Hsin-Chu, Taiwan : Journal of Micromechanics and Microengineering, 2007, Vol. 18. 0960-1317/08/015018+07.

17. *Analysis of out-of-plane thermal microactuators.* **Atre, Amarendra.** 2006, Joutrnal of Micromechanics and Microengineering, Vol. 16, pp. 205-213. doi:10.1088/0960-1317/16/2/003.

18. *A novel self-aligned vertical electrostatic combdrive actuator for scanning micromirrors.* **Tsou, C, et al.** Taichung, Taiwan : Journal of Micromechanics and Microengineering, 2005, Vol. 15. 10.1088/0960-1317/15/4/025.

19. *Design and modeling of a MEMS bidirectional vertical thermal actuator.* **Yan, Dong, Khajepour, Amir and Mansour, Raafat.** Waterloo, Canada : Journal of Micromechanics and Microengineering, 2004, Vol. 14, pp. 841-850. 10.1088/0960-1317/14/7/002.

20. *Am out-of-plane rotational platform with in-plane electrostatic combs made by the MetalMUMPs process.* **Tsai, Jui-che, et al.** Taipei, Taiwan : Journal of Micromechanics and Microengineering, 2009, Vol. 19. 10.1088/0960-1317/19/7/074007.

21. *A large vertical displacement electrothermal bimorph microactuator with very small lateral shift.* **Wu, Lei and Xie, Huikai.** Gainesville, USA : Sensors and Actuators A, 2007, pp. 371-379. 10.1016/j.sna.2007.10.068.

22. *Design and Characterization of Single-Layer Step-Bridge Structure for Out-of-Plane Thermal Actuator.* **Chen, Wen-Chih, et al.** 1, Hsinchu, Taiwan : Journal of Microelectromechanical Systems, February 2008, Journal of Micromechanical Systems, Vol. 17, pp. 70-77. 10.1109/JMEMS.2007.906761.

23. *Dynamic response modelling and characterization of a vertical electrothermal actuator.* **Li, Lijie and Uttamchandani, Deepak.** Glasgow, UK : Journal of Micromechanics and Microengineering, 2009, Vol. 19. 10.1088/0960-1317/19/7/075014.

24. *A Novel Bistable Two-Way Actuated Out-of-Plane Electrothermal Microbrige.* **Michael, Aron, et al.** 1, Sydney, Australia : Journal of Micromechanical Systems, 2008, Vol. 17. 10.1109/JMEMS.2007.911369.

25. **Hickey, Ryan.** *Analysis ans Optimal Design of Micro-Machined Thermal Actuators.* Mechanical Engineering, Dalhousie University. Halifax, Canada : s.n., 2001. p. 74, Master's Theisis.

26. *Autofocusing in Computer Microscopy: Selecting the Optimal Focus Algorithm.* **Sun, Yu, Duthaler, Stefan and Nelson, Bradley J.** Toronto, Canada : Microscopy Research and Technique, 2004, Vol. 65, pp. 139-149. 10.1002/jemt.20118.

27. *Evaluation of autofocus functions in molecular cytogenetic analysis.* **Santos, A., et al.** 3, Madrid, Spain : Journal of Microscopy, 1997, Vol. 188, pp. 264-272.

28. *A New Smart Vision System Using a Quick-Response Dynamic Focusing Lens.* **Kaneko, Takashi, Mitsumoto, Naoki and Kawahara, Nobuaki.** Aichi, Japan : IEEE, 200, pp. 461-466. 0-7803-5273-4/00.

29. *Microscopic Shape from Focus Using Active Illumination.* **Noguchi, Minori and Nayar, Shree K.** New York, USA : IEEE, 1994, pp. 147-152. 1051-4651/94.

30. *Thermal Assembly of Polysilicon Microstructures.* **Fedder, Gary K. and Howe, Roger T.** California, USA : Institute of Electrical and Electronics Engineers, 1991, pp. 63-68. CH2957-9/91/0000-0063.

31. **National Instruments.** [Online] [Cited: May 10, 2011.] http://sine.ni.com/nips/cds/view/p/lang/en/nid/207406.

32. Pololu 8V - 35V, 2A Single Bipolar Stepper Motor Driver w / Regulators. *RobotShop.* [Online] [Cited: 1 13, 2011.] http://www.robotshop.com/ca/pololu-8v-35v-2a-single-bipolar-stepper-motor-driver-w-regulators.html.

33. Profilometers. *NANOVEA.* [Online] http://www.nanovea.com/Profilometers.html.

34. **d'Entremont, Rene.** *Optical Profiler Measurements of MEMS Devices.* Mechanical Engineering, Dalhousie Unviersity. 2010. Directed Studies, Ma.S.C.

35. *Subnanometer Translation of Microelectromechanical Systems Measured by Discrete Fourier Analysis od CCD Images.* **Yamahata, Christophe, et al.** 5, Lausanne, Switzerland : Journal of Micromechanical Systems, 2010, Vol. 19, pp. 1273-1275. 10.1109/JMEMS.2010.2067445.

36. *Automatic focusing by correlative methods.* **Vollath, D.** 3, Federal Republic of Germany : Journal of Microscopy, 1987, Vol. 147, pp. 279-288.

37. *Thermal characterization of microheaters from the dynamic response.* **Jayaraman, Balaji, Navakanta, Bhat and Pratap, Rudra.** Bangalore, India : Journal of Micromechanics and Microengineering, 2009, Vol. 19. 10.1088/0960-1317/19/8/085006.

38. *Design and electro-thermal simulation of a polysilicon microheater on a suspended membrane for use in gas heating.* **Khanna, V K, et al.** Durgapu, India : Indian Journal of Pure & Applied Physics, 2007, Vol. 45, pp. 332-335.